Doctoral theses at NTNU, 2023:219

Emanuele Solfiti

On the modelling of flexible graphite

Doctoral thesis

NTNU
Norwegian University of Science and Technology
Thesis for the Degree of Philosophiae Doctor
Faculty of Engineering
Department of Mechanical and Industrial Engineering

NTNU
Norwegian University of Science and Technology

Emanuele Solfiti

On the modelling of flexible graphite

Thesis for the Degree of Philosophiae Doctor

Trondheim, June 2023

Norwegian University of Science and Technology
Faculty of Engineering
Department of Mechanical and Industrial Engineering

NTNU
Norwegian University of
Science and Technology

NTNU
Norwegian University of Science and Technology

Thesis for the Degree of Philosophiae Doctor

Faculty of Engineering
Department of Mechanical and Industrial Engineering

© Emanuele Solfiti

ISBN 978-82-326-7138-0 (printed ver.)
ISBN 978-82-326-7137-3 (electronic ver.)
ISSN 1503-8181 (printed ver.)
ISSN 2703-8084 (online ver.)

Doctoral theses at NTNU, 2023:219

Printed by NTNU Grafisk senter

Preface

This PhD thesis is submitted in partial fulfilment of the requirements for the degree of Philosophiae Doctor (PhD) at the Norwegian University of Science and Technology. It resulted from a three-years collaboration between the *Department of Mechanical and Industrial Engineering* (NTNU) and the *Sources, Targets and Interactions* section of the *European Organization for Nuclear Research* (CERN). On NTNU side, the work has been supervised by Prof. Filippo Berto together with the adjunct professor, as well as Senior Researcher at *SINTEF Materials and Nanotechnology*, Antonio Alvaro. On CERN side, the collaboration has been managed by the head of the *Target, Collimators and Dumps* section Marco Calviani, together with the technical manager of the same section Nicola Solieri.
Most of the experimental work has been conducted at the MTP Fatigue lab and Nanomechanical lab. In addition, the thermo-mechanical tests were performed at the SINTEF laboratory, the Computed Tomography was carried out at the Physics Department (NTNU) and the Focused Ion Beam - Scanning Electron Microscope (FIB-SEM) investigation was conducted at the *Nanolab* facility (NTNU - NorFab).
The thesis is written in the form of monograph. The author has been responsible for writing the original draft, conceptualization, methodology, numerical work, formal analysis, data curation, visualization and the testing part performed in the Fatigue Lab at NTNU. He collaborated with lab technicians in the rest of the experimental campaign.

Emanuele Solfiti
Trondheim, Norway
21-04-2023

Acknowledgements

First, I would like to express my gratitude to my supervisors at NTNU, Filippo Berto and Antonio Alvaro. Filippo gave me the chance to carry out my PhD here and provided positive support throughout the whole project. Antonio was always purposeful and dynamic; he managed to create a pleasant working and collaborative environment, and his support was essential for the success of my PhD.

Furthermore, I would like to thank all the CERN collaborators from the section *Target, Collimators and Dumps*, headed by Marco Calviani. A special thanks goes to Nicola Solieri for boosting this project when he became part of it, for the great help, the precious suggestions and the patience kept along the path.

A large part of the work has been carried out at NTNU and SINTEF laboratories: there, for the success of the experimental campaign, I received a valuable help from Carl-Magnus Midtbø, Børge Holen, Tore Andre Kristensen, Malin Alette Lervaag, Dag Breiby and his PhD students, and Di Wan. I owe to Di invaluable suggestions and discussion that have highly enriched my scientific background. I heartily thank Prof. Odd Sture Hopperstad and Torodd Berstad for the selfless and kind support, for the patience and the time spent in constructive discussions about the modeling part.

I had the pleasure to share my PhD routine with great colleagues, to whom I owe uncountable brain-preserving coffee breaks, fruitful discussions, great weekends and, above all, friendship. I would like to thank Sara Esmaeilian, Luigi Viespoli, Javad Sadeghinia, Victor André, Saveria Spiller, Mirco Peron, Pietro Foti, Javad Razavi, Chiara Zarna, Marco Turchetta, Sebastian Grans, Francesco Leoni, Camillo Bosco. I thank my office mates, for the spontaneous and various discussions, for the moments of happiness and frustration shared together.

Many more people have passed through this place, including master students, PhDs, visiting researchers and post-docs, and with many of them I had a very good time. I cannot list all of them, but I will always keep in mind the moments together, while looking forward to meet again in future.

A special thanks goes to Marco Maurizi for the priceless suggestions, for patient listening and for telling the right things at the right moment. Without his presence,

I would have given up my PhD halfway.

Furthermore, I am really thankful to my friends in my hometown for being capable of keeping a true friendship across the distance and for always finding some time to spend together, regardless of the limited occasions available and of my bad organization.

I am grateful to my parents for the support received across the distance and for always being there every time I went back. It is not an easy task to be good parents, and it does not happen to everyone to have good parents. I therefore consider myself lucky.

Finally, I acknowledge my colleague, friend and girlfriend Ambra. She has always been with me during this period and she tolerated every state of anxiety I have gone through, and every mess I have made. Despite everything, she was able to motivate, listen and support me always, while acting as the best inspiration of spontaneity and cheerfulness I could have ever desired for my life.

To my parents

Abstract

Flexible graphite (FG) is obtained by compaction of exfoliated graphite in the form of sheets having a thickness of 0.2 to 3 mm and density ρ from 0.7 to 1.9 g/cm^3. Sigraflex® is a commercial type of FG with $\rho = 1$ g/cm^3 employed as beam dumping material in the Target Dump External (TDE) cores of the Large Hadron Collider (LHC) located in Geneva, Switzerland. The performances of the TDE components are assessed by comprehensive FE simulations whose accuracy depends on the material parameters assigned to each component. In such context, this thesis aims to find the model and the necessary parameters for the mechanical simulation of the Sigraflex® core in the TDE.
At first, a review of Sigraflex® and FG properties available in literature will be presented: this will include the description of the microstructure, the collection of the mechanical and thermal properties, and their critical comparison with other well-known types of graphite. Then, an extensive experimental campaign will be reported. For the first time, the application of a Focused Ion Beam - Scanning Electron Microscopy (FIB-SEM) technique to FG for the quantitative investigation of the pores' sizes and shapes and the micro-sheets' thickness and arrangement, will be described. Moreover, the experimental setup and the mechanical properties obtained by in-plane tension, out-of-plane compression and nanoindentation tests will be outlined and thoroughly discussed. In particular, nanoindentation revealed to be an easy-to-use method to measure the orthotropic elastic properties of FG. Finally, although the focus will be mainly on the mechanical properties, a thermo-mechanical testing campaign will be presented, too.
Based on experimental observations, the behavior of FG will be assimilated to other well-known materials such as crushable foams and crumpled materials. A 1D analytical model will be proposed to decouple the deformation contributions from the graphite-like and crumpled-like behaviors, and the extension of the non-linear stress-strain behavior to 3D cases will be discussed. A practical solution will be to use a material model found in Ansys LS-Dyna library i.e., MAT_142 transversely crushable foam. Its suitability was investigated by means of 3D FE simulations of nanoindentation and the numerical force-displacement curves will be shown in comparison with the experimental curves. Although not exhaustive, the results are promising and can be considered as a reference point for future works on FG characterization.

Contents

Figures

Tables

1. Introduction

1.1 Background

The motivation behind this study has originated by the need to assess the operating conditions of the Large Hadron Collider (LHC) current design [1]. Specifically, the thermo-mechanical behavior of the low-density graphitic core in the Target Dumps External (TDE) blocks is of interest for increasing the future LHC energy deposition capabilities [2].

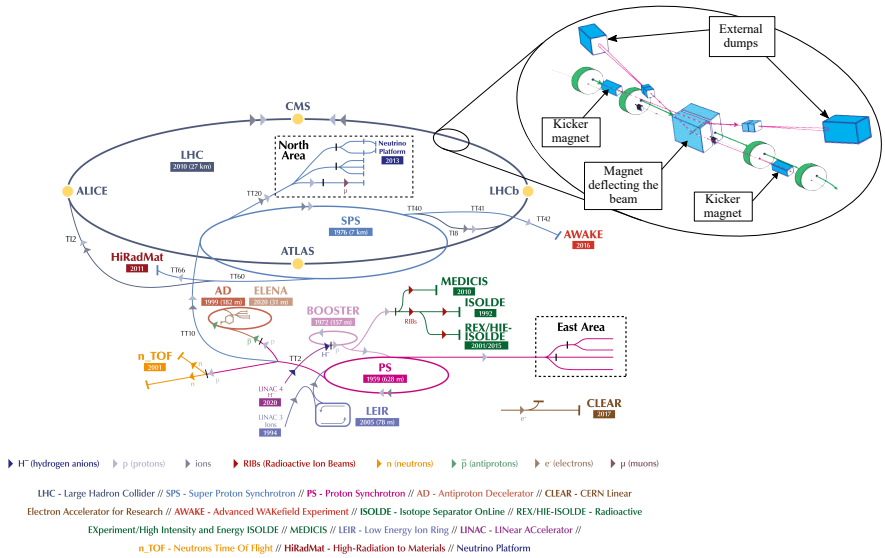

Figure 1.1: Large Hadron Collider facility overview [3] and external beam dumps also called Target Dump External (TDE) blocks (picture reworked from [4])

In the LHC (figure 1.1), two proton beams each one having 6.5 TeV/c energy counter rotate and collide in four different locations along the 27 km ring that correspond to four particle detectors. In this way, physicists can observe conditions similar to that of the Universe a few instants after the Big Bang explosion:

as an example, particles colliding at 1 TeV energy experience a state similar to that after 10^{-10} s after the Big Bang. This allows to explore the boundaries of Standard Model theories and different theories of particle physics, leading to new fundamental observations such as the measurement of the Higgs boson properties on 2012. As it is easily understood, the energy involved in this type of tests is enormous [5] and the LHC Beam Dump System (LBDS) is a critical section to ensure safe LHC operations: it consists of a fast extraction system that directs the beams out of the LHC circular trajectory to a tangential extraction line that is 700 m in length (magnification view in figure 1.1). This is done by means of a series of kicker magnets, at the end of which the Target Dump External (TDE) blocks are responsible for the safe absorption of the beam. The fast-pulsed dilution kickers sweep the high-energy focused beam in a quasi-elliptical spiral path to guarantee the energy spreading over the TDE core materials (figure 1.2).

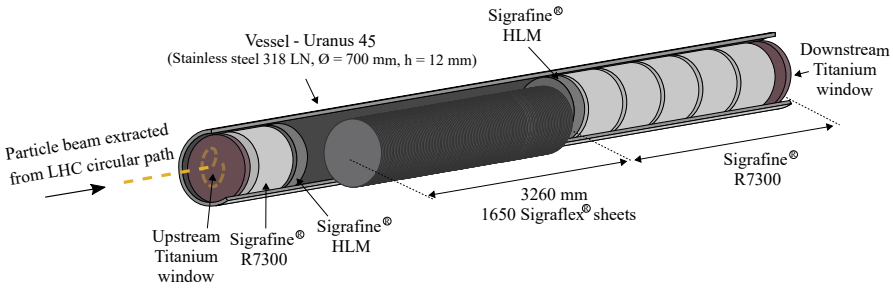

Figure 1.2: Schematic illustration of the TDE blocks graphitic core

As seen in figure 1.2, the core materials of the TDE are housed in a 318LN stainless steel vessel, sealed and filled with nitrogen gas. Inside, it consists of:

- 6 isostatic polycrystalline graphite blocks (SGL Sigrafine® 7300 [6]) 700 mm long with 1.73 g/cm^3 nominal density shrink fitted into a Uranus-45 vessel (length-by-diameter-by-thickness = 8500 × 722 × 12 mm^3),
- approximately 1650 SGL Sigraflex® [6] sheets (L20012C) as thick as 2 mm and with 1.2 g/cm^3 density. This is the low-density central section and also the focus of this work,
- two SGL Sigrafine® HLM plates [6], 80 mm thick with 1.72 g/cm^3 density, fixed to the vessel by two steel retaining rings,
- two Titanium Grade 5 windows enclosing the vessel.

The choice of graphite-based materials usage is due to the high performances with respect to beam absorption purposes since they are characterized by low atomic number and good thermo-mechanical performances at high temperature [7]. The temperature reached inside the core is indeed related to the impacted material density and, in this sense, the Sigraflex® section is the most exposed, also considering the energy increase expected in the current Run 3: a peak dose of 2.5 kJ/g in

nominal conditions and up to 4.1 kJ/g in case of dilution failure will correspond to 1500°C and 2300°C, respectively [8]. As a nominal reference, the expected working conditions of the Sigraflex® core are reported in Table 1.1.

Heating rate	10^8 K/s
Temperature max.	2000°C
Strain max.	0.13 - 2.6%
Strain rate	10^3 - 10^4 s^{-1}

Table 1.1: Nominal working conditions of the graphitic core

Sigraflex® is a commercial flexible graphite (FG) obtained by compaction of expanded graphite particles without any binder [9]. In figure 1.3 some real samples of L20010C grade provided by SGL Carbon[1] are shown. This material is porous and anisotropic with a carbon content above 98 – 99%. Its properties make it well-exploited in sealing and gasketing, also for thermal interfaces for cooling and insulation applications, often in sandwiched structures with stainless steel foils or in the shape of impregnated yarns. It shows some similarities with other types of graphites such as the well-known polycrystalline and pyrolytic graphite but differs in terms of micro-scale morphology and mechanical properties. It will be thoroughly described in Chapter 2 and actually, its characterization is the main goal of the present work.

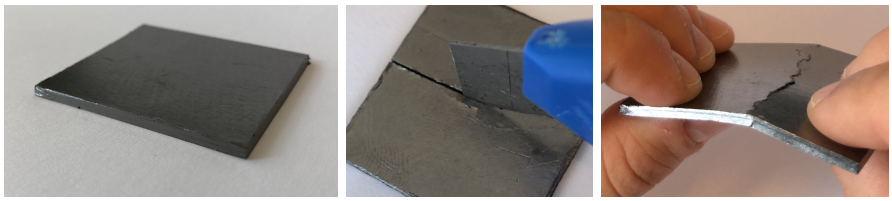

Figure 1.3: Some samples of Sigraflex® L20010C.

1.2 Thermo-mechanical problem

The beam impact generates a sudden energy deposition in the TDE materials that occurs in ∼86 µs and the subsequent thermal expansion of the impacted volume determines a dynamic multi-axial stress state in the volume and the surrounding region. A schematic representation of a proton beam impact is shown in figure 1.4. The beam has a gaussian spatial distribution around its axis and originates an axisymmetric temperature field in the impacted volume. Assuming adiabatic

[1] https://www.sglcarbon.com

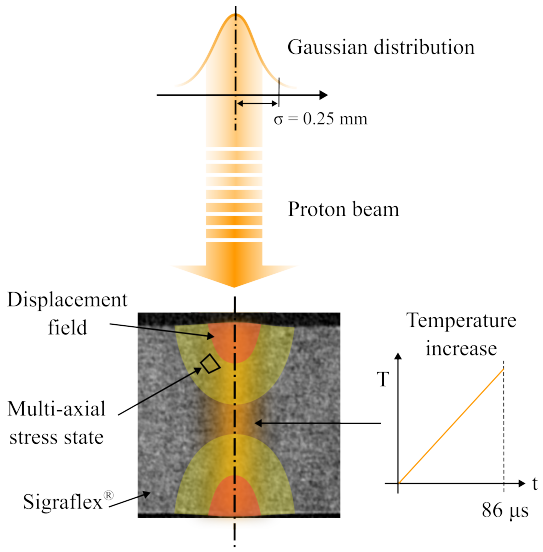

Figure 1.4: Schematic representation of a proton beam impact into a volume of Sigraflex® . This was reworked from a picture obtained post-mortem by computed tomography. The beam is gaussianly distributed around its symmetry axis with standard deviation equal to 0.25 mm. After the impact, the volume undergoes a sudden temperature increase and expands mainly along the beam axis direction.

conditions, the temperature evolution against time of a general body due to a volumetric heat source $\dot{q}$ is described by the heat diffusion equation:

$$\rho c_p \frac{\partial T}{\partial t} = \nabla \cdot (k \nabla T) + \dot{q} \tag{1.1}$$

where ρ is the density, c_p is the specific heat and k the thermal conductivity of the body. If the body is homogeneous and isotropic, the thermal diffusivity can be defined as $a = \frac{k}{\rho c_p}$ and represents a measure of the heat transfer rate from the hot to the cold ends.
The characteristic time constant is hence derived as $\tau = \frac{L^2}{a}$ where L is a characteristic size of the volume. If the deposition energy time is much shorter than τ, the temperature gradient over the volume can be neglected, the conditions are described as quasi-instantaneous and the temperature dependence on time is determined by the product ρc_p. Conversely, if the deposition time is much longer than τ, the conditions are quasi-static and the temperature distribution over the volume is mainly determined by k.
In any case, to a small temperature change ΔT is associated a change in volume ΔV due to the intrinsic thermal expansion coefficient. For an anisotropic material, this is treated as a second-order tensor with up to six independent components α_{ij} and links the temperature change to the thermal strains ε_{ij}^T in the 3D space

by:

$$\varepsilon_{ij}^{T} = \alpha_{ij}\Delta T \tag{1.2}$$

This relationship implies that a deformation occurs whenever a temperature gradient or a variation in the thermal expansion properties occurs. This is always the case for materials with finite thermal conductivity or inhomogeneities.
Duhamel and Neumann extended the Hooke's law to include such thermal contribution in the linear elastic constitutive equations by assuming that at each point of a solid body the components of stress-induced strain $\varepsilon_{ij}^{\sigma}$ and thermal strain ε_{ij}^{T} add up, such as:

$$\varepsilon_{ij} = \varepsilon_{ij}^{\sigma} + \varepsilon_{ij}^{T} = S_{ijkl}\sigma_{kl} + \alpha_{ij}\Delta T. \tag{1.3}$$

Here, ε_{ij} are the components of the total strain tensor, S_{ijkl} are the components of the compliance fourth-order tensor, and σ_{kl} are the components of the stress tensor. Equation 1.4 can be reverted to obtain the stress components explicitly:

$$\sigma_{ij} = C_{ijkl}\varepsilon_{kl} - C_{ijkl}\alpha_{kl}\Delta T \tag{1.4}$$

where C_{ijkl} are the components of the fourth-order stiffness tensor. This equation takes the name of linear thermo-elastic constitutive equation and neglects any dependence of the elastic constants C_{ijkl} and thermal expansion coefficients α_{ij} on temperature, as well as any inertial effect associated with the heating rate [10].
Expressed in this way and under the assumption of symmetry of α_{ij}, the unknown parameters in this equation are 27 and they can be reduced only if the impacted material presents symmetries such as transversal isotropy or orthotropy. Equation 1.4 is a very simplified case and is seldom of interest for real applications where the deformations are severe, plastic deformations occurs, and the material parameters are rate or temperature dependent. Then closed-form solutions to this equation are not available and the stresses must be predicted by Finite Element (FE) thermo-structural simulations.
Moreover, when the heating rate is severe, stress waves may arise and the material density may experience large variations depending on how much larger is the yield strength than the dynamic current stress. If the yield strength is much smaller than the dynamic stress, the material can be considered as behaving like a fluid, i.e. with strong predominance of hydrostatic stress states. In this extreme case an additional constitutive equation called *equation of state* would be requested to predict the stress state. This provides the evolution of pressure (hydrostatic component of the stress tensor) as a function of specific volume, temperature and energy and is solved by dedicated algorithms (hydrocodes) implemented in software such as AutoDyn [11] or Ansys®LS-Dyna [12].
In summary, the procedure used to evaluate the stress state on a beam-impacted material and hence assess the safety of a component such as the TDE, follow the classical scheme represented in figure 1.5 (see also [13] for a detailed example). At first, the energy distribution is converted to a temperature field by Monte-Carlo particle transport codes such as FLUKA [14]. This can be given as thermal load in input to a FE software where the necessary geometry has been previously

defined, bounded and meshed. The constitutive law for each material involved in the impact is usually based on experiments or literature data and attributed to a geometry representative of the real impacted volume. In the case of the Sigraflex® core, this may be a stack of sheets interacting among each other or a single homogeneous volume. The law may include the elastic constants, a yield function, the hardening parameters and their dependence on strain-rate and temperature, and a failure model. The thermal properties are also assigned as well as an equation of state, if needed. A simple example of constitutive law that the material may have at this stage is given by equation 1.4.
The model is eventually validated by experiments close to the real-case scenario such as the HiRadMat series [8, 13] and a failure model is employed to predict the life of the components and the maximum sustainable load.

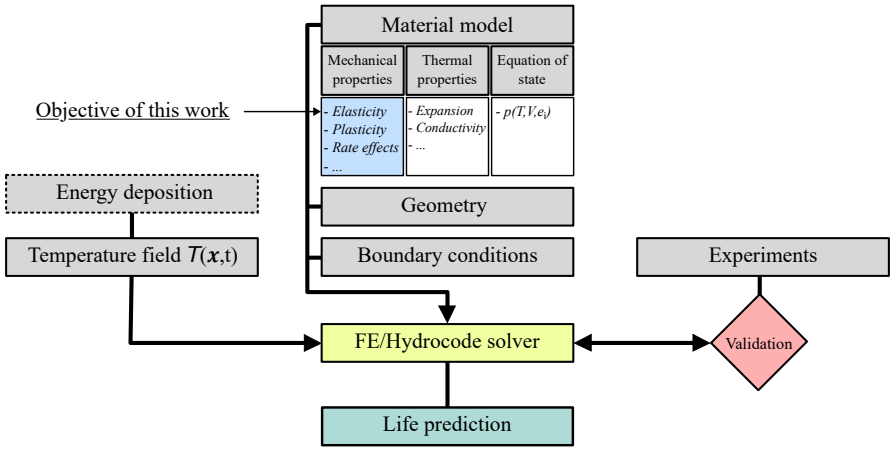

Figure 1.5: Procedure for the life prediction of the Sigraflex® core inside the TDE.

1.3 Challenges

The original goal of this work was to cover all the aspects related to the material model in figure 1.5, including the thermal and equation of state aspects. However, this was resized based on the observations listed below.
The application of Sigraflex® in the TDE dumping core is unique and largely deviates from the commercial spectrum mentioned in section 1.1. This is unfortunately reflected on a limited amount of experimental data available in literature or provided by the producers, often targeted to the only sealing applications. Some examples include monotonic static out-of-plane uniaxial compression properties, gas permeability measurements, thermal and electrical conductivity, and coefficients of thermal expansion as a function of the sheet density.
Moreover, since the properties are strongly affected by the density and by production process parameters such as chemical species, exfoliation temperature and

residual ash content, it is not straightforward to borrow the available data and apply it in the scenario considered here. In this sense, the type of Sigraflex® under the lens has 1 g/cm^3 density, whereas potentially useful data, not provided by SGL Carbon, can be found only for different brands FG such as Papyex® [15] and GraFoil® [16]. Or sometimes in works where the FG sheets were made in-house (see for example [17]).
For reasons that will be more clear with the reading of this work, the visual access to the material microstructure is hindered when the micro-sheets become too packed and, so far, any invasive attempt of cross-sectioning would affect the surface so that imaging techniques are not sufficient to collect quantitative data. Non-invasive techniques such as X-Ray Computed Tomography (also reported here in chapter 3) proved not to give sufficient resolution for accurate pore detection, but only for the monitoring of the deformation field under compression [18, 19]. The most complete microstructure description available in literature is from Celzard et al. [20] that went into details for exfoliated graphite compacts up to 0.3 g/cm^3 and the results cannot be trivially extrapolated to higher densities sheets.
In addition to the unknowns ascertained from the literature review, some additional questions arose from a general problem analysis and previous experimental observations:

- What happens when a so tortuous material is being impacted by a proton beam? Is the nitrogen (necessary for the inert atmosphere in the TDE) capable to flow out during the impact time or it expands internally contributing to the overall thermal expansion?[2].
- What is the characteristic size relevant to the problem? The protons have a gaussian spatial distribution with 200 - 300 µm standard deviation around the beam axis, but affects up to 15 mm volume radius around them [data provided by internal communication]. Sigraflex® instead is made of particles as wide as ∼100 µm, with the constitutive carbon planes oriented perpendicularly to the beam axis. Are the interlocking forces or the inner graphite structure that determines the stress-state during a single impact?
- Which kind of stress-strain constitutive law can be a good initial guess? FG is clearly a type of graphite, but the production process is different from e.g. polycrystalline or pyrolytic graphite, as well as some substantial differences are obvious in the mechanical response. Transversal isotropy in the elastic domain is a realistic assumption and the Young's moduli have been already investigated in some works, but no data are given about the yield strengths and Poisson's ratios. Not to mention about the plastic behavior, for which there is basically no previous proposals for a yield function or hardening rule.

[2]For further insight, compare figure 4 in [8].

1.4 Objectives

After the observations listed in the previous section, the original objectives had to be resized and the focus restricted only to the mechanical properties of Sigraflex® , i.e. the first member of equation 1.4. The research is therefore limited to the constitutive stress-strain relationship in static conditions without taking into account rate and temperature effects. A particular effort is put on the *classification*, that is, to which set of well-known models of similarly-behaving materials Sigraflex® can be assigned. These is meant to find a model that is already implemented in FE software such as LS-Dyna or Abaqus [21] and that could be quickly adapted to this application. A second objective is to find an experimental technique that could allow for the accurate observation and quantitative evaluation of the microstructure, including the size, shape and distribution of pores and micro-sheets. This could serve as a basis for a micromechanical model that could replicate the mechanical and thermal responses even when the latter is given by e.g. nitrogen expansion or structural re-arrangement of the micro-sheets. A third and last objective is to extend the technical know-how on mechanical testing of Sigraflex® and to understand which are the key mechanical properties that are of interest to this application. Most of the experimental data available regards the out-of-plane compression and in-plane tension of FG but they are barely sufficient even for the simplest material model. However, due to the fragility of Sigraflex® , the standard mechanical tests are not always the easiest solution and alternatives such as nanoindentation may represent the best way to go.

1.5 Publications and contributions

Conference papers

- E. Solfiti and F. Berto, 'Mechanical properties of flexible graphite,' *Procedia Structural Integrity*, vol. 25, pp. 420–429, 2020
- E. Solfiti and F. Berto, 'A review on thermophysical properties of flexible graphite,' *Procedia Structural Integrity*, vol. 26, pp. 187–198, 2020
- E. Solfiti, M. Calviani, A. Perillo-Marcone, J. Heredia, C. Torregrosa, A. Alvaro and F. Berto, 'Flexible graphite as beam dumping material in the TDE blocks of the large hadron collider,' *Procedia Structural Integrity*, vol. 28, pp. 2228–2234, 2020

Journal paper

- E. Solfiti, D. Wan, A. Celotto, N. Solieri, P. A. Munoz, R. F. Ximenes, J. M. Heredia, C. L. T. Martin, A. P. M. F.-X. Nuiry, A. Alvaro *et al.*, 'FIB-SEM investigation and uniaxial compression of flexible graphite,' *arXiv preprint arXiv:2304.04021*, 2023. Currently under revision in *Materials and Design* - Elsevier.

2. Literature review

2.1 Introductory comments

The publications available in the literature that address the microstructure, the mechanical and the thermal properties of FG or exfoliated graphite compacts, have been collected, reviewed and summarized in this chapter. The goals were:

- to understand FG and hence Sigraflex® microstructure including the characteristic sizes of particles, micro-sheets and pores,
- determine the suitable experimental techniques for its characterization,
- assess which material models could be used on FE simulations to best predict its behavior.

Most of the following information can also be found in [22–24] and in [25] (currently under review in *Materials and Design*[1]).
Mainly, Google Scholar[2] and Scopus[3] were used to search for scientific papers. Some data were also found in technical datasheets from different manufacturers websites.
The main challenge was represented by the fact that many authors attributed different names to the same material with the same density. For example, FG with 1 g/cm^3 was referred to as flexible graphite or natural graphite or expanded graphite. However, the name *natural graphite flakes* is mainly used for the ore material involved in the production of *expanded graphite* (also synonym of *exfoliated graphite*). Only at a later stage, this is compressed to obtain compacts of expanded graphite or flexible graphite.
FG was patented by Shane [9] in 1968, then Dowell and Howard [26] conducted a thorough characterization work in 1986 aiming to understand the microstructure and basic mechanical properties. In 2005, Celzard et al. collected in a comprehensive paper [20] many experimental results about the characterization of low-density graphite compacts, including modeling approaches of the pore space and micro-sheets arrangement. The PhD thesis of Cermak [17] was published in

[1] https://www.sciencedirect.com/journal/materials-and-design
[2] https://scholar.google.com/
[3] www.scopus.com

2020 and is among the most recent works concerning the mechanical and thermal properties of FG.
This review has been continuously updated since October 2019 until December 2022, but no relevant publications on mechanical or thermal properties were found after [17]. Many recent publications can be found about flexible graphite applied for example to fuel cell electrodes or sensors, but these will not be considered as relevant to this work.

2.2 FG microstructure

A visual summary of FG production process is given in Figure 2.1. It starts from natural graphite, a purely crystalline ore material in the form of plates and whose thickness and diameter measure around $10^1\mu$m and $10^2\mu$m, respectively [22]. Sulfuric and nitric acids are chosen as chemical species for the intercalation: they are able to penetrate among the basal planes and to expand rapidly upon heating so to push apart the carbon basal planes and obtain the exfoliated particles. Smaller is the thickness-to-diameter ratio of the flakes, longer is the path for the gaseous products to escape, and maximized is the final expanded volume [27]. Such particles are commonly referred to as *worms* due to their accordion-like shape and, thanks to their jagged profile, can be compressed together to create compacts or sheets with tailored density and thickness. Typically, compacts denser than 0.7 g/cm^3 and up to 1.9 g/cm^3 are referred to as FG whereas lower density materials are simply referred to as exfoliated graphite compacts or compressed expanded graphite. It is basically impossible to obtain densities higher than 1.8 – 1.9 g/cm^3 due to the difficulty on applying further irreversible work of compression [26].
The following nomenclature will be adopted throughout the text (see also Figure 2.1):

- natural graphite flakes: raw material made of purely crystalline graphite flakes,
- worms or exfoliated graphite: flakes after expansion,
- micro-sheets: stacks of tens of carbon basal planes. The skeletal structure of each single worm is a pile of corrugated micro-sheets,
- particles: worms intended as entities inside the compacted materials. They are flattened along the bedding plane,
- out-of-plane and in-plane directions: perpendicular and parallel to the bedding plane, respectively. Sometimes, the in-plane directions will be also refer to as directions 1 or 2, while the out-of-plane direction will be direction 3.
- compaction: the compression stage in the production process.

Furthermore, a bottom-up hierarchical order can be identified at different length scales: the carbon basal planes (nm) inside the micro-sheets (μm), the micro-

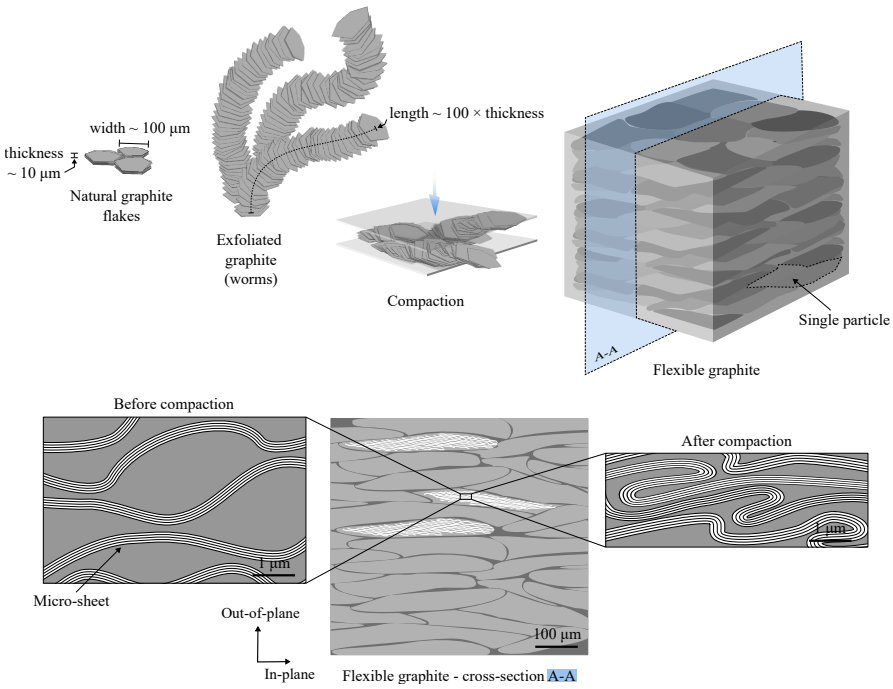

Figure 2.1: Production process of FG. The compaction stage is made by rolling compression up to $\rho = 0.7 - 1.9$ g/cm^3. On the bottom, the virtual cross section A-A of the final sheet highlights the presence of flatten particles having internal pores that deform severely under compaction.

sheets inside the particles (10 - 100 µm) and the interlocked particles as constitutive units of the bulk material (mm).
The uncompressed worms' density ranges around 0.004 - 0.015 g/cm^3 (corresponding to aporosity P > 99%) [20, 28] and their morphology depends on the initial flakes' size [29, 30] as well as on production process parameters such as maximum exfoliation temperature [27] and intercalant species [31]. Their final length can reach up to 100 - 300 times the initial thickness, whereas the width corresponds to the original width of the particles in the order of 100 µm. The cells are randomly dispersed along the worms' body, as a result of the expansion of the intercalant species [20], and have non-regular honeycomb shape. The single worm structure may be schematically seen as that of a foamy particle with open porosity space and cylindrical enveloping volume. The cells result from the corrugation of carbon basal planes that maintain the roughly circular perimeter and are averagely arranged perpendicularly to the cylinder axis. The degree of corrugation can be related to the degree of dispersion of chemicals and their consequent volatilization.
In [28], the typical sizes of the single cell (wall-to-wall) before compaction were

measured by SEM imaging in worms with three different densities (0.006 g/cm^3, 0.009-0.011 g/cm^3 and 0.004 g/cm^3) and were found to have ellipsoidal shape, with average aspect ratio equal to 0.5, major axis ranging between 21 to 32 μm and the minor axis between 10 to 16 μm. Pores as large as 100 – 200 μm were also reported at the distribution extremes. The wall thicknesses (that correspond to the micro-sheets thickness) could be inferred by nitrogen adsorption and specific surface area calculation in [20] and [32] and were found to be equivalent to 48 – 68 carbon basal planes i.e., $\simeq$ 16 – 22 nm. In [26] a higher estimate for the wall thickness corresponding to 30 – 60 nm was also estimated. The thickness-to-length ratio of a cell wall can be calculated from this data as $\simeq 20/20000$ [nm/nm] $= 10^{-3}$, which certifies the large flexibility thereof.

The orientation of the basal planes depends on the orientation of the micro-sheets during the compaction: Celzard et al. [20] reported that they are randomly dispersed at the early stage of compaction whereas Cermak et al. [17], upon X-ray diffraction measurements, showed that the basal planes of compacted FG are oriented only by 9 – 15° with respect to the in-plane direction. Likewise, the pores flatten out upon compaction: in [33], it was extrapolated that, at 1 g/cm^3, they must have disk-like shapes with the largest faces parallel to the same direction.

The pore space properties in compacts up to 0.3 g/cm^3 were thoroughly investigated in [20]. The Johnson, Koplik and Schwartz (JKS) theory was found to reasonably describe the electrical conductivity by assuming cylindrical pore shapes with equal lengths and diameters. Moreover, various parameters such as density, permeability and formation factor were related one each another by simple power laws. The pore network developed at the considered densities was described tortuous and increasingly anisotropic along with the density increase. In the same work, the porosity after compaction was described as the result of inter- and intra-particle contributions so that the bulk density and the particles density could be related in a linear relation. For example, when the bulk density reaches 1 g/cm^3, the particles are compressed from 0.015 g/cm^3 even up to 1.2 – 1.8 g/cm^3.

The JKS theory was also used in [34] for compacts with density from 0.0236 g/cm^3 to 0.35 g/cm^3; in this case the pore sizes decreased from 1.36 μm to 0.078 μm.

In [27], the pore sizes and permeabilities of 1 g/cm^3 material were investigated by mercury porosimetry and nitrogen adsorption-desorption experiments. Three different pore categories, related to their spatial scale sizes, were identified: macro-pores (80 nm), meso-pores (2-3 nm) and micro-pores (inter-crystalline cavities). The permeability analysis revealed a dominant orientation along the bedding planes so that the gas could penetrate in the in-plane direction 2-3 times faster than in the out-of-plane direction. In [35], the distribution of the transport pores size was investigated by nanopermporometer with hexane as filler of the porous matrix and nitrogen as the gas-carrier. The characteristic pore sizes were found to range between 1.5 and 6 nm.

Since the visual access to the pore network at such density is made difficult by sub-micron scale pore sizes, the amount of open or closed porosity at 1 g/cm^3 is

yet to be clarified. While Celzard et al. [20] found 30% closed porosity at 0.14 g/cm^3, Dowell and Howard [26] observed that the reduction of specific surface area upon compression of 1 g/cm^3 sample is not related to the creation of new closed voids. Toda et al. [18] inferred that the closed porosity volume fraction at 1 g/cm^3 is 8%, based on the rule of mixture of homogeneously distributed closed and open pores. In [27], the total volume occupied by macro-pores (pore size $\geq$ 40 nm) in 1 g/cm^3 specimens was obtained by the volume of intruded mercury at high pressure and resulted 0.51 – 0.48 cm^3/g. The total volume of meso-pores (pore size $\leq$ 40 nm) was measured in terms of outgassed nitrogen volume for 2h at 300°C. This was 0.03 – 0.08 cm^3/g. On the base of this data, the specific volume occupied by the pores can be easily calculated as well as the final porosity. The first is equal to 0.51 – 0.59 cm^3/g which means that the porosity is 0.51 – 0.59 for 1 g/cm^3. Then, if the total theoretical porosity is taken as

$$P = 1 - \frac{\rho}{\rho_s} = 0.56$$

where $\rho = 1$ g/cm^3 and $\rho_s = 2.26$ g/cm^3 is the density of crystalline graphite [36], the closed porosity can be confused within the uncertainty of measures, but cannot certainly overcome 9%.

2.3 Mechanical properties

The mechanical properties of FG may depend on several parameters: initial flake sizes, ash content, chemical intercalant species, exfoliated volume, density and thickness of the final product. Their influence will be discussed in this section.

2.3.1 Tensile properties

The tensile strength in the in-plane direction increases linearly with the bulk density increase, but the is not valid for the tensile strength in the out-of-plane direction (see figure 2.2a). Typical values of the tensile strength in the in-plane direction for 1 g/cm^3 are in the range 4 - 7 MPa (some higher values were solely reported by Sykam et al. [37]) whereas in the out-of-plane direction the uncertainty is larger. Only one work concerning this quantity was found [38] and the values obtained were around 0.02 - 0.03 MPa.
The crack due to in-plane tensile stresses was found to propagate along the particles, or clusters of particles boundaries. It outlined some boundaries even parallel to the loading direction and departing from different locations near the notch [30, 38]. It was therefore suggested that these clusters of particles, also called *structural units*, first rotate along the load direction and then slip until the final separation. The interlocking forces hence play a key role in the in-plane tensile deformation mechanism. Dowell and Howard [26] explained that they are generated by some links between the jagged boundaries whose number increases proportionally to

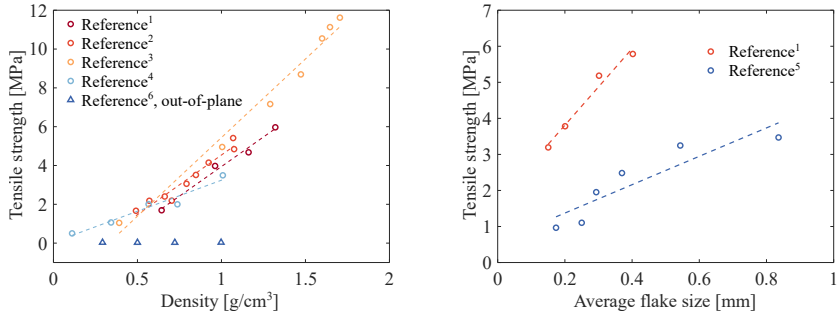

Figure 2.2: (a) Tensile strength dependence on bulk density and (b) natural graphite flake size. [1][30], [2][26], [3][39], [4][38], [5][40], [6][38] (measured in the out-of-plane direction).

the bulk density, and whose effectiveness depends on the initial relative misalignment of the micro-sheets. Higher is the misalignment, and more likely is to have an effective interlock. This is in turns a consequence of the quality of the exfoliation process and the initial flake size: in [30], it was indeed noticed that fully exfoliated worms, with final length up to 300 times of the original flake thickness, ensure a tensile strength increase. Larger flakes can also result on higher exfoliated volume and bigger structural units in which an eventual pull-out stress would be better hindered [31] (see figure 2.2b).
Not only, but also different intercalant substances like sulphuric acids result in larger pores, described as flat *baloons*, in the exfoliated structure and may in turn lead to larger particles [31]. Ionov et al. [41] noticed an effect of the intercalant species both on the absolute value of the strength and on the regression slope of the linear dependence on the bulk density. However, the effect of the exfoliated volume on the tensile strength is clearly visible only when the compound is considered as *fully* exfoliated [30].
The tensile strength may also depend on the ash content[4] of natural graphite: Dowell and Howard [26] for example found that to increase the ash content means to decrease the potential enhancement led by the density rise, while Savchenko et al. [42] extracted an increasing linear relation between the tensile strength and the ash content.
Typical values for the elongation at break in the in-plane direction are around 1 - 2%. However, the elongation at break along the in-plane direction was found to be markedly different between the axis parallel to the rolling direction and perpendicular to it. This was attributed to an higher tensile deformation during the the rolling process along the rolling direction, that may affect the maximum strain

[4]The ash content is the residue (mostly oxydes of metals) that comes from the extraction process of natural graphite and it is an index of the purity level of the flakes. It can affect the oxydation sensitivity of the FG and also the strength.

achievable upon reloading, as a sort of mechanical treatment, while the ultimate tensile stress remains unaffected [26].
The typical stress-strain curves of tensile tests can be found in [26, 37, 43] but the only attempt to carry out a simple constitutive model was shown in [26]. In this work, a simple power law of the type $\sigma = A\varepsilon + B\varepsilon^2$ was used to fit the stress-strain curve. The expression was originally proposed by Jenkins for the compression behavior of polycrystalline graphite [44] and was adapted for the tensile behavior. The fitting was however satisfactory only up to a half of the tensile strength. The in-plane tensile Young's modulus reported from [26] goes from 0.5 to 3 GPa, in accordance with 1.38 GPa extracted by Xi et al. [45] and with commercial data from FG furnishers such as SGL Carbon[5]. By visual inspection of the cyclic curves also reported in [26] and with the aid of the data on permanent deformation found in the Sigraflex® datasheet[6], it can be noticed that the deformation includes both elastic and plastic contributions but the transition between the two domains is not clearly visible. Concerning the underlying deformation mechanism, if some tensile forces are applied along the in-plane direction, the elastic modulus is expected to be initially controlled by the flexing and unwrinkling of the carbon planes, while only then, when the shear forces acting between the carbon planes reach a local threshold, an irreversible sliding occurs [30].

2.3.2 Compression and recovery properties

Compressibility and recovery are fundamental properties for sealing performances and are direct effects of the FG inherent resilience. Indeed, the production process is based on the application of compression to gain severe irreversible deformation until the desired density is achieved. The latter was related to the forming pressure p_f by an exponential law of the type $p_f = 0.35e^{2.6\rho}$ by Cermak et al. [46] for a density range from 0.2 to 1.7 g/cm^3.
Celzard et al. [20] explained that the material is isotropic at the beginning of the compression because of the worms and the micro-sheets random arrangement, while the degree of transversal isotropy and alignment increases with the compression increase.
Dowell and Howard [26] tested 1 g/cm^3 FG in the out-of-plane direction and applied out-of-plane cyclic compression up to 31 MPa. The material was observed to densify up to 1.73 g/cm^3 where no irreversible deformation was further possible. The concavity of the loading path was oriented upward, while the unloading-reloading behavior turned into a more and more linear trend. Some critical points were also highlighted: (i) the stiffness in compression increased with the misalignment of the basal planes, (ii) at high densities, the reversible work of compression was predominant on the irreversible work and (iii) the load carrying mechanism

[5] https://www.sglcarbon.com
[6] https://www.sglcarbon.com/en/markets-solutions/material/sigraflex-flexible-graphite-foil-and-tapes/

was entirely attributed to the bending of the carbon basal planes. In addition, the presence of two types of micro-structural regions was noticed: one with slightly oriented micro-sheets and well-aligned basal planes, probably responsible for the elastic compression response; the other with highly wrinkled micro-sheets and responsible of the inelastic response. Given by the predominance of creases that request for larger external work to increase the degree of folding, the second type of regions was also expected to give a stiffer contribution.
Similarly, Toda et al. [18] observed, by means of synchrotron X-ray microtomography with ZnO and WC marker particles, that the bending and the thickness reduction of the micro-sheets were the predominant deformation mechanisms upon compression loading, whereas the unloading was characterized mainly by thickness recovery. Leng et al. [30] hypothesized also an influence on the deformation mechanism from the air trapped in the pores. This was in agreement with Toda et al. [18] who argued that trapped air may also contribute to the behavior under recovery. It is not clear though to what extent such a small amount of closed porosity (< 9 %) discussed in the previous section, could influence so much the mechanical response.
Kobayashi et al. [19] adopted the same technique as [18] to observe the 3D strains inside 1 g/cm^3 FG during two cycles of out-of-plane compression. Some clusters of materials with average diameters equal to 100 – 150 μm showed similar deformation fields and were defined as *deformation units*. These owned rod- and sheet-like shapes, and presumably matched with the same entities mentioned as structural units in the analysis of Gu et al. [38] reported in the previous section.
The size of the natural flakes do not seem to have a remarkable influence on the compressibility[7] and recovery[8], but an increasing linear trend is also visible between the density and the compressibility [30].
Some typical uniaxial compression (engineering) stress-strain curves are reported in figure 2.3a for different FGs. The commercial types of FG were tested only at high loads so that the resolution at low loads is scarce. Here the concavity of the curve is upward with a strong stiffening at increasing stress. Cermak et al. [46] instead investigated the low loads response (maximum load $= 1$ MPa and maximum engineering strain < 6%) of FG at four different densities, i.e. 0.55, 1.05, 1.54, 1.7 g/cm^3, and reported a full elastic recovery with little hysteresis in all cases. The curve shape is also non-linear at the beginning with seeming linearization at increasing stress. The concavity is kept upward in the whole domain with tangent slope varying from 10 to 50 MPa. While the curves at high loads show a behaviour similar to that observed in materials that densify, such as foams, the low-loads behaviour reported in the inset of figure 2.3a appears unusual and needs to be further investigated. It is indeed unclear why the low-loads curve show an initial non-linear region that appears to extend if the material is denser. And furthermore, if one would obtain a comprehensive stress-strain curve

[7] taken as the nominal compression strain evaluated at a fixed pressure i.e., total strain
[8] taken as the nominal strain recovered i.e., elastic strain. Compressibility - recovery = plastic strain

putting all together, the only way would be to add a point of flex as conjuction between the low-loads and high-loads domain, which add a further questioning to the behavior. Other experimental curves can be found in [47] for high loads and in [48] for low loads.

Concerning other compression-related properties, both Dowell and Howard [26]

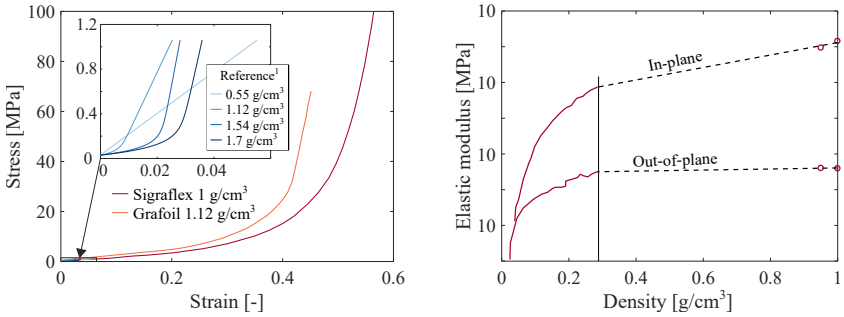

Figure 2.3: (a) Stress-strain curves at high loads from Sigraflex® datasheet and Grafoil datasheet®,[9]. Stress-strain curves at low-loads from [1][46], reproduced by means of the provided fitting parameters. (b) In-plane and out-of-plane moduli dependence on density from [33]: both of them follow an exponential relationship in the high density domain. The original data were converted from porosity to density by means of $\rho = \rho_s(1-P)$ where $\rho_s = 2.26$ g/cm^3. These data will be further reported for analysis in figure 3.19.

and Cermak et al. [46] reported that the transversal deformation under and after out-of-plane loading was negligible. For the in-plane compression instead, Krzesinska [33] measured the in-plane (dynamic) Young's modulus by ultrasound technique and found a value equal to around 4 GPa. The ratio between this value and the values found in [46] is $\simeq$100 and certifies an extremy degree of anisotropy.

A semi-empirical approach was proposed to fit the dynamic elastic modulus both in the high and low porosity regions (the latter being typical of FG foils). Defining E as the dynamic elastic modulus at the porosity P, E_0 as the Young's modulus at $P = 0$ and finally b as a parameter that quantify the effect of porosity on the dynamic modulus, the exponential equation $E = E_0 e^{-bP}$ is consistent in the low porosity region where $\rho > 0.3$ g/cm^3 (figure 2.3b) and, according to the values for b, it was supposed that the pores are roughly disk-shaped with the faces aligned to the bedding plane.

Finally, an attempt of modeling the FG compression response was done in [47] for 1.1 g/cm^3 FG. An hyper-elastic Blatz-Ko foam constitutive law was calibrated with the experimental data and then adapted to model a particular sealing configuration under high pressure.

[9] https://neograf.com/products/gaskets-sealants/grafoil-flexible-graphite

2.3.3 Other mechanical properties

Nanoindentation is a well-established technique for the characterization of several types of materials and distinctly suitable to extract the elastic modulus and the hardness of films, membranes or any thin specimen for which standard tests would be cumbersome. Chen et al. [32] employed nanoindentation to investigate exfoliated graphite compacts with density from 0.089 to 0.275 g/cm^3 and observed that the cell walls undergo very large recoverable shear deformation probably allowed from the sliding of the basal planes inside the cell walls.
Neverthless, Xiao et al. [34] modeled low density compacts with interfacial friction theory where each cell was considered as four Voigt elements in parallel, and showed that the contribute on the overall sliding stems primarily from the cell walls relative displacement. A single cell can give an engineering shear strain, and hence potential sliding and overall flexibility, up to 35 and up to 12 for compacts and FG with $\rho = 0.86$ g/cm^3, respectively [49]. This argumentation is valid for low density compacts, whereas the extrapolation is not immediate for FG since the viscous component may decrease strongly as the density increases [32].
Khelifa et al. [50] indented and simulated a commercial FG foil with 1 mm thickness and compared the results with experimental nanoindentation data. The constitutive equation used was that of an isotropic elasto-plastic material with power-law isotropic hardening. Among the coefficients, the yield strength found was 1.9 MPa, the (isotropic) elastic modulus was 190 MPa with assumed Poisson's ratio equal to 0.3. These values are significantly smaller than those owned by any other types of graphite e.g., the out-of-plane elastic modulus of single crystale graphite is 36.5 GPa [51] and for polycrystalline graphite ($\rho = 1.58$ - 1.97 g/cm^3), this is in the range 4.8 - 23 GPa [52]. Under the same assumed value for the Poisson's ratio, Chen et al. [29] found by nanoindentation that that the indentation modulus was 1.7 MPa for FG with 1 g/cm^3, in strong disagreemnt with [50].
Dissipative and visco-elastic phenomena in low density compacts have been largely studied in [49, 53–56]. The visco-elastic behavior of a material can be substantially measured by its *loss factor* $\tan\delta$ where δ is the phase-lag angle between the dynamic stress applied and the observed strain. The loss factor found by flexural tests of FG with density equal to 1.1 g/cm^3 spanned up to 0.187, while it was 0.019 or 0.021 for pure aluminum and Zn-Al alloy [53]. This strong viscous component becomes less relevant at higher densities where the layered microstructure is more hindered on allowing for relative sliding of micro-sheets.

2.3.4 Summary

A schematic overview of the values for the mechanical properties discussed along this section is shown in figure 2.4. Scarce data are available to properly define the main mechanical properties, also due to a large variation of these against density, different manufacturing techniques and parameters: a summary of numerical values for tensile and compression strengths are reported in table 2.1.

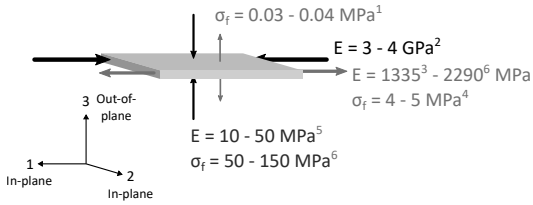

Figure 2.4: Visual summary of elastic moduli and yield strengths for 1 g/cm^3 FG. In-plane isotropy is assumed. [1]Data from [38], [2]Data from [33], [3]Data from [45], [4]Data from [24], [5]Data from [46], [6]Data from [26].

Reference	Density [g/cm^3]	Tensile strength [MPa]	Young's modulus [GPa]	Compressive strength [MPa]	Compressive modulus [GPa]	Poisson's ratio
[52] (polycr. graph.)	1.72 - 1.94	13.44 - 30.33	8.96 - 17.7	57.91 - 102.34	4.8 - 23	0.07 - 0.22
[26]	1	≃ 4	2.29	150	0.366 - 0.597	negligible
[30]	1.1	≃ 4				
[38]	1	≃ 3.5 (≃ 0.03 out-of-plane)				
[18]	1					0.04
[45]	1		1.335			
Sigraflex®	1	>4				
Grafoil®	1.12	4.5 - 5.2		165	0.166 - 0.2*	
[46]	1.05				0.01 - 0.05	negligible

*these values were taken for 1.4 g/cm^3 foils after unloading from 14 - 52 MPa compression stress.

Table 2.1: Mechanical properties (tensile properties in-plane, compression properties out-of-plane, Poisson's ratio as transversal deformation under out-of-plane compression)

2.4 Thermophysical properties

The thermal conductivity k, the coefficient of thermal expansion α and the specific heat capacity c_p of FG and exfoliated graphite compacts will be reviewed in this section. As mentioned in section 1.2, if a body is homogeneous and isotropic then these quantities are related one each other by means of the thermal diffusivity a as $k = \rho c_p a$ and can be used to solve many thermal problems by means of the heat equation 1.1.
Most of these properties were recently investigated by Cermak [17] that also compared the results of a large experimental campaign on FG with different densities with previous literature data. Here, the essential information will be reported in addition to some conceptual comments as appendices to the already exhaustive work mentioned.

2.4.1 Thermal conductivity

FG is transversal isotropic also from a thermal perspective. This means that the thermal conductivity can be defined both in-plane $k_{\parallel}$ and out-of-plane $k_{\perp}$ where $k_{\parallel}$ is expected to be greater than $k_{\perp}$ due to the preferred orientation of the carbon basal planes. Since the orientation depends on the micro-sheets re-arrangement and on the pore closures, a global indicator of the conductivity may be represented by the bulk density. As shown in figure 2.5a indeed, many authors employed different measurement techniques to observe that $k_{\parallel}$ increases linearly along with the density. Cermak et al. [57] also proposed a linear fitting for the data collected across density values from 0.55 to 1.7 g/cm^3.

Conversely, $k_{\perp}$ was observed in figure 2.5b to increase at low densities up to a

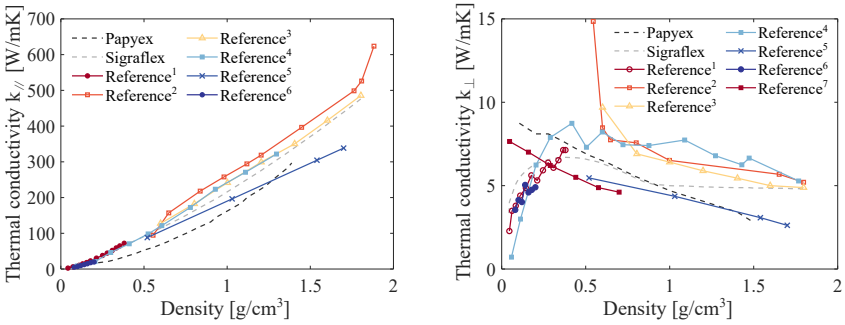

Figure 2.5: (a) Thermal conductivity in the in-plane and (b) out-of-plane directions against density: Papyex®[10], Sigraflex® , [1][58], [2][39], [3][59], [4][60], [5][57] (replicated from the fitting parameters provided), [6][61], [7][62].

turning point around 0.5 g/cm^3, and decrease afterward. $k_{\perp}$ indeed results from a trade-off between the increased number of contact points between the cell walls and the improved alignment of micro-sheets. The former is probably predominant at low densities where the material is still isotropic and the pore size decrease is beneficial for the out-of-plane conductivity. The latter is instead predominant at higher densities and, despite the increased number of contacts between the micro-sheets, the heat is more and more conducted only in the in-plane directions [39]. The ratio $\frac{k_{\parallel}}{k_{\perp}}$ is approximately 10 at 0.5 g/cm^3, 40 at a g/cm^3 and overcomes 100 at 1.8 g/cm^3. The increase is exponential with the density in analogy to the increase in the ratio between the in-plane to out-of-plane Young's moduli discussed in figure 2.3b.

Cermak et al. [57] further investigated the effect of out-of-plane pressure on the conductivity from 0.1 to 1.08 MPa of FG specimens with 0.55, 1.05, 1.55 and 1.7 g/cm^3. $k_{\parallel}$ was found to not be affected by the pressure in this density range,

[10] https://www.mersen.com/sites/default/files/publications-media/6-gs-papyex-graphite-souple-mersen.pdf

while $k_{\perp}$ showed slightly higher values at higher pressure. Interestingly, $k_{\parallel}$ and $k_{\perp}$ of FG specimens with 1.7 g/cm^3 density were initally more sensitive to the pressure increase, but the sensitivity decreased quickly above approximately 0.8 MPa. As noticed in the compression stress-strain curves in the inset of figure 2.3a, this stress value coincides with the end of the initial non-linear region and the beginning of the steep increase. This is interpreted as a connection between the micro-sheet orientation, that undergoes a stronger change at low loads determinant for the conductivity, and the non-linear shape of the stress-strain curve.
The conductivity is not only dependent on the density, but also function of the temperature. In this case, the change is mainly ascribed to a variation of the inherent crystalline properties and can be compared to other carbon-based materials. In figure 2.6, this comparison was done by observing the conducitivity of commercial FG ranging around 1 g/cm^3.
It is noticed that $k_{\perp}$ of commercial FG follows the same trend as $k_{\perp}$ of pyrolytic

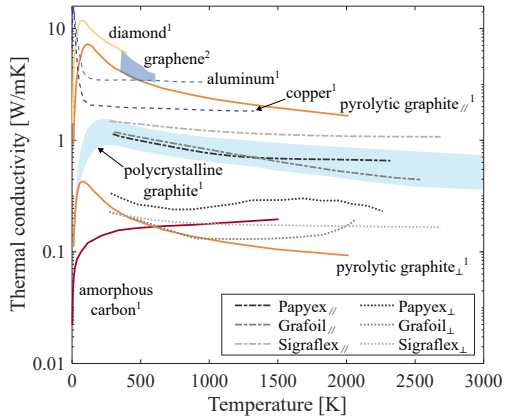

Figure 2.6: Temperature dependence of thermal conductivity: [1][63], [2][64]. Papyex® is another commercial FG with ρ = 0.7 - 1.1 g/cm^3, Grafoil® with ρ = 0.72 - 1.36 g/cm^3, Sigraflex® .

graphite. Probaly, $k_{\parallel}$ of FG with even higher densities would tend to match with $k_{\parallel}$ of pyrolytic graphite, which is similarly composed by strongly oriented carbon planes and clearly constitutes an upper bound for the conductivity.
$k_{\parallel}$ of commercial FG instead follows the same trend of polycrystalline graphite, that is considered much more isotropic than FG. The increasing-decreasing trend of $k_{\parallel}$ along with the temperature may be ascribed to the effect of lattice vibrations that is beneficial for the conductivity at low temperature but detrimental at higher temperature. Copper and aluminum own values higher than FG although in the same order of magnitude but they cannot hold the same working temperature of FG. Their melting point results equal to 1357°C and 933°C respectively [63], which is considerably lower than 2500°C of FG.
Many approaches about modeling of the thermal conductivity were presented in

literature. These often starts from the observation of micro-mechanisms of material compaction at very low densities. Celzard et al. [20] observed that there exist a critical density (at very low densities) for which a sudden increase of the conductivity. Around such threshold, the percolation theory was found to be adequate on modeling the conductivity and elasticity behavior using power laws of density such as

$$k \propto (\rho - \rho_c)^t$$

where ρ_c is the critical density corresponding to the threshold and t is a fitting exponent. At higher densities, corresponding to rolled commercial FG range, the material is assumed to be a binary mixture of air and solid part and some hypothesis are made about the pore shapes. The conclusions are obtained by means of analytical theory such as the effective media theory and JKS theory [20], or Hashin-Shtrikman upperbound for two phases compound [60]. In the latter case, the thermal conductivity of the overall compact can be expressed as a function of the thermal conductivity of the solid content k_s and the porosity $P = 1 - \rho/\rho_s$, with $\rho_s = 2.26$ g/cm^3:

$$k = k_s \left(1 - \frac{P}{2+P}\right).$$

k_s mixes the contributions from the in-plane direction and out-of-plane direction of the solid content to the thermal conductivity. This mixing approach seemed to fit the experimental data with a low error in a wide range of density up to commercial FG foils.
Chen et al. [62] compared the two approaches of Hashin-Shtrikman and the well-known rule of mixtures $k = v_s k_s + v_a k_a$ in the out-of-plane direction, where v_s and v_a are the volume fractions of the solid part and air, respectively, while $k_a \simeq 0$ is the conductivity of the air. While the rule of mixtures does not consider the changes in the solid content orientation during the compaction and considers the conduction path as uniformly oriented in the same direction, it could still to capture the trend along with the increasing density.

2.4.2 Specific heat capacity

No data are available in literature about the FG specific heat dependence on the temperature except for some data from commercial FG datasheets (figure 2.7). One value is given at room temperature by [60] and by [17]: these were $c_p = 850$ J/kgK and $c_p = 729.3$ J/kgK, respectively. Since FG has usually > 97 - 98% carbon content (even ≥ 99.85% for tailored thermal FG such as Sigraflex® TH[11]), the specific heat is basically the same as that of crystalline or polycrystalline graphite. Also Grafoil® declares a value of 711 J/kgK at 21°C, which is indeed quite similar to that of polycrystalline graphite at T = 19 - 25°C i.e., 704 - 720 J/kgK [65]. The

[11] https://www.sglcarbon.com/en/markets-solutions/material/sigraflex-high-purity-flexible-graphite-foil-and-sheets/

increase of c_p of polycrystalline graphite in the neighbourhood of room temperature can be considered as linear, whereas a polynomial fit of the type

$$c_p = 4184(0.538657 - 9.11129 \times 10^6 T - 90.2725 T^{-1} \\ - 43449.3 T^{-2} + 1.59309 \times 10^7 T^{-2} - 1.43688 \times 10^9 T^{-4})$$

is suitable when the range of T is extended from -23°C to +2726.85°C [66]. This fitting appears as suitable to model the specific heat of FG in the same range of temperature.
The behavior of copper and aluminum curves are markedly different from that of graphitic materials showing milder increments along with temperature.

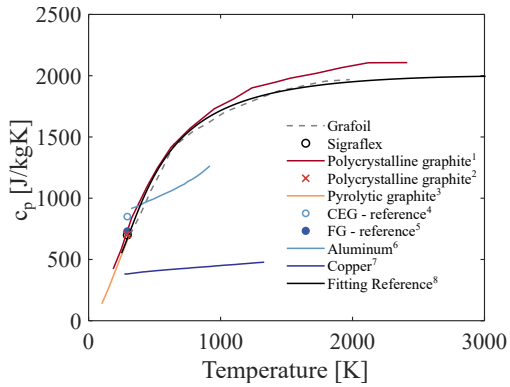

Figure 2.7: Temperature dependence of FG specific heat capacity c_p: Grafoil® with ρ = 0.72 - 1.36 g/cm^3, Sigraflex® 700 J/KgK at 20°C. [1][66], [2][65] 703.6 - 720.7 J/kgK at 19 - 25°C, [3][67], [4][60] 850 J/Kgk at 20°C and ρ not specified,[4][17] 729.3 J/KgK at 25°C and ρ = 0.55 - 1.7 g/cm^3, [6][68], [7][69], [8][66].

2.4.3 Coefficient of thermal expansion

The coefficient of linear thermal expansion α_T was probably the least investigated thermal properties before Cermak et al. [17]. This physical quantity arises from the lattice change effects due to the applied temperature: the increase in the carbon lattice distance in the c-axis direction is responsible for α_c and this appears much larger than α_a, even negative up to $\simeq$ 600 K. Riley et al. [70] proposed a model for the thermal expansion of crystalline graphite based on a relation between the hexagonal lattice vibrations (perpendicular and parallel to it) and the heat capacity at constant volume c_v defined as:

$$c_v = \frac{2}{3} c_{Va} + \frac{1}{3} c_{Vz},$$

where a and z refer to the directions parallel and perpendicular to the lattice, respectively. c_{Va} and c_{Vz} can be expressed as Debye functions D of the form

$$c_{Va} = 3RD\left(\frac{\Theta_a}{T}\right) \quad \text{and} \quad c_{Vc} = 3RD\left(\frac{\Theta_c}{T}\right)$$

where Θ_a and Θ_c are the two characteristics temperature referring to vibrations perpendicular and parallel to the hexagonal axis, respectively, and $R = 8.314$ J/-mol K. The Debye function in this case is expressed by

$$D\left(\frac{\Theta_a}{T}\right) = 3\left(\frac{\Theta_a}{T}\right)^{-3} \int_o^{\frac{\Theta_a}{T}} \frac{z^4 e^z}{(e^z-1)^2} dz.$$

The final model is then expressed by

$$\alpha_c = AC_{Va} + BC_{Vc} + CT \quad \text{and} \quad \alpha_a = LC_{Va} + MC_{Vc} + NT. \tag{2.1}$$

where A, B, C, L, M, N are fitting constants. In figure 2.8, an example of this fitting is shown together with data collected from literature in both the in-plane and out-of-plane directions. All the experiments involved pyrolytic graphite as tested material (the closest material to crystalline graphite). The constants A, B, C were taken from [71]:

$$A = 1.777 \times 10^{-7} \quad [\text{J/mol}], \quad B = -1.065 \times 10^{-7} \quad [\text{J/mol}], \quad C = 0 \quad [(^\circ\text{C})^2],$$

$$\Theta_a = 2280 \quad [\text{K}], \quad \Theta_c = 760 \quad [\text{K}].$$

While L, M, N from Tsang et al. [72] were preferred:

$$L = -5.05\times10^{-7} \quad [\text{J/mol}], \quad M = 1.4\times10^{-6} \quad [\text{J/mol}], \quad N = 5.15\times10^{-9} \quad [(^\circ\text{C})^2],$$

$$\Theta_a = 2300 \quad [\text{K}], \quad \Theta_c = 800 \quad [\text{K}].$$

These equations were found to follow the experimental data quite satisfactorily from 77 K to above 3000 K [71], though not respecting the limits imposed by thermodynamic principles in the neighborhood of 0 K i.e., α and its derivatives must approach zero as T tends to 0 K [73].

Mixing functions of the type $\alpha_x = \xi\alpha_c + (1-\xi)\alpha_a$ can be also employed to find α at a fixed temperature or in a temperature range assuming the mixing parameter ξ independent on T in a random direction x [77]. Alternatively, α should be considered as a tensor as in equation 1.2, where $\alpha_{11} = \alpha_{22} = \alpha_a$ and $\alpha_{33} = \alpha_c$ due to transversal isotropy.

FG data from different datasheets are also shown in figure 2.8 and result in good agreement with those of crystalline graphites in both directions when considering the average values taken in the temperature ranges shown. It must be noted that the subscripts c and a for graphite were deliberately confused with the out-of-plane and in-plane directions of FG to indicate the predominant orientations of the micro-sheets and the internal basal planes. The FG foils have very low expansion in

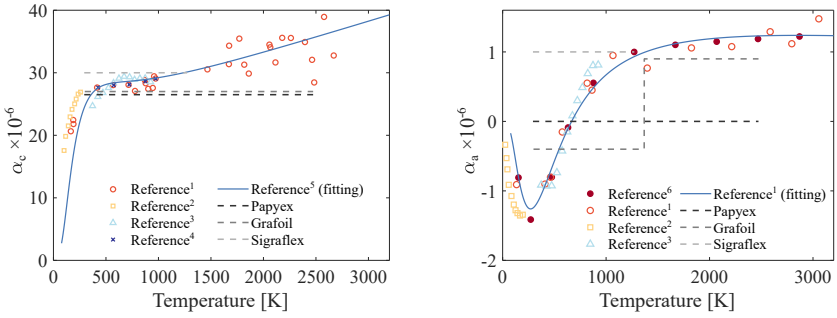

Figure 2.8: (a) Out-of-plane and (b) in-plane coefficients of thermal expansion from datasheet of commercial FGs: Papyex® with ρ = 0.7 - 1.1 g/cm^3, Grafoil® with ρ = 0.72 - 1.36 g/cm^3, Sigraflex® , and from literature: [1][71], [2][74], [3][75], [4][70], [5][72], [6][76].

the in-plane directions, even negative, similarly to crystalline graphite. In Grafoil® datasheet is explained that at first the foil shrinks (negative α_c) up to 1095°C due to the relieve of residual stresses of previous compression, and then slightly expands, but the phenomen could also be explained as a natural effect given by the properties of the crystalline lattice.
Likewise for the thermal conductivity, Cermak et al. [17] measured the variation of FG thermal expansion along with the initial density. This was reported here in figure 2.9 by means of the fitting equations representing the average values at four density values i.e., 0.55, 1.05, 1.54, 1.7 g/cm^3:

$$\alpha_\perp = -119\rho^{-0.151} + 142, \quad \alpha_\parallel = -0.132\rho^{3.46} - 0.6.$$

The measurements were executed from 0 to 100°C at the heating rate of 0.07°C/s. As observed, the in-plane expansion is always negative and tends to increase in absolute value with increasing density. Similarly, the out-of-plane expansion remains positive and increases in absolute value at increasing density. Since no variation was found on specimens with different thicknesses but same density, it was suggested that the expansion is independent on the specimen thickness. Although it is intuitive for many FG properties that at higher density the similarity with crystalline graphite is increased, this may not be valid for the thermal expansion, too. Observing figure 2.9, it seems that at 1.7 g/cm^3 the thermal expansion is already higher than graphite (both in-plane and out-of-plane if considering the absolute values), but the uncertainty of the measurements do not allow to get to any certain conclusion.
The density-dependence of FG thermal expansion suggests a probable involvement not only of the carbon mirco-structure, but also of the micro-sheets meso-structure on the thermal expansion. The meso-structure comprises the geometry created by micro-sheets folds and wrinkles and it is realistic that the geometrical

effects may affect the overall thermal expansion to make it, for example, larger in the out-of-plane direction or even rate-dependent.
Further investigation is needed to explain the origin of the Sigraflex® behavior reported in [8] and to further decouple it from possible contributions of trapped gaseous substances.

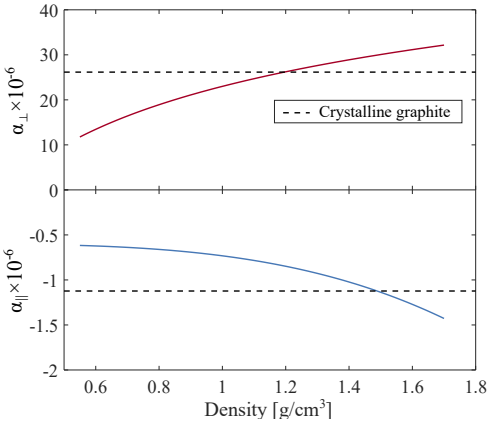

Figure 2.9: Density dependence of the coefficient of thermal expansion [17]. This was compared with an average value of α_c and α_a obtained by averaging equations 2.1 in the range 0 - 100°C.

2.4.4 Other thermal properties

Dowell and Howard [26] reported a reduction on the ultimate tensile strain after one hour heat treatment at 1750°C by a factor of 0.6 whereas the strength increased by a factor of 1.2. The compressive modulus (tangent at 6.9 MPa out-of-plane pressure) was found to decrease from 366 MPa to 178 MPa after 1 hour of heat treatment at 2750°C. Thus, thermal treatment appears beneficial for the tensile strength, while improving ductility upon compression.
In general, crystalline graphite does not have a melting point at a pressure of 1 atm. It directly sublimes at approximately 4000 K and, for the triple point to be observed, a pressure of 100 atm and 4200 K are needed. However, the reaction to oxygen and combustion occurs at much lower temperature in air i.e., at 350 - 400°C. The oxides obtained are gaseous and do not form as in many carbides a protective oxide layer to delay the oxidation [36]. It follows that FG with pure carbon content without any residual metal oxides could both avoid the burn-out at high working temperature and also improve the overall strength [26, 42]. That is also one of the reason why Sigraflex® TH grade should be preferred in high temperature applications [private communication with SGL Carbon].
The electrical conductivity σ_e has in general a strong relationship with the thermal conductivity. For metals this is usually described by the well-known Wiedemann-

Franz law:

$$k = LT\sigma_e$$

where L is the Lorentz number whose values for metals is equal to $2.44{\cdot}10^{-8}\mathrm{W\Omega/K^2}$. Similar relations have been carried out for different types of graphites, for example

$$k^{-1} = 2.93 \cdot 10^{-3}\sigma_e^{-1} + 0.34$$

that works for graphitised coked based materials and pyrolytic graphite [78, 79]. Typical value of L for polycrystalline graphites is $1.2{\cdot}10^{-6}\mathrm{W\Omega/K^2}$ [80] whereas for pyrolytic graphite in the in-plane and out-of-plane directions is respectively $2.9{\cdot}10^{-6}\mathrm{W\Omega/K^2}$ and $5.4{\cdot}10^{-5}\mathrm{W\Omega/K^2}$ [62].
Regarding FG, the results in [39] gave L values from 5.6 to $6.2{\cdot}10^{-6}\mathrm{W\Omega/K^2}$ and a final fit in the shape of a sigmoidal regression at room temperature as follows

$$\lambda = 1168.4e^{-\frac{1}{3.5\sigma_e}} + 102.2.$$

Chen and Chung [62] found a linear relation among the electrical and thermal conductivity in the out-of-plane direction corresponding to $L = 7.3{\cdot}10^{-6}\mathrm{W\Omega/K^2}$.
FG also inherits from graphite properties both a certain degree of thermoelectric power and piezoresistivity. The first was quantified by [81]: a temperature gradient was generated at the surface of a 1.1 $\mathrm{g/cm^3}$ FG specimen in the out-of-plane direction at slow heating rate and the voltage difference was measured. This raised in a linear manner with a slope equal to -2.6 μV/°C. The piezoresistivity was investigated by Xi e al. [45] who observed an increment of electrical resistivity above 30% when the material is stressed up to 3.18 MPa. In the latter work moreover, the behavior of FG as electret and piezoelectret element has been reported for the first time.
A thermal property also relevant to the application of this thesis, is the thermal contact resistance. Due to the good compliance ability that stems from the porous microstructure, FG foils are indeed good thermal interface materials. It was underlined by Gandhi et al. [82] how the contact pressure can modify it depending strongly on the application: increasing the contact pressure leads to a minimization of the resistance, but overcoming such value can deform the surface and lead to an increment of that.
Marotta et al. [83] showed how to model the contact interface problem for FG used as interstitial material. The thermal resistances can be modeled in a spring series model, considering an applied temperature variation ΔT and the heat flux Q. The resistances are ascribed to the non-effective contact area, to the medium present in the gaps between the contact points and to the bulk material itself. The equivalent thermal resistance is defined as thermal joint resistance and it was shown to be function of the applied pressure and thickness of the interstitial material. The data shown for eGraf[12] suggested that, regardless of the sheet

[12]This is a commercial grade of FG and information can be found in `https://neograf.com/products/thermal-management-solutions/egraf-hitherm-thermal-interface-materials`, although Marotta et al. [83] reported that the trademark is from Graftech, Inc.

thickness, increasing the pressure from 50 to 500 kPa, leaded to a decrease of the thermal joint resistance by 5 times.
The bulk resistance is instead only a part of the total joint resistance and this was reported by Smalc et al. [48] for FG (eGraf, 0.13 mm thickness) to be 30 ± 0.05 mm^2 °C/W at 100 kPa applied pressure (and 162 ± 0.08 mm^2 °C/W thermal joint resistance). This data were obtained by stack of three specimens under the assumption that the individual specimens coalesce together under pressure and thus making the contact resistance between them negligible. This was checked by measuring the thermal joint resistance of single and stacked specimens as shown in figure 2.10. All the results for one, two or three stacked specimens of two different thicknesses lies on the same regression line or even overlaps, showing that even at 100 kPa pressure, the gap between the sheets is irrelevant.

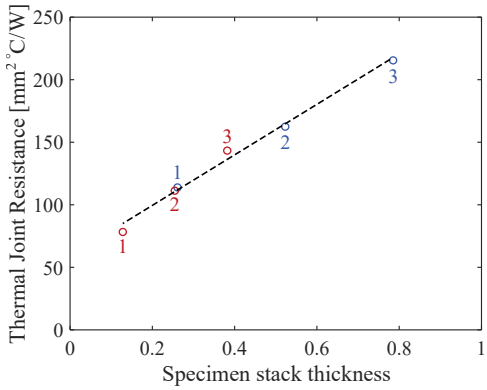

Figure 2.10: Data reworked from Smalc et al. [48]. The numbers close to the corresponding number indicate the number of single specimens stacked. The x-axis indicates the total stack height.

3. Experimental campaign

3.1 Material datasheet

This chapter reports the experimental campaign carried out on Sigraflex® L20010C[1] provided in form of sheets with 1 g/cm^3 density, 2 mm thickness and 2% ash content. Some relevant properties are reported in Table 3.1. Although type L20012C is currently being employed in the TDE, type L20010C is considered for application in the future TDE design mentioned in the Introduction.

Foil size	$1000 \times 1000 \times 2$ mm^3
Density	1 g/cm^3
Ash content	≤ 0.15 %
Elongation at break(in-plane)	> 1 %
Tensile strength (in-plane)	$\sim$4 MPa
Specific heat (20°C)	0.7 J/Kg K
Coeff. of thermal expansion (20 - 1000°C)	1×10^{-6}K^{-1} (in-plane), 30×10^{-6}K^{-1} (out-of-plane)
Thermal stability	-250 to +3000°C (up to +400°C in presence of oxygen)

Table 3.1: Sigraflex® L20010C datasheet properties.

3.2 FIB-SEM investigation

3.2.1 Motivation

The pore sizes estimated by means of gas or fluid flow experiments are not always straightforward to be employed in the material structural modelling and they cannot unveil properties related to the deformation micro-mechanism. Characterization through visual inspection can instead lead to a quantitative description of the microstructure properties such as pore sizes and orientations, giving results suitable for statistical analysis and micro-mechanical modelling. SEM imaging of FG

[1] https://www.sglcarbon.com/en/markets-solutions/material/sigraflex-flexible-graphite-foil-and-tapes/

fractured sections was already reported in [17, 26, 38] but no attempt to extract quantitative properties was reported in any of the reviewed works.
FIB-SEM tomography is by now an established technique to obtain 3D information on different materials but the applications in carbon-based materials are still limited, especially for quantitative reconstruction purposes [84]. The accuracy of the extracted microstructure properties relies on the capabilities of segmentation algorithms which should be capable of discerning solid phase from the pores. This can be challenging in highly porous media where shine-through artifacts and curtain effects are more likely to occur and generate ambiguities after image binarization [84, 85]. For these reasons, and since no data were available from previous works on FG, the investigation was limited and optimized on a single section as well as the image processing was focused on the only bi-dimensional pore properties. The following section is part of a publication currently under review [25].

3.2.2 Methods

A transversal cross-section of a FG specimen free from any production process marks was cut by Ga^+ Focused Ion Beam microscope. The surface was first prepared by platinum deposition along the top edge of the desired section. This was meant to be sacrificial for the cross-sectioning while limiting the tail and curtaining effects by levelling of the superficial asperities.
Then, the section was milled by ion sputtering (30 kV, 65 nA) along parallel stripes, at increasing depth, from the surface down to approximately 100 µm. An ion current of 2.8 nA was adopted in the last milling step to finely smooth the surface. The final section was rectangular with sides of 100 µm × 150 µm, perpendicular to the slicing direction as in figure 3.1.
The images that accurately captured the pore structure and the regions less subjected to curtaining were analyzed in MATLAB® using Image processing Toolbox^{TM} functions. The anisotropic diffusion filter was used to lower the noise while preserving the edges, and the marker-controlled watershed algorithm was exploited for pore detection. Morphological operations improved the analysis and manual intervention was sporadically needed to discard poorly detected pores, sometimes confused with dark artifacts in the denser material domains. Moreover, the material was visually split in two phases (dense and coarse) by direct crop of the image FFT followed by thresholding of the reconstructed image. The best parameters combination was found by recursive attempts comparing the trend of the total porosity affected by each of them.
The radii of the maximum inscribed circles R_{ins} were calculated as the maximum of the distance transform per each pore binary image and used for the definition of the aspect ratio $AR = R_{ins}/R_{max}$ where R_{max} was taken as a half of the maximum Feret diameter. All the quantities calculated were converted to the metric system by pixel proportion.

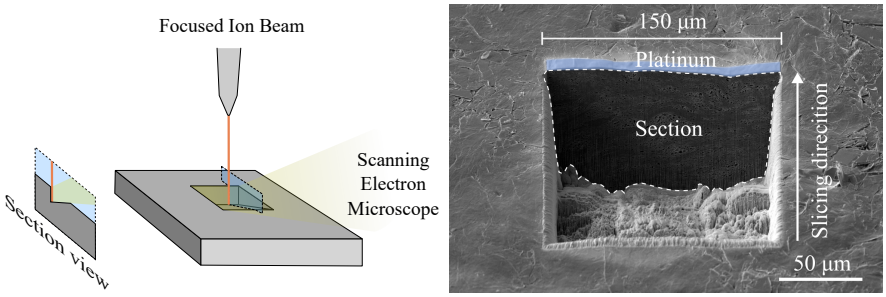

Figure 3.1: (a) Schematic illustration of the section obtained by FIB-SEM and (b) top view of the actual section.

3.2.3 Results

The corrected view of the whole section is reported in figure 3.2. Despite the curtain effect due to the high porosity, the microstructure is much more evident than in tension-fractured specimens images such as those ones reported in detail in [17] or on the right side of figure 3.2. Two types of regions can be identified by visu-

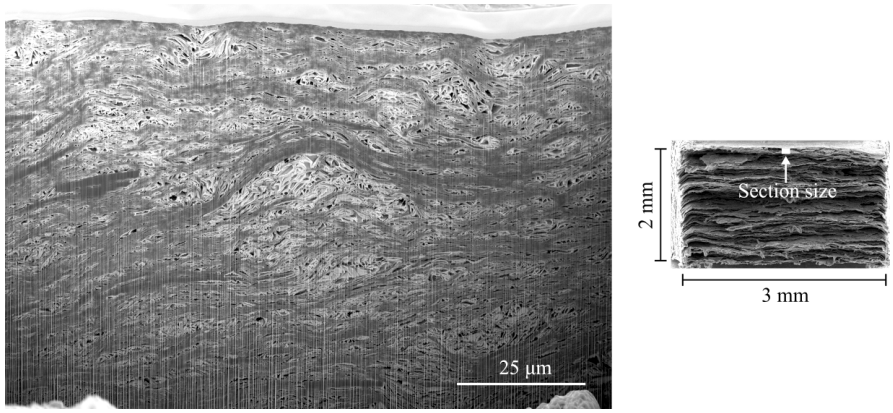

Figure 3.2: Schematic illustration of the section obtained by FIB-SEM together with its relative dimensions with respect to the whole specimen dimensions. The image on the right was obtained by applying in-plane tensile forces as described in section 3.4.

ally separating darker and brighter spots. The former have stripe-like shapes with tiny pores and tend to run perpendicularly to the compaction direction; the latter show larger pores with very misaligned walls and shiny features. Such distinction becomes more evident at increased magnifications such as in figure 3.3. The darker regions are composed of several compacted layers attributed to bundles of micro-sheets (figure 3.3b). The micro-sheets are well-aligned with each other and

are separated by thin and elongated pores. The contact lines visible in figure 3.3d help to visually follow the micro-sheets profiles and could be attributed to totally compacted pores.
The micro-sheet's thicknesses did not show big variation in dimension when manually measured by pixel proportion. These ranged between 40 to 120 nm that correspond to 120 to 360 carbon basal planes: at least twice than the values predicted by nitrogen adsorption and specific surface area estimation [20, 32]. In the transition between the two regions (figure 3.3c), the micro-sheets deviate from the aligned state and branch out with continuity until becoming pore walls.
The relative interlocking between neighbouring worms is so effective that any discontinuity amenable to the particles' boundaries was not detected. Due to the sheets' extreme flexibility, the particles withstand large deformations without failure so that during compaction they can fold into themselves and collapse creating very non-regular pores' contours. This confirms the observations made in [26] about the presence of two types of regions, one with slightly oriented micro-sheets and one with highly wrinkled micro-sheets, each related to a different deformation response upon uniaxial compression load. In the following, we will refer to the oriented micro-sheets regions as *aligned regions* whereas to wrinkled regions as *misaligned regions*. The pores detected in the imaged domain are highlighted

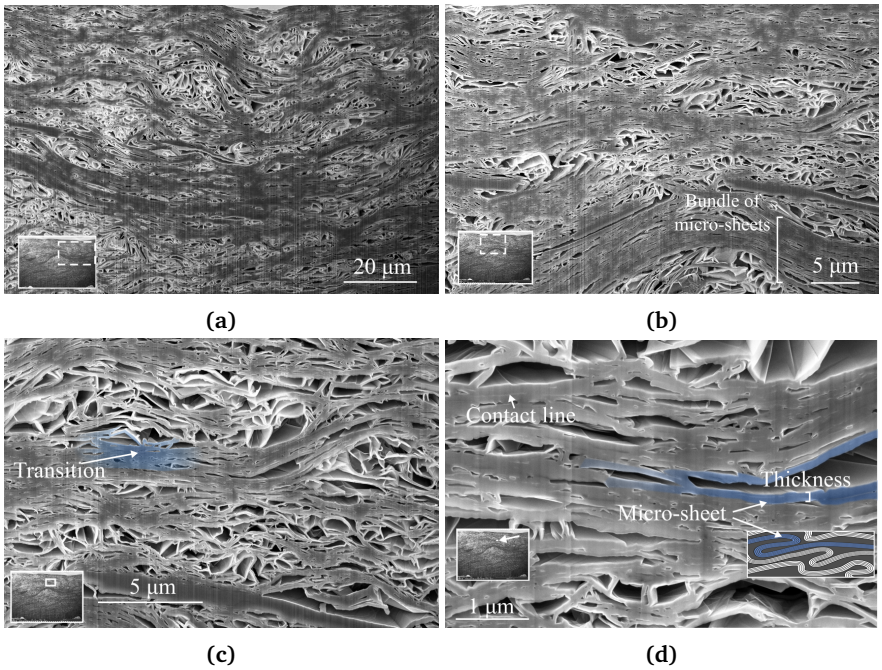

Figure 3.3: microstructure of Sigraflex® : magnified views.

and overlapped to the original image in figure 3.4a. Despite the accuracy of the

measurements was checked by visual assessment, it was obvious that the most accurate results were obtained for medium-size pores. Large pores' boundaries indeed were affected by ambiguous features visible in the internal pore walls and often resulting in the areas underestimation. Smaller pores conversely could be confused in the noisy and dark shades of the hard regions.
In total, 2681 pores were identified within an area of $27.62 \times 41.47 = 1145.5$ μm^2, resulting in a local 2D porosity of 0.15 ± 0.05 averaged over and including all the tested combinations for the image analysis algorithm parameters. The limited size of the region together with the 2D nature of the investigation can explain the big discrepancy with the overall material porosity ($P = 0.51 - 0.55$). Not only, but also the density gradient along the sheet thickness predicted in [60] i.e., denser material on the sheet surface, can be considered as a suitable explanation for such discrepancy.
The aligned and misaligned domains were separated (see figure 3.4a and 3.4b) so that the pores' properties could be assessed separately per each domain.
The different combinations of the algorithm parameters, such as the cut-off frequencies of the passband filter and the grayscale thresholds, were tuned until the binarized regions satisfactorily overlapped the aligned and misaligned regions, considered as complementary. The area fraction of the aligned phase ranged between 0.42 and 0.55, with an average value of 0.49. Its porosity was calculated as the summed areas of all the pores falling within this region with more than 50% of their pixels. The value obtained at 0.49 area fraction was 0.051, one order of magnitude lower than the porosity of the misaligned phase that instead was 0.24. The number of pores was almost equally distributed between the two phases i.e., 1459 for the misaligned phase and 1222 for the aligned phase, but the misaligned phase contributed to the 85% of the overall porosity volume.
The radius of the maximum inscribed circle R_{ins}, the half of maximum Feret diameter R_{max} together with their ratio AR (figure 3.4c-d-e) were used to describe the size and shape of the pores. On average, the values of R_{ins} and R_{max} of the misaligned region pores were larger than the hard phase pores, whereas the AR distributions were identical meaning that the main difference between the two phases was mainly about the pore sizes. This was better quantified by the equivalent radii R_{eq} distributions in figure 3.4d which shows that despite the continuous spectrum of values, the two logarithmic distributions would tend to decouple. Fitting them as log-normal distributions, the expected values for R_{eq} are 0.145 μm and 0.0693 μm, corresponding to an area of 0.066 μm^2 and 0.015 μm^2, for the misaligned and aligned phases, respectively. The pores in the misaligned regions were therefore more than 4 times bigger than the pores in the aligned regions. Gathering all the data under the same distribution, the average values for all the pore parameters were obtained and reported in table 3.2.

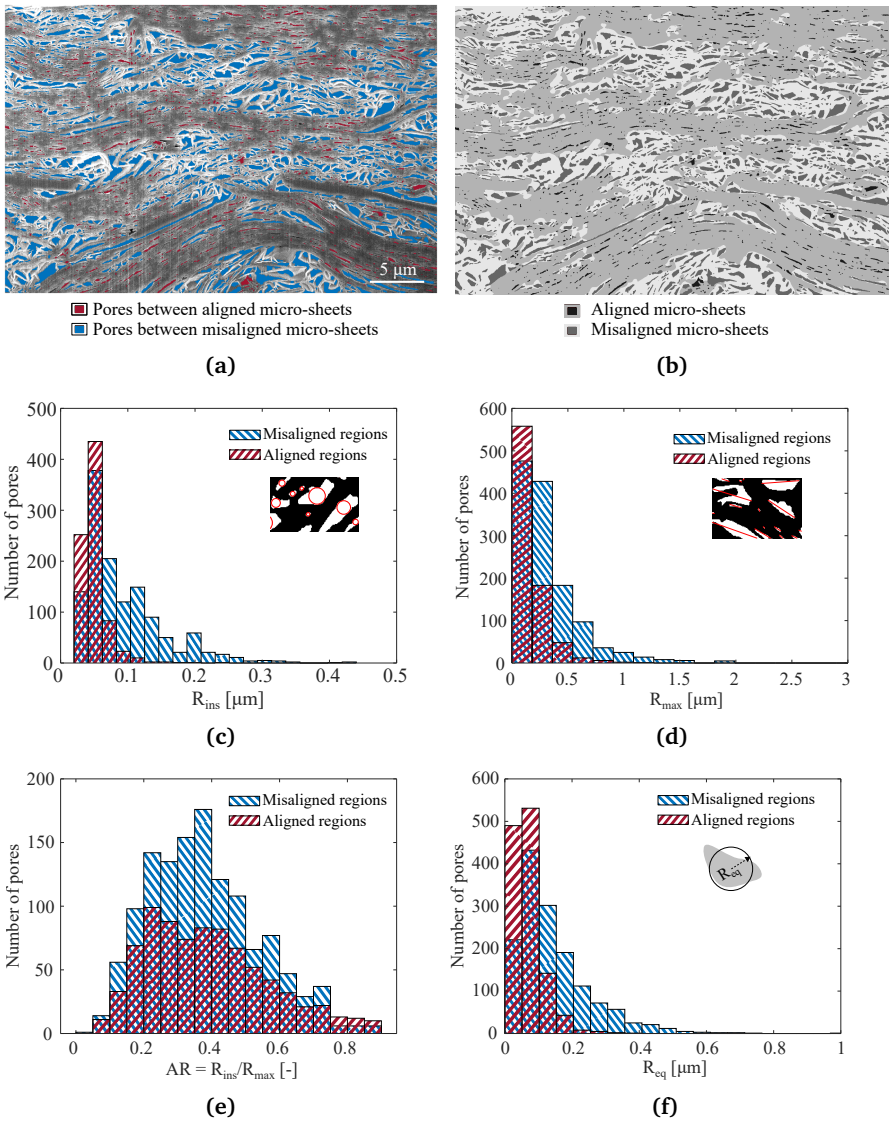

Figure 3.4: Results from image analysis: (a) pores as obtained by watershed segmentation, highlighted, and overlapped to the original image, (b) hard and soft phase distinction as obtained by image FFT cropping and thresholding, (c) maximum inscribed circle radii R_{ins} distribution, (d) half of maximum Feret diameter R_{max} distribution, (e) aspect ratio AR distribution, defined as fraction of the previous two quantities and (f) pore equivalent radii distribution.

	Regions		μ		σ		Expected value [μm]	
R_{eq} [μm]	All	Misaligned Aligned	-2.216	-2.198 -2.8219	0.5776	0.7319 0.5528	0.129	0.1451 0.0693
R_{ins} [μm]	All	Misaligned Aligned	-2.68	-2.495 -2.9727	0.522	0.5374 0.3272	0.0786	0.0953 0.054
R_{max} [μm]	All	Misaligned Aligned	-1.616	-1.422 -1.923	0.7234	0.74 0.577	0.2581	0.3171 0.1727
AR [-]	All	Misaligned Aligned	-1.064	-1.0729 -1.05	0.4815	0.4721 0.496	0.3875	0.3824 0.396

Table 3.2: Mean values of all pore parameters considered as single log-normal distribution

3.2.4 Observation of detached particles

This section reports an additional investigation performed on some particles that were pulled apart from the specimen surface by means of simple "scotch tape" technique. This technique is often used for graphitic materials to induce exfoliation and delamination (see e.g. [86]). The particles detached from the specimen

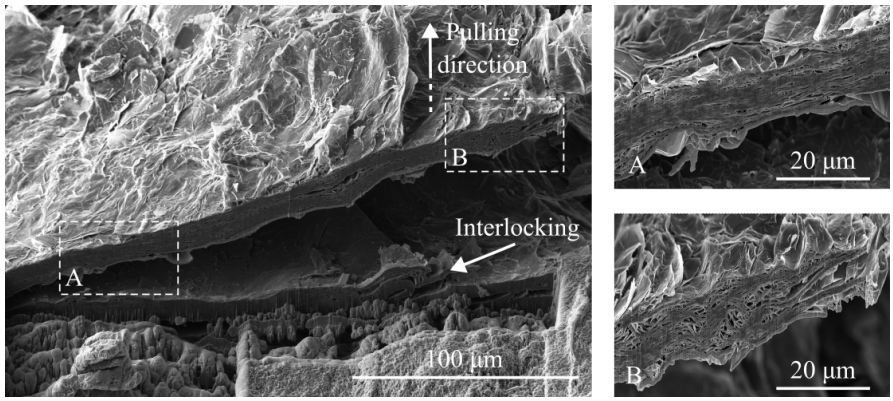

Figure 3.5: FIB-SEM investigation of a particle detached from the specimen top surface. The magnification views shows aligned and misaligned regions in the inner microstructure.

surface looked like the one in figure 3.5. It may not be possible to indicate with certainty whether the whole particle or part of it could be detached, but the thickness size thereof is coherent with those expected for compressed particles. Many micro-sheets were teared apart and fractured in the out-of-plane direction, which corresponded with the pulling direction of the tape. A small part of the particle detached appear as still being attached to the bottom surface and constitutes as an example of how the particle interlocks among each other. However, once they are compacted together, it is nearly impossible to distinguish them since the inner and outer (in between the particles) porosity show the same level of inhomogeneity. Both aligned and misaligned regions are clearly visible in the inner particle structure and especially in the inset B of figure 3.5, the micro-sheets configura-

tion appears as the result of meso-structure kinking due to in-plane compression stress. In this case, the misaligned regions are originated in between two kinking micro-sheets bundles.

3.3 Computed tomography

In X-ray computed tomography (XCT), several projections in multiple angles allows the 3D representation of an object to be reconstructed with several microns spatial resolution. This testing method was performed in the attempt of obtain a digital 3D reconstruction of Sigraflex® microstructure that could give more information about the porosity and be complementary for the 2D FIB-SEM analisys reported in section 3.2.
The XCT machine employed and the related configuration parameters are reported in figure 3.6. The specimens were stripe-shaped at the smallest size possible by means of waterjet first, and hand cutter later. This was done to avoid delamination, most likely to occur under highly pressurized water. In figure 3.7 four cross sections of the sample along the z directions can be observed. To visualize the sample more accurately, a 3D stack of images was reconstructed by images captured at different depths in both x and y direction. The 3D reconstructed volume is presented in figure 3.8. A few clusters of highly attenuating particles were also found in the internal volume (not shown here), probably due to locally denser carbon regions.
Unfortunately, despite the long-time exposure, the resolution was not sufficient to obtain detailed imaging of the microstructure and get noteworthy features reusable for further purposes.

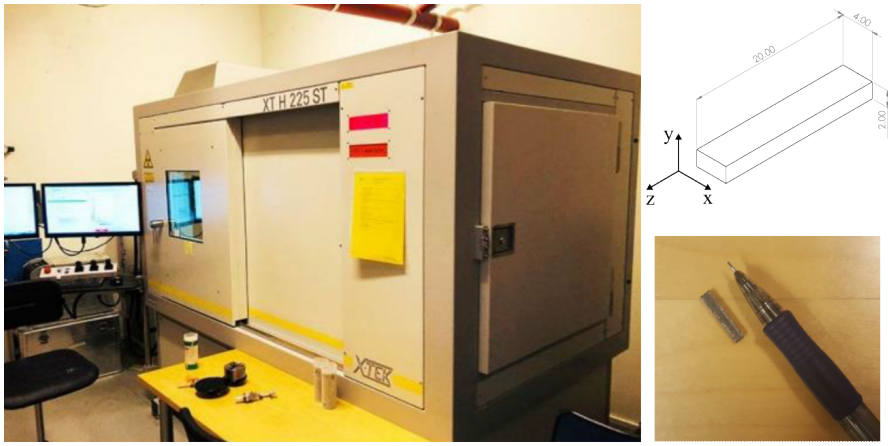

Tube voltage [kV]	Current [µA]	Voxels' size [µm]	Exposure time [h]	Projections
120	58	2.48	14	3142

Figure 3.6: XCT machine and geometry of the specimen investigated. Measures are given in mm.

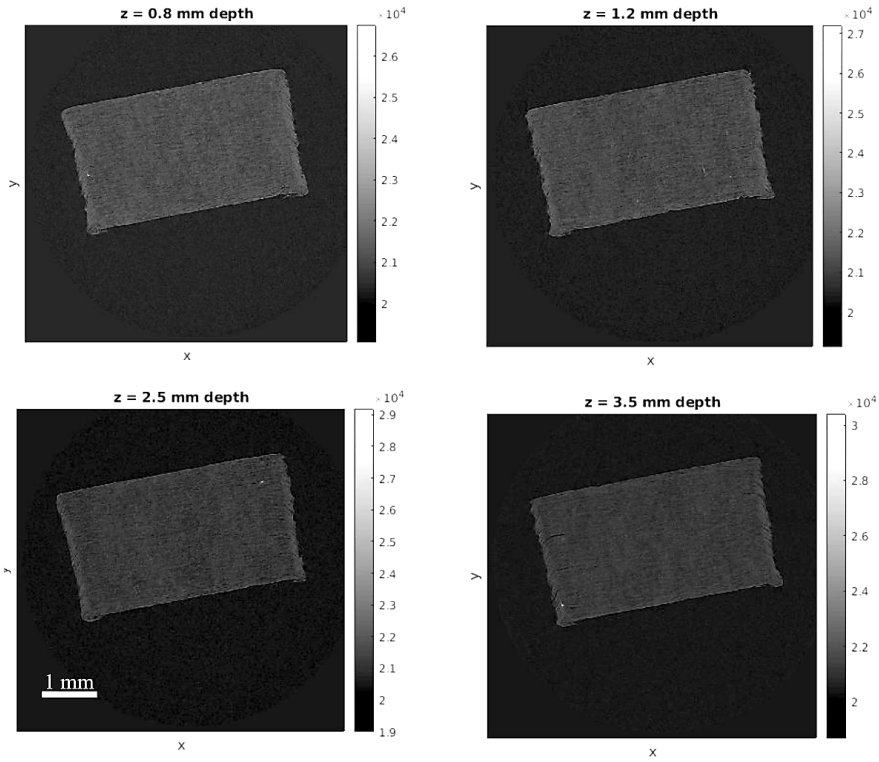

Figure 3.7: Four images extract from XCT analysis along the z-axis of the specimen.

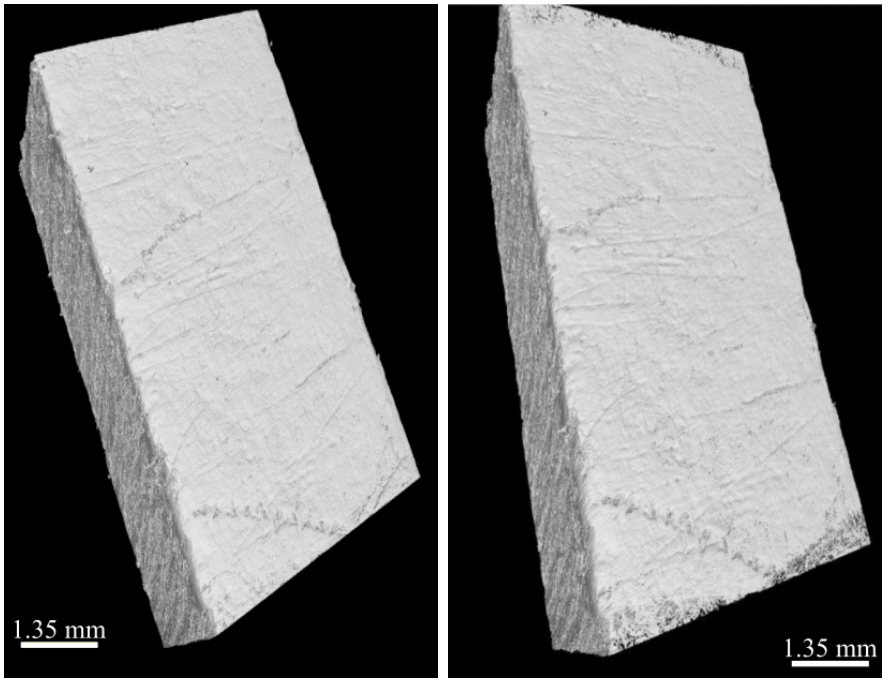

(a) **(b)**

Figure 3.8: (a) and (b): two FG specimens volume as reconstructed from stack of x, y and z images.

3.4 Static uniaxial in-plane tensile tests

3.4.1 Motivation

This section reports the in-plane tensile tests performed on Sigraflex® . The goal was to observe and analyze the stress-strain curves so to extract the main mechanical parameters and find an analytical description suitable for modeling purposes.

3.4.2 Methods

The procedure to obtain dog-bone specimens was challenging due to the material softness and ease to delaminate. After several trial-and-error iterations, the preferred method was based on waterjet cutting by means of a CNC machine i.e., WJS NCH 30, with the following parameters: jet pressure = 3800 bar, beam diameter = 0.3 mm, sand GRIT = 230.
After the cutting, the specimens were let to dry for 24+ hours at room temperature and spray-painted for Digital Image Correlation (DIC) pattern. The final geometry and its dimensions are shown in figure 3.9. In-plane tensile static tests

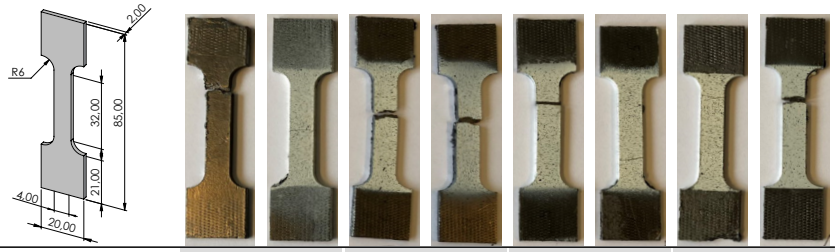

Test id.	1	2	3	4	5	6	7	8
Displacement rate [mm/s]	0.01		0.1		1		10	
Strain rate [s^{-1}]	$3.125 \cdot 10^{-4}$		$3.125 \cdot 10^{-3}$		$3.125 \cdot 10^{-2}$		$3.125 \cdot 10^{-1}$	

Figure 3.9: Post-mortem tensile specimens. Specimen sizes are shown on the top left, the dimensions are given in *mm*.

were performed in a MTS Exceed® Universal testing machine (5 kN). Eight specimens were tested upon four different displacement rates from 0.01 to 10 mm/s (figure 3.9). The front and side views were recorded at the same time to capture the deformation field on both specimen sides. The strain was calculated in two different gauge lengths as shown in figure 3.10a: the full gauge length, corresponding to commonly used gauge length, and the short gauge length, arbitrarily defined per each case between the upper and lower bounds of the fracture surrounding volume. The engineering stress and engineering strain were obtained by definitions as

$$\sigma = \frac{F}{A_0} \quad \text{and} \quad \varepsilon = \frac{u - u_0}{l_g}$$

where F is the force recorded by the machine expressed in kN, A_0 the initial cross-sectional area of the gauge length, u is the displacement array recorded by the machine, $u_0 = u(1)$ (according to MATLAB® convention) and l_g is the gauge length.

3.4.3 Results and discussion

The static curves are plotted in figure 3.10. DIC data for test 1 were not usable due to technical reasons whereas for specimens 7 and 8 the camera sampling rate was not sufficient to capture the strain fields. In figures 3.10b-c-d some combinations

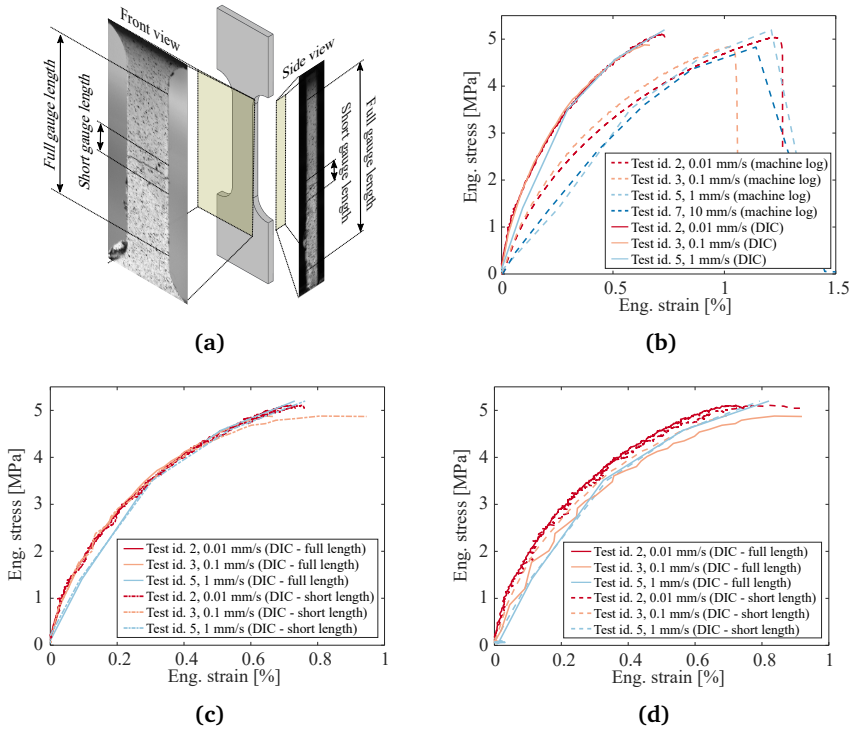

Figure 3.10: (a) DIC specimen views and gauge length definitions. Three plots are shown according to different DIC views and comparison with machine crosshead displacement data: in (b) ε was calculated by both machine displacement and DIC front view (full gauge length), in (c) ε was calculated from DIC front view including full and short gauge length, and in (d) from DIC side view including full and short gauge length.

of static curves are compared upon different views and gauge lengths. The failures appeared as brittle together with obvious delamination of the layered structure probably occurring between the compressed particles. In some cases, the DIC front camera could not detect the initial crack location because of this growing internally, while evidences of delamination were shown either in the side or back

views. The static curves plotted with the different displacements monitored from the front and side views were indistinguishable as well as the strains calculated from the full and short gauge lengths (figure 3.10c and d). The latter observations implies negligible deformation gradient along the longitudinal direction.
The non-linear stress-strain behavior resulted quite similar to that of polycrystalline graphite (see e.g. [52]). This was modeled in [44] by a simple power-law of the type:

$$\varepsilon = A\sigma + B\sigma^2 \tag{3.1}$$

where A [MPa^{-1}] and B [MPa^{-2}] were regarded as material elastic and plastic compliances. Although proposed for compression loading, in [26] such relation was adapted for the FG in-plane tensile static curves and it was found to fit pretty well the stress-strain curves up to a half of maximum stress. In the same way, A and B were obtained in this work by means of non-linear least square regression of experimental DIC data of tests 2 and 3 from the front and side views, as shown in in figure 3.11a.
In the latter figure, the data points were gathered together in the same plot while the fitting resulted from a final average of fitting parameters obtained by fitting each curve separately.
First, the data were converted to true quantities by the usual conventions (although negligible differences in the results there exist with respect to engineering quantities):

$$\varepsilon_{true} = \ln\left(1 + \varepsilon_{eng}\right)$$
$$\sigma_{true} = \sigma(1 + \varepsilon_{eng})$$

Then, an initial fitting was done by means of a high-degree polynomial (degree ≥ 2) so to obtain a smooth series of data, and its derivative was evaluated at the origin so to get the best approximation for the initial elastic modulus. This was found to be 2288.94 ± 0.266 MPa.
A second fitting was done by means of equation 3.1: in one case, A was imposed as equal to the initial tangent slope found earlier while on another case this was left as a fitting parameter. In the latter case the values of A found were compared to the values of the derivative evaluated at the origin (3.11b). The stress domain on which the fitting was executed was varied until the best coefficient of determination R^2 was obtained ($R^2 > 0.998$). This occurred around 60 - 70% of the maximum stress as shown by the end of continuous line in figure 3.11a; here the curve is also compared with the fitting obtained by using the whole stress domain. This tends to overestimate the tangent at the origin (see figure 3.11b) while it best describes the curve shape at larger strains. The mean values of A and B at the optimal R^2 are 0.3488 ± 0.106 GPa^{-1} and 130.78 ± 44.93 GPa^{-2}, while the mean values in the whole stress domain are 0.0384 ± 0.032 GPa^{-1} and 256.97 ± 14.73 GPa^{-2}. The latter pair of values compare well with the quantities reported by Dowell and Howard [26]: $A = 0.437$ GPa^{-1} and $B = 392$ GPa^{-2}.
The ultimate tensile strength was taken as the maximum stress, also corresponding to the maximum strain, reached by the curve and it is reported in figure 3.11c.

The average value obtained is 4.984 ± 0.181 MPa in full agreement with values from literature (see [22] for a review).
Finally, the true strain at break is reported in figure 3.11d: the mean value obtained from machine log data are higher that DIC data. The latter are quite similar in both the front and side views. None of elastic modulus, maximum stress and maximum strain show rate-dependency in the range 0.01 - 10 mm/s.

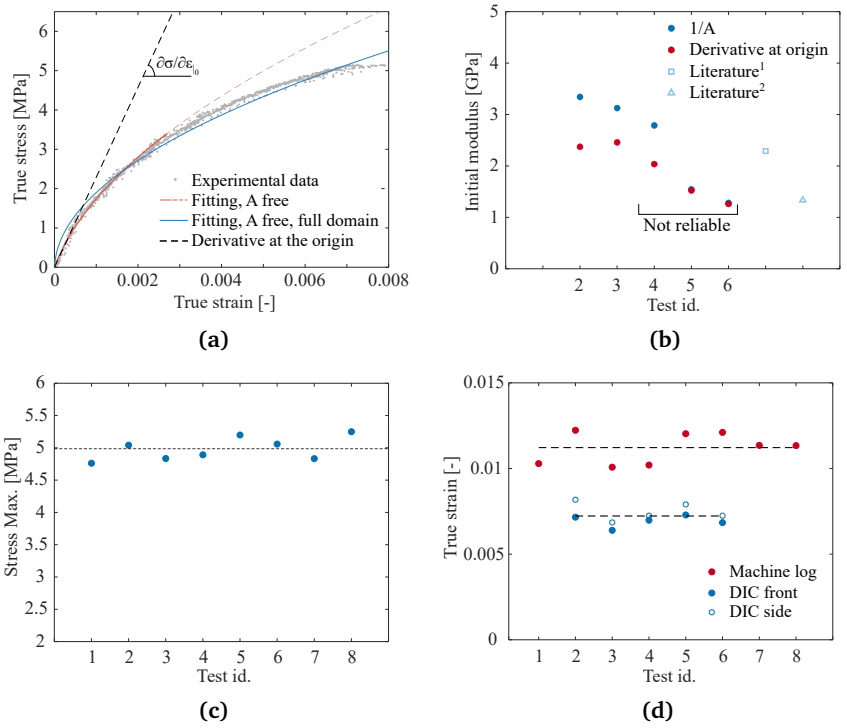

Figure 3.11: (a) Fitting of experimental data according to Jenkins [44] at different maximum stress. The derivative at the origin is evaluated from a different fitting that employed a high-degree polynomial. (b) Inverse of A and derivative at the origin compared with values found in literature [26][1] and [45][2]. (c) Tensile strength obtained as the maximum stress of the curve. The dashed line indicates the mean value: 4.984 ± 0.181 MPa (d) Tensile true strain at maximum stress, also corresponding to the strain at failure. The dashed lines indicate the mean values: 1.12 ± 0.090 % (from machine log) and 0.72 ± 0.052 % (from DIC).

3.5 Static uniaxial in-situ tensile tests

3.5.1 Motivation

This section reports the in-plane tensile tests performed in-situ on Sigraflex® . The specimens tested were markedly smaller than those used in the previous section, the environment was controlled the fracture could be observed by SEM while propagating. The goal was to observe the differences with the macro-scale tests and the effect of different environments.

3.5.2 Methods

Small specimens were cut by the same technique described in section 3.4.2. The dimensions and geometry are reported in figure 3.12 together with the test matrix that summarizes all the testing conditions. The testing equipment consisted in a

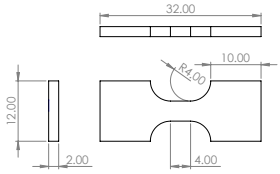

(a)

Test id.	Strain rate (µm/s)	Environment
1	2	Air
2	2	Air
3	-	-
4	0.2	Low vacuum
5	0.2	Low vacuum
6	0.2	High vacuum
7	0.2	Low vacuum
8	20	High vacuum
9	20	Low vacuum
10	0.2	High vacuum

(b)

Figure 3.12: (a) In-situ tensile dog-bone specimens, including dimensions in *mm*, and (b) test matrix

SEM with an embodied Kammrath & Weiss tensile/compression module with 5 kN load cell[2]. Two first trial tests were performed in air at 2 µm/s to calibrate the set-up procedure and check the load cell capabilities. Then, seven more different specimens were tested in inert atmosphere (N_2) and both in low and high vacuum $\simeq 10^2$ and $\simeq 10^{-3}$ Pa, respectively.
After each specimen setup, a waiting time of at least 20 minutes was given to allow the vacuum conditions to stabilize inside the chamber. In test number 10, the waiting time was extended up to 40 minutes to further ensure that the complete outgassing. All tThe specimens were tested at two different displacement rates i.e., 0.2 and 20 µm/s, corresponding to $5{\cdot}10^{-5}$ and $5{\cdot}10^{-3}$ s^{-1} nominal strain-rates and also to the upper and lower limits achievable with the available equipment.

[2] www.kammrath-weiss.com/en/tensile-compression-module

3.5.3 Results and discussion

A sequence of four frames captured during a single test is reported in figures 3.13a-d. Each test shows similar characteristics of the propagating crack: this started from a defect sometimes visible on the surface, and propagated in a brittle manner along the cross-section with no obvious striction of the lateral sides. Similarly to what was discussed in section 3.4.3, the original defect may also lay on the sides of the specimen that were not imaged, and the propagation lines visible on the top surface may be an advanced stage of cracking. The crack runs around the particles that appear to maintain their integrity while they are being pulled apart, rotated and detached. Some of them can be easily recognized along the fracture profile in figure 3.13d, but a further insight will be given in section 3.5.4.

All the engineering stress-strain curves are reported in figure 3.14a. The curves

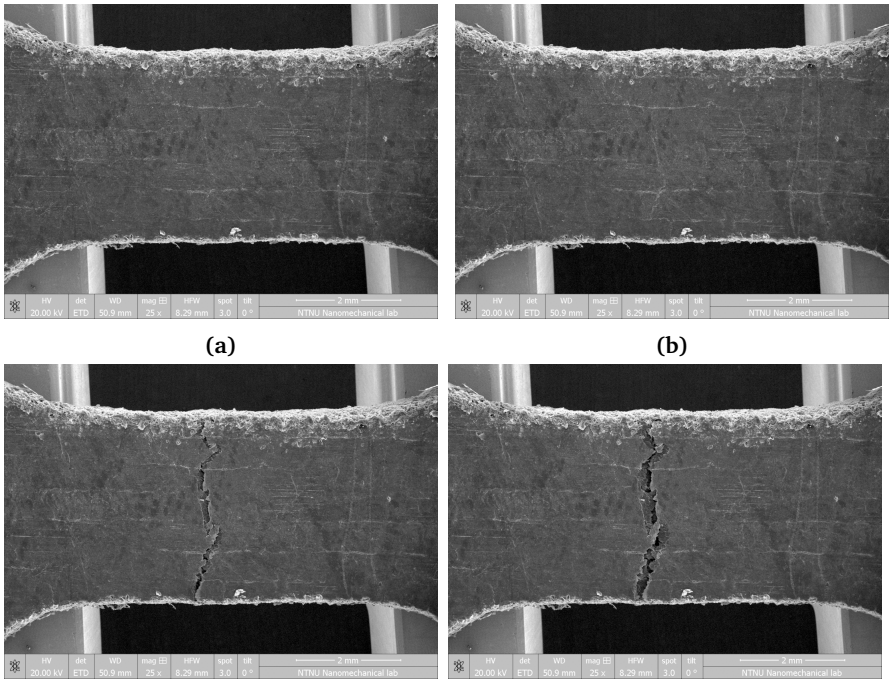

Figure 3.13: Frames sequence of test 4: (a) undamaged specimen, (b) and (c) the crack grows and propagates, and (d) the specimen is completely fractured.

appear uniformly scattered and no clear effect can be observed from strain-rate variations in the tested range or in different pressure conditions. The stress-strain relationship appears non-linear with downward concavity from the early beginning of the deformation, in line with the macro-scale tests. Although the crack can develop either in the central cross-section or more towards the grips, the stress-

strain trend is not much influenced. Interestingly, the decrease in stiffness near the maximum appears smoother than in the macro-scale testing, either ascribed to a lower rate sensitivity or to a scale effect. The maximum strength is taken as the maximum point of the stress curves and resulted 4.348 ± 0.332 MPa. This compares well with the one recorded in macro-scale tests. Same for the strain at maximum stress calculated from the machine log that is 0.968 ± 0.086 % (see figure 3.14b).
All the curves fall within the same scatter of data and nothing can be said about the effect of each environment on the stress-strain curves.

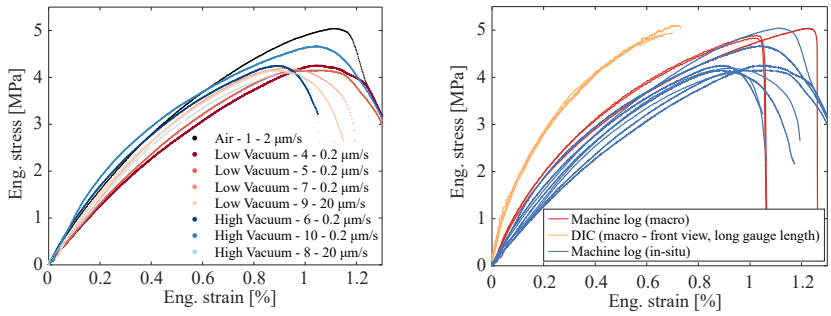

(a) **(b)**

Figure 3.14: All the stress vs strain curves are reported in (e) except for test 2 and 3 which were discarded due to bad sampling. These are compared with stress vs strain curves (Test 2, 3 and 4) from macro-scale tensile tests in (f), both from machine log and DIC recording.

3.5.4 Post-mortem fractography study

After the complete failure, the fractured surfaces of the specimens corresponding to test 3,4 and 5 were observed by SEM. Examples of top and front views are shown in figure 3.15. In the front view, the white creases laying horizontally correspond to the particles and micro-sheets bundles that have been compressed from above during the compaction process. The fractured cross-sections is not flat and indeed clear vacancies of the particles pulled apart have left are obvious. The effect is similar to delamination of fiber in fiber reinforced composites.
Some particles not completely detached can be observed here and there, as a confirmation that some degrees of integrity is maintained during the compaction and during the tensile test. In figure 3.13d, the fracture shows smooth edges that seem to follow the boundaries of the compacted particles. Getting closer in the magnified view A of figure 3.15, traces of tearing and ripping off are clearly visible and sometimes patches of particles appeared still stuck to what were the neighboring particles before the rupture. The micro-sheets can create complex patterns at micro-scale as the ones shown in the magnified views of figure 3.15: their extreme

flexibility originated from inherent carbon basal planes property and the internal structure of each single particle is expected to be a compacted network of folds and creases. In the magnification D of the same figure, the surface of the micro-sheets is extremely corrugated and looks like a ripped off cloth after breakage. Among the SEM pictures available in literature, these and the similar ones reported in [17] were the most detailed to get a close-up of FG microstructure before the FIB-SEM application reporeted in section 3.2.
Upon careful observation of each test fracture surface, the type of fractures were found to be slightly correlated to the testing rate. Borrowing the glossary from metals, we can consider the particles as grains and define *transgranular* the local fractures occurring across the grain and *intergranular* those occurring at the boundaries. The latter were found mostly at lower strain rates whereas transgranular fractures were observed to be consistent at higher strain-rates. In this condition the material tended to show brittleness and transgranular fractures probably because of shorter time available to rotate and re-arrange so to redistribute the stress along the boundaries.

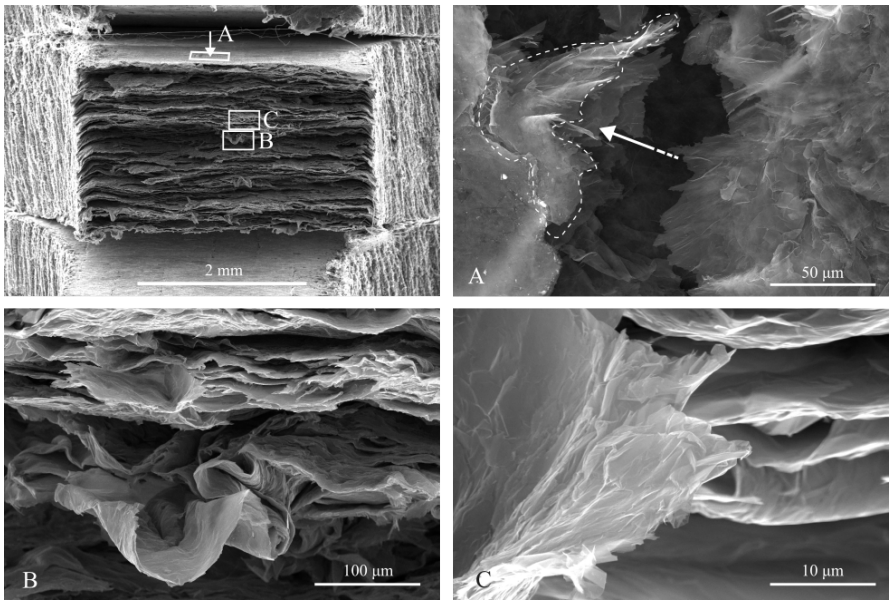

Figure 3.15: Post-mortem cross-section of in-situ tensile tested specimens. Magnified views A, B and C highlight the tearing mechanism at the origin of particle detaching, the micro-sheet complex patterns due to particles interaction during the compaction process and the corrugated surface of a single micro-sheet.

3.6 Uniaxial compression

3.6.1 Motivation

This section reports the out-of-plane compression tests performed on Sigraflex® . The goal was to extract the main mechanical parameters such as the elastic modulus or the yield strength, and to assess whether Sigraflex® showed similarities with stress-strain curves of other well-known materials. Although some data were already available in literature [46], these were taken up to a maximum stress of 1 MPa. Here, the tests will be pushed further above, the unloading and cyclic behavior will be analyzed as well as the stiffening due to densification.

3.6.2 Methods

Static and cyclic uniaxial compression tests were carried out by using the same material described on section 3.1. The foils were hole punched in circular specimens with 26 mm nominal diameter (figure 3.16a) and an Instron Electropuls® E10000 machine used for testing (maximum load ±10 kN, load cell resolution ±0.5 N) was equipped with compression plates as in figure 3.16c.
In total, 25 tests were performed on single unit specimens (figure 3.16b) and

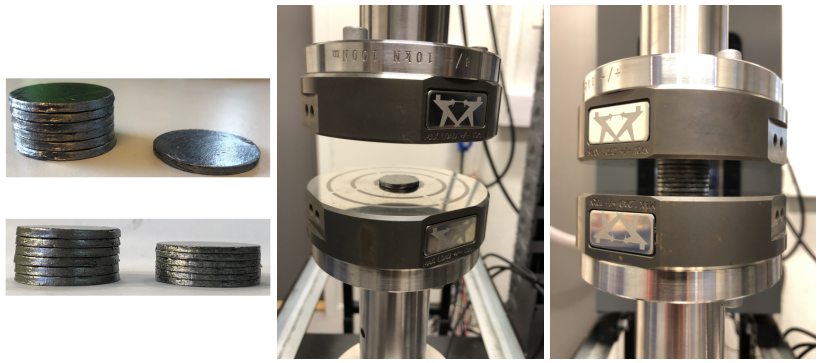

(a) **(b)** **(c)**

Figure 3.16: (a) Single sheet and stacked specimens' geometry and stack specimen residual deformation (top and bottom, respectively). Testing example of single sheet (b) and stacked (c) specimens.

5 tests on 6-units stacked configuration (figure 3.16c). The number of specimen per each testing condition is reported in Table 3.3. Recommendations from ASTM D695 [87] and ISO 13314 [88] were followed when possible. All the monotonic and cyclic displacements were applied at 0.1 mm/min rate by means of single or repeated triangular waveforms where, in some cases, a 30 seconds holding time was applied at the maxima and minima displacement peaks. A pre-load not exceeding 0.03 MPa (∼15 N) was consistently imposed for all tests to ensure contact

between the plates and the specimen. The monotonic tests were stopped at arbitrary displacements and unloaded completely before any sign of failure could be detected.
In 7 cyclic tests, a cyclic load up to 1 MPa with a load rate of 30-40 kPa/s was imposed prior to testing for 6-10 cycles, until a satisfactory repeatability was observed in the loading-unloading curves, and the test program followed as regular in displacement control. One test was done at 0.01 mm/min and one in load control at 20 kPa/s (roughly equivalent to a displacement rate of 0.1 mm/min). In any case, the maximum stress achieved ranged from 1 to 14 MPa.
The specimens' diameters and thicknesses were measured by a digital calliper (± 0.01 mm resolution) at 5 random positions along the lateral and base surfaces before and after each test so that the residual deformations could be compared with the machine log data. The data were plotted using the definition of true strain for compression:

$$\varepsilon = \ln \frac{h_0}{h}, \tag{3.2}$$

where $h_0 = 2$ mm is the gauge length of the specimens also corresponding to the nominal thickness, and h is the current specimen thickness. The engineering and true stresses were considered as equal due to the small variation of the resistant area. These were obtained as:

$$\sigma = \frac{F}{\pi R^2}, \tag{3.3}$$

where F is the machine force and R the specimens radii.

	Monotonic	Cyclic
Single specimens	8	17
6-sheets specimens	4	1

Table 3.3: Number of tests per each case

3.6.3 Monotonic curves: description and discussion

Three examples of true stress-true strain curves are shown in figure 3.17a. All the stress-strain responses feature an initial flat toe of variable length, including those obtained from stacked specimens, and steepens up to prosecute with an apparently linear domain. The concavity is turned upward after a knee occurring always at a well-repeatable stress level between 3 and 4 MPa. Three domains were detected based on the change points of the true stress-true strain tangent modulus (figure 3.17b). In the first domain, the initial toe was characterized by a fast increase in slope where a local maximum was reached in correspondence of a stress value of 3 MPa and slope value of 30 to 40 MPa. The true strain at maximum showed a wide scatter of values around 6 – 6.2 %, spanning between 1.5% and 16%. The corresponding stress values were instead tight in the range 0.3 - 0.4 MPa. To exclude that this initial toe was due to unexpected geometrical

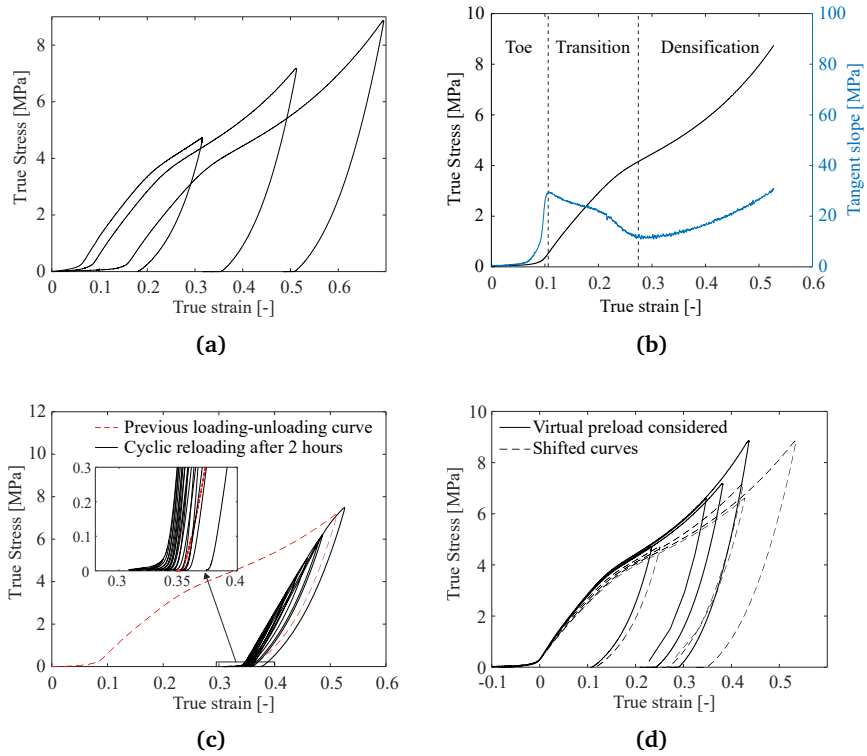

Figure 3.17: (a) Uniaxial compression curves of Sigraflex® , (b) average curve and relative tangent slope, (c) monotonic loading up to 7 MPa and subsequent cyclic reloading after full recovery and (d) comparison between curves obtained by shifting in the strain axis and curves obtained by considering zero trues stress at the virtual preload of 0.3 MPa

imperfections of the specimens, a single sheet was monotonically loaded up to 7 MPa to obtain a perfect flat specimen, let recover for 2 hours and loaded again, cyclically, up to 7 MPa (figure 3.17c). The toe was again clear, but the strain recovered was much less than the one observed in the first loading-unloading path. The same behavior was also well visible in the piled-up specimens and was considered as part of the material response in a recent investigation of similar FG stacked disks loaded up to 1 MPa [46]. However, since it contributes to a large part of the total true strain, its influence was normalized here by applying a virtual preload of 0.3 MPa to all the tests and by taking the corresponding displacement as a new zero for the true strain definition 3.2. The curves obtained in this way are plotted in figure 3.17d together with the corresponding curves obtained by taking the first recorded displacement value as reference and by shifting along the strain axis. Interestingly, the curves obtained by virtual pre-load tend to nicely overlap

meaning that the 2-mm-gauge length starts to be "effective" only at the end of the toe. It is therefore supposed that the toe strain is due to the relaxation of the material after the production process governed by meso-structural mechanisms such as micro-sheets unfolding and disentangling. Since friction is involved in the unfolding process of the micro-sheets, it is regarded to as visco-elastic mechanism that is hindered at higher compression loads by an increasing number of contacts and geometrical constrains of the micro-sheets. This can be better explained by the crumpled nature of FG, that will be detailed in depth in section 4.2.2.
It is highlighted that the curves used and the data calculated in the next sections will always refer to the curves calculated assuming the virtual preload, and hence excluding any data in the stress domain below 0.3 MPa.
The second domain of the monotonic behavior under discussion spanned up to 24% strain. Here the tangent slope decreased (and hence, the stress-strain curve is not actually linear) more slowly than in the first domain and reached its local minimum at around 12 MPa. This occurred in correspondence of the curves' knee, recognizable as the hump at the end of this domain. The stress corresponding to the slope minimum was again well repeatable for all the tests and it was 5.1 MPa on average.
In third domain, the tangent modulus grew up to the maximum load. The concavity acquired at this point by the stress-strain curve is attributed to the densification regime given by the pore closures mechanisms where the pore walls are predominantly touching with each other. Since the material itself is the result of a densification process followed by a certain amount of recovery, the third regime can be regarded as a continuation of this process, whereas the second region represents the transition needed for the specimen to catch up the inelastic deformation accumulated during the production. To trigger again the densification, the stress applied must be equal to or higher than the maximum stress undergone during the compaction: this can be estimated by the exponential fit proposed in [46], where the forming pressure is replaced with the compression stress and is related to the final density ρ_p by:

$$\sigma = 0.35e^{2.6\rho_p}. \tag{3.4}$$

When $\rho_p = 1$ g/cm^3 then $\sigma = 4.7$ MPa, similar to the average value $\sigma = 5.1$ MPa found here.

3.6.4 Cyclic curves: description and discussion

An example of cyclic curve is shown in figure 3.18a. Three main phenomena were observed in all the tests: (i) memory of subsequent cycles stress-strain extreme points, (ii) nearly-zero yield strength and (iii) large hysteresis in the unloading-reloading path.
The first one refers to the tests where 2 or more cycles were done at the same peak strain (figure 3.18a or inset in figure 3.18b): inelastic deformation is induced in the material only during the first few loading cycles that are followed by a stable regime where the strain is fully recovered at each cycle. Hysteresis

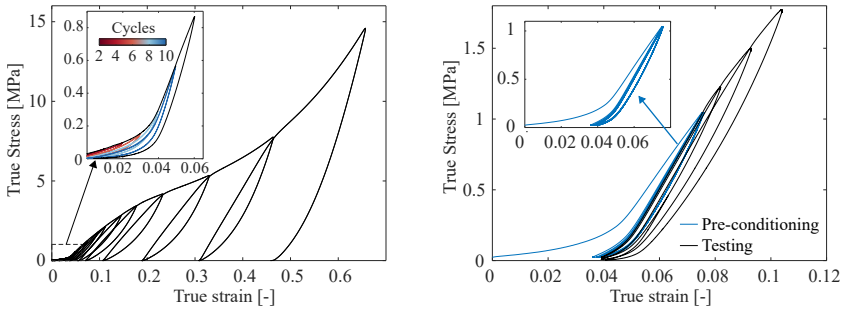

Figure 3.18: Cyclic curves: (a) example of cyclic curve, including a magnification view of the first cycles at low loads. Two cycles at the same peak strain were done up to 5% true strain, then one cycle. (b) Stabilization at 1 MPa peak stress and cyclic loading at higher peak strains. The material has almost perfect memory of stress-strain extremals from the second cycle on.

is always visible, but the stress-strain reversal points are held fixed and become memory points. The memory can be established again by exceeding the current peak stress and cycling at higher strains or loads. This behavior was reported for bulk artificial graphite [89] and can be associated to discrete memory typical of rocks and soils [90]. It was motivated by the layered structure of graphite that allows for generation of so-called incipient reversible kink bands [89].

About the nearly-zero yield strength, this is common in foams under compression due to specimen geometry imperfections, as reported in [91], but it is also well-known to occur naturally in polycrystalline graphite under uniaxial compression loads [52]. As shown in the inset of figure 3.18a, the cyclic paths usually started from a positive pre-load around 0.03 – 0.04 MPa, reached the peak stress and recovered the total strain imposed. When the peak load overcame 0.5 MPa, a permanent strain at zero load appeared at the end of the unloading. However, for any peak stress, also lower than 0.5 MPa, the stress values at zero strain tended to decrease as if the preload was already inside the plastic domain and the yield strength lower than the pre-load.

An alternative explanation to this phenomenon may be the viscous behavior of the material. It is not excluded that holding a longer waiting time at zero load may have allowed for the full recovery of cycles having peak stresses even higher than 0.5 MPa. However, the same behavior was also observed in the 0.01 mm/min test, the slowest one.

Concerning the large hysteresis, this is typical in foams made of polymeric materials [91] due to the visco-elastic character of polymer chains. Analogously, the viscous character of FG (already highlighted in [32]) may be inherited by the layered crystal structure of graphite that allow for basal dislocations and kink

bands to propagate and exhibit recoverable hysteresis loops [89].
Thus, on one side, the contribution from the graphite crystalline structure to the FG hysteresis would be given by the aligned regions that may constitute a large part of the total volume (in the FIB-SEM section, a fraction equal to 0.49 of the area investigated was attributed to aligned regions). On the other side, the misaligned micro-sheets can also contribute to the viscous behavior in different ways, as for example fibres in entangled materials where geometrically constrained features slide and originate friction forces [92]. Further testing is needed to uncouple these two potential contributions, but it is believed that the second one is limited to the toe region at low loads since that can be related to the structural component of the total strain (further discussion will be given in section 4.2).
As final remark, it is reported that those tests that were pre-conditioned did not show any remarkable difference with the other ones. The cyclic paths stabilized after 2 - 6 cycles as in figure 3.18b while the toe was always visible in the low-loads domain together with a constant are inside the cycles. Further re-cycling at higher or lower loads than 1 MPa did not show again any difference with other not pre-conditioned tests. In each test, the toe contribution was visible only in the low-loads region of every cycle and tends to gradually become shorter at increasing loads until almost disappearing above 40% true strain and 7 MPa true stress.

3.6.5 Observations on the initial cyclic tangent slope

The initial tangent modulus of the loading paths was calculated to monitor the change in stiffness under increasing compression loads. A part of the irreversible deformation obtained by new compaction is given both by micro-sheets' folding and additional interlocking. These affect the pore shapes and sizes, and consequently the elastic response for which the initial tangent modulus is considered as representative.
Due to the hysteresis loops shape, the modulus was calculated as shown in figure 3.19a: per each cycle, the initial part of the loading path was fitted by a linear polynomial in the part where the toe was considered as fully expired, usually corresponding to 0.3 – 0.4 MPa. The slope of the fitting was taken as the tangent modulus.
The tangent line was then extended downward to cross the x-axis and the intersected true strain ε_p was considered as the inelastic component of the total strain. This was used to define to final relative density ρ_p^* by means of

$$\rho_p^* = \frac{\rho_0}{\rho_s} e^{\varepsilon_p} \tag{3.5}$$

where $\rho_0 = 1$ g/cm^3, ρ_s= 2.26 g/cm^3 and no lateral deformation is assumed. The last hypothesis will be better supported in section 3.6.6. The moduli are finally plotted against ρ_p^* in figure 3.19b.
The initial cyclic tangent modulus in general differs from the cyclic secant mod-

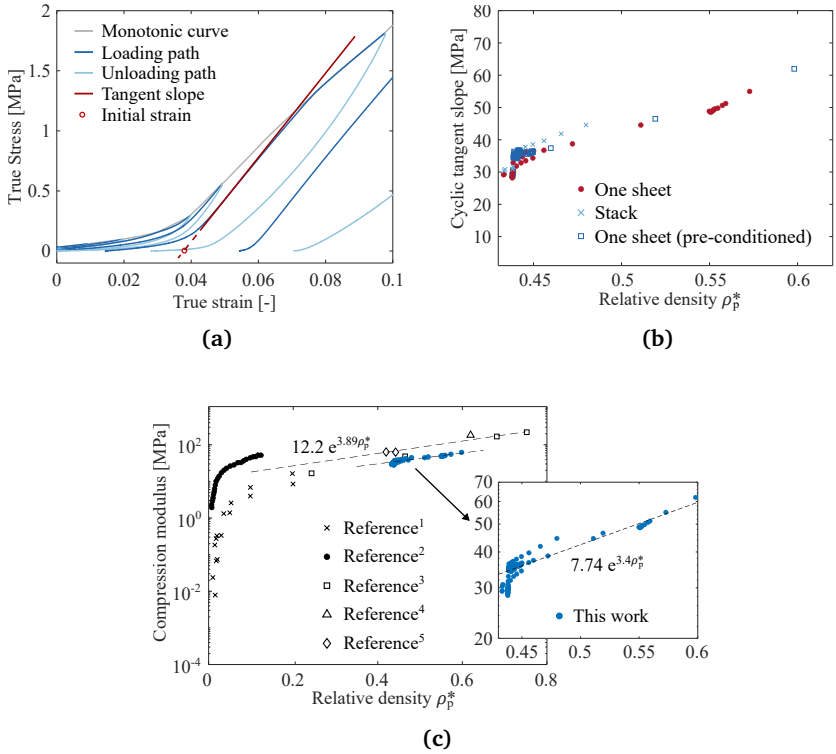

Figure 3.19: (a) Calculation of the tangent slope in the initial part of loading cycles. This is taken as the slope of the true stress-true strain loading path as soon as the toe is ended. The initial strain is found by the tangent line intersection with the x-axis. The cycles not reaching at least 0.5 MPa peak stress were not included in the calculation. (b) Tangent slope plotted against the relative density. The latter was obtained from the true strain by the assumption of no lateral deformation. (c) Tangent slope and compression moduli from literature plotted against the relative density: [1][93], [2][20], [3][46], [4][94], [5][33]. Only data points at $\rho_p^* > 0.1$ were considered in the linear fit.

uli used to characterize foams of various nature (see for example [91]), but it is considered here as more meaningful because of the different production process employed for FG. The uniaxial compression test can indeed be regarded as a continuation of such process, and each unloading as the final stage for obtaining a new FG sheet with different properties such as density and tangent modulus.
In [91], it was observed that the cyclic secant modulus in metal, polymer and cement foams varies differently in the elastic, plastic and densification domains. In the case of Sigraflex® instead, the tangent modulus was found to solely increase from an initial value between 30 to 40 MPa up to 60 MPa when the relative density

was increased from 0.44 to 0.6. The material hence undergoes stiffening from the beginning of compaction, or equivalently, continues the crumpling process from where it was left after production.
In light of equation 3.4 and of the exponential law $E_d = E_{d,0}\, e^{-bP}$ proposed earlier in [33] to relate the compression moduli E_d and the porosity P where $P = 1-\rho_p^*$, the cyclic tangent moduli were plotted in semi-logarithmic coordinates together with the data available in literature (figure 3.19c).
The exponential fit in the inset of figure 3.19c was found to describe nicely the moduli evolution along with ρ_p^* and gave an exponential coefficient of 3.4, quite different though from 0.2 found in [33]. Likewise, the data found in literature were fitted in the same figure to a similar exponential laws, including the average value for the initial tangent modulus found in this work (34.35 MPa). They gave a similar exponential coefficient equal to 3.89, supporting the argument that the application of further compression may be also seen as a continuation of the production process.
Even if the specimens were produced under different conditions (closed die or rolling) and different were the measurement technique (ultrasound speed or stress-strain tangent slope), it is clear that the FG tangent modulus H follow a scaling law of the type

$$H = H_0\, e^{n\rho_p^*} = 7.74e^{3.4\rho_p^*}, \tag{3.6}$$

when in the range 0.1 – 0.2 g/cm^3 $\leq \rho_p^* \leq$ 0.7 - 0.8 g/cm^3. Here, H_0 is the FG tangent modulus at $\rho = \rho_0$ and n is the exponential coefficient.
Similarly, also equation 3.4, can be expressed in terms of the final relative density ρ_p^* by setting $\rho_p = \rho_p^*\, \rho_s$,

$$\sigma = 0.35\, e^{5.88\rho_p^*}. \tag{3.7}$$

The relations 3.6 and 3.7 highlight the main differences between FG and cellular solids, that mainly follow power law-like scaling relations [95].

3.6.6 Measurement of the residual deformation

Despite Sigraflex® datasheet indicates 0.1 coefficient of friction for general contact with steel, very low barrelling and lateral deformation were visible in the piled-up specimens during the tests up to 30% longitudinal compression strain. The same was reported by Cermak et al. [46]. For these reasons, the volumetric strain will be taken as equal to the axial strain for both single and piled-up specimens, so that equation 3.5 holds. This assumption is not completely true, since, as it will be shown in this section, a small amount of residual lateral deformation is visible at the end of each test and is supposed to exist also during the compression. However, it will be considered accurate enough for the transformation of axial strain into volumetric strain until more accurate measurements will be performed in future works.
The residual volume change was assessed by measuring the residual axial and radial deformations at the end of each test. In figure 3.20a, the measurements of

the thicknesses and radii of each specimen are shown against the maximum true strain; in the case of axial residual strain the corresponding machine data for the last displacement value at zero load is also shown to assess potential influence of additional strain due to long-time relaxation. The minimum displacement resolution caught by the calliper was ± 0.01 mm: this was fine enough to exclude the influence of a systematic error, but not to resolute the size variations of specimens loaded below 0.08 true strain. The radial residual strains shown in figure 3.20a

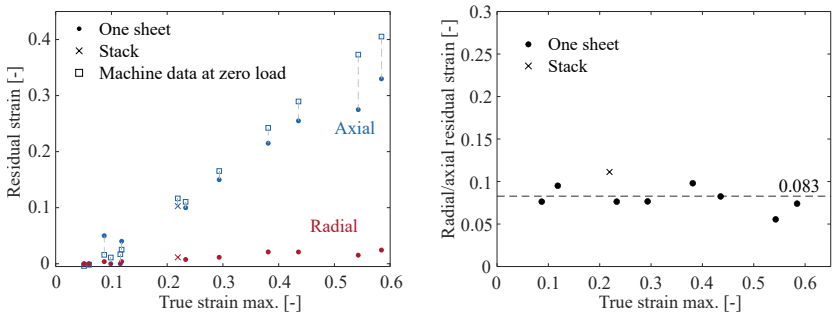

Figure 3.20: (a) Radial and axial residual strains, and (b) radial/axial residual strain ratio. The measures of the sample thickness were taken by a digital calliper at least 30 minutes after each test and compared with the machine displacement in (b). The latter represents the values of the thickness right after the test end and the dashes lines represent the waiting time before each measurement (≥ 30 minutes).

rose above the calliper resolution at around 0.1 true strain (corresponding to 3 MPa) and increased almost linearly with the applied deformation. Same for the axial residual strain that showed good agreement with the last strain recorded by the machine at the end of the unloading path. Long-time relaxation was probably more effective at strains higher than 0.5 where more gap is visible between the calliper and machine data.

These measurements were meant to quantify the recovered deformation of the initial toe after sufficient relaxation time, but this was not detected probably because of the too high pressure applied manually by the calliper. The ratio between the residual strains in the radial and axial directions can be considered as an estimation of the plastic Poisson's ratio of the material, even though more accurate strain-recording method should be applied to verify the quality of these data. The plastic Poisson's ratio is typically very low for most foam materials ranging around 0.04 [95]. The elastic Poisson's ratio for non commercial FG was observed in the single particle deformation under compression and it was estimated to be 0.04 in [18]. This is not so different from the average value of 0.083 shown in figure 3.20b and can be considered as constant through the whole tested domain, that

is, up to ≃0.58 true strain.

3.7 Nanoindentation

3.7.1 Motivation

Nanoindentation is a useful technique for measuring the mechanical properties of materials at the micro and nano scales. In this section, the nanoindentation testing of Sigraflex® is presented: the primary goal is to observe the load-displacement response and extract the modulus of elasticity and hardness. These will be compared to the corresponding macroscale mechanical properties.
Although this technique is widely and successfully used to find the modulus of elasticity and hardness of several materials, the scalability of this parameters is not trivial when a porous and anisotropic material such as FG is investigated. Indeed, as mentioned in chapter 2, only two studies have been published about nanoindentation on similar FG, and only one of them concerns FG with 1 g/cm^3 [50]. In the latter, an average value of 190 MPa for the modulus of elasticity was extracted from nanoindentation unloading curves, a value much higher than those found in this work (30 to 40 MPa) and those reported by Cermak et al. [46] (around 50 MPa) in the static uniaxial compression tests.
This discrepancy may be ascribed to either local variations of density, (Bonnissel et al. [60] indeed predicted a density gradient from the sheet midline to the surface due to the compaction process) or to the anisotropy of the microstructure. Despite the FIB-SEM analysis has clarified how the microstructure appears, it still remains a local analysis that cannot guarantee whether or not the observations done on an area of 100 × 150 µm^2 with porosity $P = 0.15$ is representative of the bulk material. In figure 3.21, a real-size indenter drawing has been placed on top of the mentioned SEM image obtained in section 3.2.3. From this picture, it is first

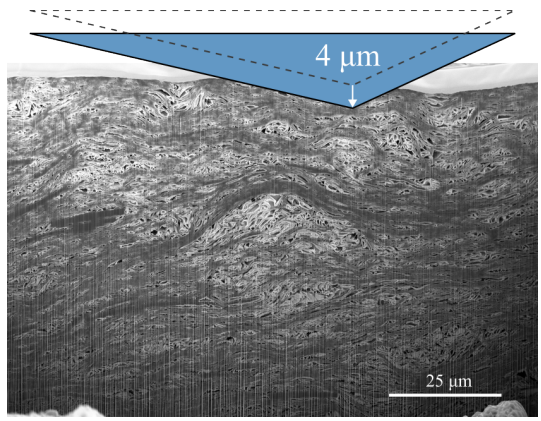

Figure 3.21: Schematic representation of a real-size Berkovich tip placed on top of the FIB-SEM cross-section investigated in section 3.2.

noticed that the surface roughness[3] can be neglected compared to the maximum indentation depth (4 µm in this case).
An indentation can affect a large volume of material underneath the tip, down to tens of times of the maximum indentation depth, but the exact dimension is not easy to estimate a priori being also material dependent. Therefore, the properties extracted from this nanoindentation study may potentially be representative of a FG volume equal or smaller to that investigated in the FIB-SEM analysis, but this should be checked a posteriori by means of, for example, the direct comparison of the extracted mechanical properties with the mechanical properties obtained in macro-scale tests.

3.7.2 Methods

Instrumented nano-indentation testing was performed by a Hysitron TI950 Triboindenter equipped with a Berkovich tip (figure 3.22a) on a small squared sample ($\sim$10 x 10 mm^2) that was cut out of a bigger sheet by means of a cutter. The tip is described in the indenter manual as a three-sided pyramidal probe with total included angle from one edge to the opposite side of 142.35°. The half angle from the perpendicular to one face is $\alpha = 65.35°$. For the sake of accuracy, it is underlined that in some reference such as [96], this angle is given as 65.27° and may lead some differences when comparing data at very small indentation depths. See the inset in figure 3.22a for a complete geometry overview.
The static nanoindentation consisted on a single loading - unloading cycle, separated by a short holding time (0.5 s) at fixed maximum load (see figure 3.22b). The holding time was included so to uncouple the unloading behavior from any viscous effect. The loading and unloading ramps were conducted at constant and symmetric loading rates: 1000 - 2000 - 3000 - 4000 µN/s, and the maximum stress was kept at 1000 - 2000 - 3000 - 4000 µN. A matrix of 10×10 indentations per load rate was performed on the top surface of the sample in the out-of-plane direction, each spaced by 10 µm in the in-plane directions.
According to the indenter manual, the tip radius is usually finite and given as 150 nm in a brand new tool. As it will be shown in section 4.12, the tip radius is fundamental to model correctly the material response in the low load region. However, this is expected to naturally wear out after several uses and for a better accuracy, it is usually either measured a posteriori by means of e.g. AFM microscope or calculated by Hertzian fitting of the low-loads region in the loading path. In this case, direct measurements of the tip were not available, and the radius was estimated by means of Hertzian contact fitting in a previous work that employed the same tip [97]. This was found to be 1 µm.
The reduced modulus E_r as well as the hardness H are extracted from the load P

[3] In the Sigraflex® datasheet, it is reported a value of 10 µm for the surface roughness. It is however unclear whether it concerns the peak-valley roughness or any derived quantity. The datasheet can be found here: `https://www.sglcarbon.com/en/loesungen/material-downloads/downloads-sigraflexr/`

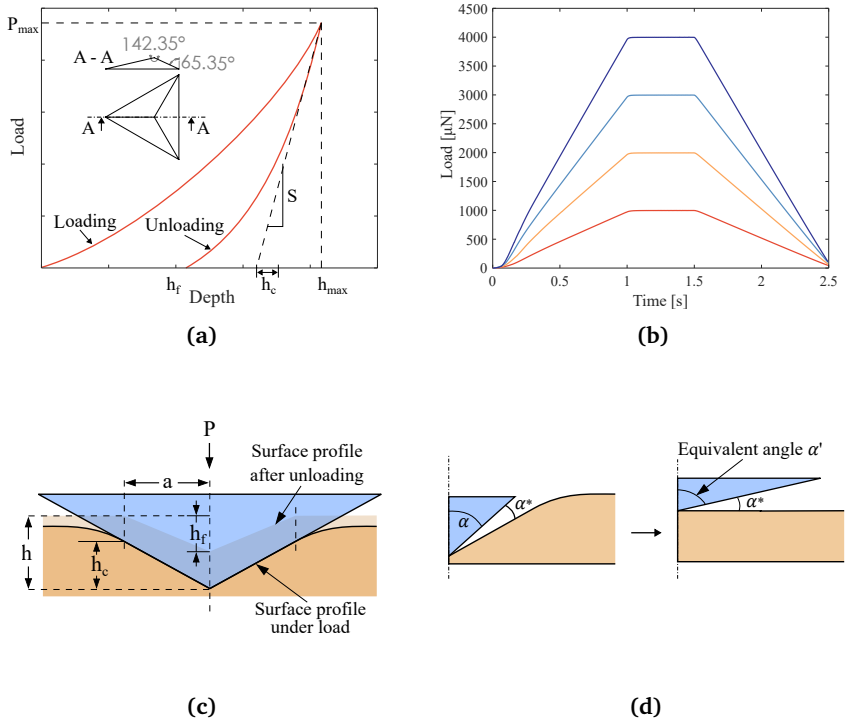

Figure 3.22: (a) Example of P-h curve together with the relevant parameters used in the analysis. In the inset, the geometry of the Berkovich tip according to the nanoindentater manual. (b) Load-time curves imposed to the indenter. (c) Scheme of an imprint for a conical indentation where a is the radius of the projected area at peak load. (d) Definition of effective angle α' for an elastic-plastic nanoindentation.

vs depth h curve following the Oliver and Pharr method [98]:

1. the unloading path of the P-h curve is fitted by a power law of the type

$$P = \hat{A}(h - h_f)^m$$

where $\hat{A}$, h_f and m are fitting parameters. The expression is analytically differentiated and evaluated at h_{max} corresponding to P_{max} to find the contact stiffness

$$S = \frac{dP}{dh}|_{h_{max}},$$

2. the contact depth h_c is the depth for which the indenter is actually in contact with the material. It accounts for the curvature of the material in the

neighbourhood of the indenter tip. It is found as

$$h_c = h_{max} - \varepsilon \frac{P_{max}}{S},$$

where $\varepsilon = 0.75$ is an analytical coefficient accounting for the actual paraboloid shape of the deformed surface below a Berkovich tip,

3. the projected contact area at peak load A, whose equivalent radius is indicated as a in figure 3.22c, is a function of h_c. For a perfect Berkovich tip: $A(h_c) = 24.5h_c^2$. Because of the tip blunting however, this is better approximated by a polynomial function $A(h_c) = 24.5h_c^2 + C_1h_c^1 + C_2h_c^{1/2} + C_3h_c^{1/4} + ... + C_8h_c^{1/128}$. This is found by an iterative fitting procedure done while indenting a material with known Young's modulus, usually fused quartz or aluminum. Oliver and Pharr assumed and observed that the Young's moduli of the materials indented are not dependent on the contact depth and that a single area function can be used for materials on a wide range of Young's moduli,
4. the hardness is obtained as
$$\mathsf{H} = \frac{P_{max}}{A}$$
where A is evaluated at the peak load for each test. H is defined as the mean pressure undergone by the material at P_{max},
5. finally, the reduced modulus is obtained as

$$E_r = \frac{\sqrt{\pi}}{2} \frac{S}{\sqrt{A}}. \tag{3.8}$$

The last relationship was derived from Sneddon [99] that solved the analytical problem of a conical tip indenting a linear elastic semi-infinite half space. He derived the P - h analytical relationship:

$$P = \frac{2E_r \tan\alpha}{\pi} h^2. \tag{3.9}$$

Differentiating with respect to h, the slope is obtained as:

$$\frac{dP}{dh} = \frac{4E_r \tan\alpha}{\pi} h. \tag{3.10}$$

Moreover, he also found that $h_c = \frac{2h}{\pi}$ (this is also the expression at the origin of the coefficient ε given above) and hence $A = \pi h_c^2 \tan\alpha^2 = \frac{h^2 \tan\alpha^2}{\pi}$. Substituting this last expression in equation 3.10, equation 3.8 is retrieved. This is valid for both elastic and elastic–plastic indentations by assuming that the initial unloading segment of the load–displacement curve is linearly elastic.
However, to model the unloading path under the assumption of elastic unloading, the Sneddon solution 3.9 must be modified: the angle α with an effective angle α' (see figure 3.22d). This is because the unloading is interpreted as a loading path

occurring on an imprinted surface while the Sneddon solution would be applicable only on a flat space.
Later researches found that the equation works well for all axisymmetric indendeters with infinitely differentiable profile provided that a correction factor β is added. For a pyramidal Berkovich tip, the corrected indentation modulus is then

$$E_r = \frac{\sqrt{\pi}}{2\beta}\frac{S}{\sqrt{A}}. \tag{3.11}$$

Here, β will be taken as 1.034 as in [50].
In general, for an isotropic material, the Young's modulus $E_{specimen}$ and Poisson's ratio $\nu_{specimen}$ are obtained by simply reverting the relation

$$\frac{1}{E_r} = \frac{1-\nu_{specimen}^2}{E_{specimen}} + \frac{1-\nu_{indenter}^2}{E_{indenter}} \simeq \frac{1-\nu_{specimen}^2}{E_{specimen}}, \tag{3.12}$$

where $\nu_{indenter} = 0.07$ and $E_{indenter} = 1140$ GPa for a diamond tip. The approximation holds when $E_{indenter} >> E_{specimen}$ or when the indenter is rigid.
However, as observed from FIB-SEM investigation, Sigraflex® and and FG have a strongly oriented microstructure at the indentation scale. If the anisotropy is not neglected, then the indentation modulus is a weighted average of the elastic constants relative to the indentation direction. According to Delafargue and Ulm [100], for a transversely isotropic material indented along the symmetry axis (out-of-plane), this reads:

$$M = \frac{1}{\pi H} \tag{3.13}$$

where

$$H = \frac{1}{2\pi}\sqrt{\frac{C_{11}}{C_{31}^2 - C_{13}^2}\left(\frac{1}{C_{44}} + \frac{2}{C_{31}+C_{13}}\right)} \tag{3.14}$$

and the components of the stiffness tensors C are expressed in Voigt notation:

$$\begin{aligned} &C_{11} = C_{1111}, && C_{13} = C_{1133} = C_{3311}, \\ &C_{44} = C_{2323} = C_{1313}, && C_{33} = C_{3333}, \\ &C_{31} = \sqrt{C_{11}C_{33}} > C_{13}. \end{aligned}$$

In this case, M would replace E_r in equation 3.9 and again the load-displacement response follows the same quadratic law. However, to decouple the contribution of all these parameters, combined nanoindentation tests are needed in the in-plane and out-of-plane directions. These were not performed here and the indentation modulus will be extracted by means of equation 3.11. However, the definition of M will be used in section 4.5.2 for discussion on Sigraflex® elastic properties and in section 4.6 for the validation of the FE model.

3.7.3 Results: static tests

The averaged P-h responses are presented in figure 3.23a. None of the loading paths showed pop-ins or discontinuities and the aspect is that typical of elastic-plastic materials. The viscous effect and any dependence on loading rate were not considered as affecting the results because of the negligible change in rate imposed. The curves were also analyzed in figure 3.23b after normalization with respect to both h_{max} and P_{max}. As can be observed, the amount of inelastic depth is independent on both the maximum depth and load, and on average was $\simeq$ 60% of h_{max}. The loading and unloading paths does not show clear differences by going down to deeper h_{max} and the underlying area is nearly constant. Hence,

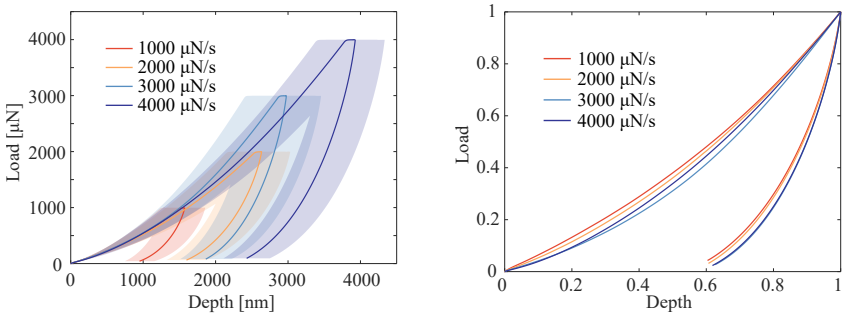

Figure 3.23: (a) Average P-h curves. These were obtained by averaging along the depth axis, keeping the imposed load fixed. The scatter band stands for one standard deviation (upper and lower). (b) Average P-h curves, normalized with respect to both P_{max} and h_{max}.

indenting such material at 1 µm or 4 µm does not change significantly the scale of the phenomena involved in the response. However, there might be a size effect affecting both the modulus and the hardness, as shown in figure 3.24. The boxplot in figure 3.24a shows the median values of the indentation modulus including the 25^{th} and 75^{th} percentiles in MPa. These are:

360.239 [302.74477.1], 284.199 [227.075328.99],
374.629 [284.75464.73], 271.199 [238.02309.73],

for 1000 - 2000 - 3000 - 4000 µN/s, in order. The overall median value is 322.56 MPa.

Plotting the four median values versus the corresponding contact depth (inset of figure 3.24) shows a decreasing trend of the indentation modulus. Similarly, the hardness suffers of the same effect and does not reach any asymptotic value even at 4 µm. The nanohardness or even better the hardness are usually correlated to the yield strength of a material by [101]:

$$H = C\sigma_y. \tag{3.15}$$

For metals, it has been shown empirically that C ≃ 3 while for porous materials this can be much lower down to 1. Therefore, the impossibility to find a yield point under uniaxial compression pointed out already in the macro-scale tests section 3.6.4 may also constitute a meaningful motivation for the hardness size effect. This can be confirmed by deeper indentations tests such as macro-indentations which, although involving of a larger volume of material and porosity, should give the same result.

Finally, from the measurements of the contact stiffness found as in equation 1,

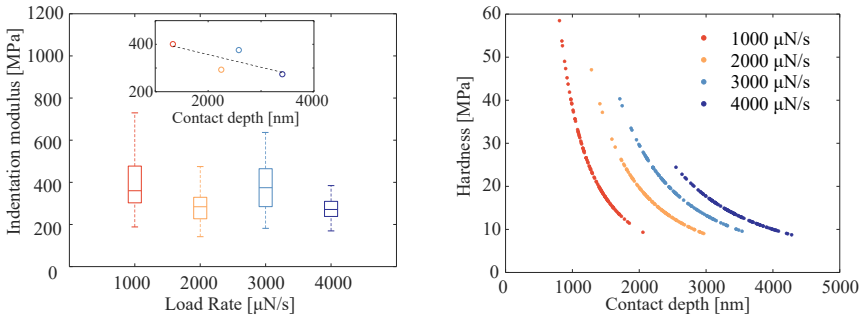

Figure 3.24: (a) Indentation modulus M plotted against the load rate and (inset) the contact depth h_c. It is not obvious whether or not M is dependent on h_c. (b) H-h_c data.

the effective angle α' can be calculated as in [96]:

$$\alpha' = \arctan\left[\frac{1}{2h_e}\sqrt{\pi\, A(h_c)}\right] = 81.85^\circ \quad [80.46^\circ, 82.6^\circ] \tag{3.16}$$

where $h_e = h_{max} - h_{final}$ is the elastic deformation. The uncertainty is derived from the uncertainty in the experimental contact stiffness.

3.7.4 Discussion: static tests

Cermak et al. [46] reported that the elastic modulus under uniaxial compression in the out-of-plane direction for 1 g/cm^3 FG ranges around 50 MPa. In this work the same quantity was found to be around 30 and 40 MPa (see section 3.6.3). Assuming by contradiction that the material is isotropic, one could calculate the isotropic elastic modulus from the reduced modulus by means of the relation 3.11 and get $E = 322.56$ MPa for $\nu \simeq 0$ or $E = 324.8$ MPa for $\nu \simeq 0.083$: in both cases, one order of magnitude higher than the macro-scale out-of-plane modulus.

One reason for this discrepancy could be the local variation of density: Bonnissel et al. [60] indeed derived analytically that a density gradient should be present from the midline to the surface of compacted graphite sheet due to the compaction

process. This means that FG is expected to be denser on the surface, and stiffer according to the observations of section 3.6 about the initial tangent slope, while softer in the inside core. Indeed, more recently, Efimova et al. [35] reported that the foil investigated (0.3 - 1.5 g/cm^3) had a three-layers structure: two higher density surface layers and one lower density bulk layer, in line with the prediction of Bonnissel et al. The surface density was estimated to be 2 g/cm^3 and was likewise ascribed to the compaction process. However, it was underlined in Cermak et al. that it was not possible to notice any change in density along the thickness from SEM analysis of tensile fractured specimens [17].
In figure 3.25, two nanoindentation *P-h* curves found in literature were also compared with the one found in this work: despite the similar densities, the results are pretty different and underline how other process parameters than density can affect the mechanical properties. From this curves, Khelifa et al. [50] (reference 1 in the same figure) obtained an indentation modulus equal to 190 MPa, in good agreement with that reported for Grafoil®. Although much lower than the indentation modulus found here (322.56 MPa), yet the corresponding elastic modulus would result in a large overestimation of the out-of-plane elastic modulus.
Another suitable reason to motivate the big discrepancy is that the contribution to the indentation modulus is strongly affected by the in-plane directions stiffness components, too. This is ideally true for elastic anisotropic materials according to equation 3.14, but it is not straightforward for FG. To uncouple the contributions of C_{ij} components, additional nanoindentation tests would be requested at least along the in-plane direction. These were not part of in this work, but further insights on this discussion, also supported by FE modeling, will be provided in section 4.6 by exploiting the experimental data from macro-scale testing.

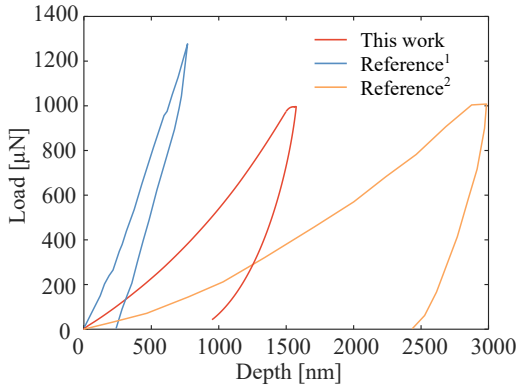

Figure 3.25: *P-h* curves comparison between this work Sigraflex® , 1 g/cm^3, 1 µN/s), [1]Chen and Chung [29] (raw material from Mineral Seal Corporation, 0.86 g/cm^3, 1 µN/s), [2]Khelifa et al. [50]. In the latter case, Papyex®, 1.1 g/cm^3 was used and the tests run in displacement control at 0.05 µm/s).

3.8 Thermomechanical testing

3.8.1 Motivation

As mentioned in the Introduction, the LHC dump working conditions includes both thermal and mechanical loads applied at the same time. The section reports two different test sessions. The first test session aimed to reproduce the thermomechanical conditions in a controlled way, alternatively to the direct proton beam impacts performed in the HiRadMat43 campaign[4]. Due to some complexities arose in this session, the second session was focused only on the thermal load and aimed to investigate the effect of the heating rate on the thermal expansion coefficient once the specimens was completely outgassed.
The coefficient of thermal expansion of FG and Sigraflex® seems to have strong similarities with the thermal expansion of crystalline and polycrystalline graphite (see section 2.4.3). The measurement of this quantity usually involves long heating time (see e.g. [103]) to ensure a uniform distribution of the temperature along the specimen, and also because in principle the thermal expansion coefficient is not rate-dependent.
However, during the HiRadMat43 experiment on a Sigraflex® specimen performed in air, a huge local swelling in the out-of-plane direction of the affected volume was recorded [8], much higher than predicted by simply accounting for the material CTE. The reasons at the origin of this behavior are still unknown: on one side, the trapped gas or the residual chemicals inside the material pores may have played a role in the phenomenon. The fast heating delivered by the impact together with the high tortuosity of the pore space may have not allowed the flowing of the heated region within the impact time and would have provided an additional expansion term. On the other side, it is not excluded that the samples CTE could be rate dependent, maybe as a result of the particular crumpled microstructure.
Although the objectives of this thesis were reduced to the only mechanical investigation, this part was performed at the early beginning of the project when the challenges were still unknown and the goal was to shed some lights on these questions by the controlled decoupling of the mechanical and thermal loads. Nevertheless, the success of this investigation was limited and left much room for improvement, but constitutes a source of fundamental technical know-how for future works willing to focus on the thermomechanical behavior of FG.

3.8.2 Tensile force and heating rate applied

The machine used was a Gleeble GTC 3800 (figure 3.26) equipped with a sealed chamber for vacuum and inert environment (N_2 or Ar). The temperature was increased through the specimen by direct resistive heating i.e., the current flowed

[4]The HiRadMat testing campaign has already been mentioned in the Introduction. These tests are usually performed at CERN and recreate the real-case scenario of a proton beam impact on different materials under various environmental conditions [102]

directly across the contacts between the specimen and the grip, and it was feedback-controlled by means of thermocouples attached to the specimen surface. Tensile loads could be applied at the same time by means of hydraulic actuators. A first round of preliminary tests, not reported here for brevity, led to the adjustments listed below:

- the thermocouples are usually welded to the specimens, but this was not considered as a viable option due to the weakness of the material. A second possibility was to cement them on the surface of the specimen, without penetrating and therefore weakening the sample. However, this option was discarded due to possible influence of the cement on the specimen thickness and hence on the local temperature distribution. The favourite option was then to twin the two nude extremities of a thermocouple and to leave the knot in touch with the specimen surface. The light tension obtained by fixing the other extremities at the machine was responsible for keeping the setup in place (see inset of figure 3.26),
- the original load cell of the machine was substituted to improve the load acquisition: the one in use had 2.2 - 22 kN as maximum load range,
- the use of a IR thermo-camera was assessed: due to the wavelength it could read with the available lenses and the presence of a borosilicate glass on the backdoor, no recording could be obtained. In any case, the available IR-camera setup allowed only for a maximum temperature reading up to 350 °C, and therefore this was not used,
- low-force jaws were installed to facilitate the set-up. Copper flat grips with thickness range 2.0-3.25 mm were preferred.

Figure 3.26: Gleeble GTC 3800 with sealing chamber for vacuum and inert environment

Four tests were performed on dog-bone specimens shown in the inset of figure 3.27.

Test 1: only tensile load

This was intended to verify the capacity to register the force with the new load cell. The chamber was set under high-vacuum and filled with Argon. To prevent the specimen from breaking during creation of vacuum, the hydraulics were kept active so that the jaws did not get pulled together and break the specimen in compression. The test was run at room temperature and constant displacement rate. As observed in figure 3.27, the load cell seems to have enough resolution to record the forces despite the force being small in relation to the load cell range being much larger.

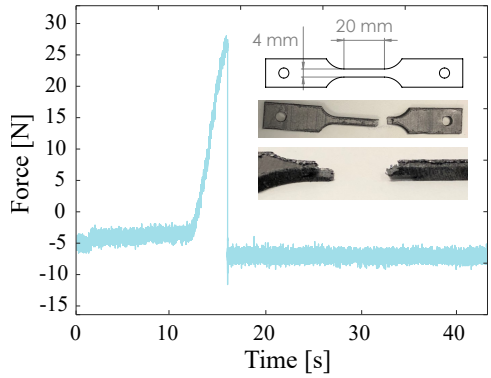

Figure 3.27: Force-time history of a tensile test performed by means of Gleeble GTC 3800

Test 2: only thermal load

This was performed to understand and verify how to impose heat on the specimen and define the heating rate the specimens could handle. K-type thermocouples were used and the environment as well as the grips were kept same as in Test 1. The maximum temperature imposed was 1000°C at different heating rates: 2 – 50 – 100 – 200°C/s. All the tests were run using the same specimen several times. As observed, the temperature control was still satisfactory at 200°C/s up to 1000°C.

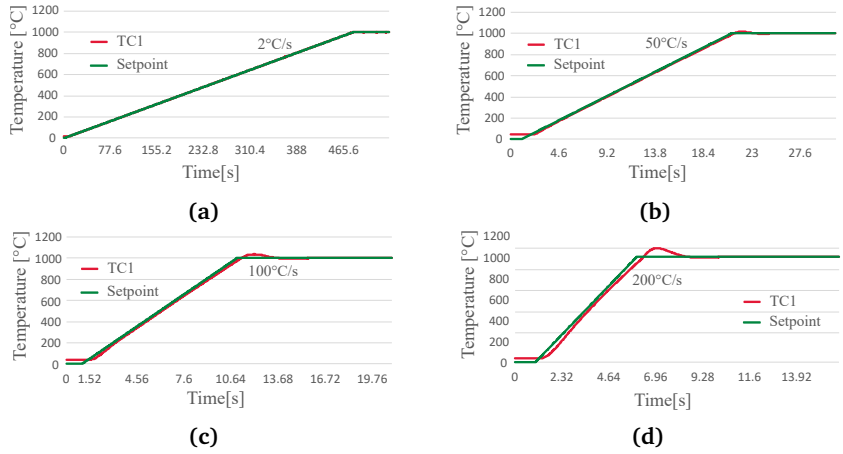

Figure 3.28: Temperature time history: thermocouple measurement compared with machine imposed history at different heating rates. (a) 2 °C/s, (b) 50 °C/s, (c) 50 °C/s and (d) 200°C/s.

Test 3 and 4: tensile and thermal load

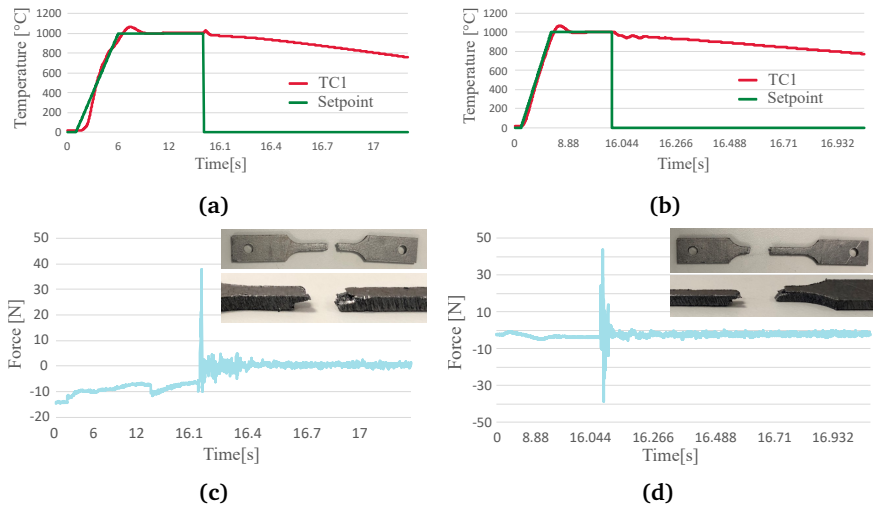

Figure 3.29: (a) and (b) Temperature time histories of test 3 and 4. (c) and (d) corresponding force time histories.

These tests were done combining heating and application of force. They were done to see which stroke rates the specimen could handle while keeping the environment, the gripping and the temperature measurements as in test 1 and 2. In test 4, the heating rates was sped up to 500°C/s. The mechanical load was applied at constant displacement rate 100 mm/s. As obvious from figures 3.29c-d, the res-

ulting data did not allow for post-processing due to low resolution at the applied displacement rate, but the set-up procedure was the result of several optimization iterations and was considered as satisfactory as well as the temperature control method.

3.8.3 Only heating rate applied

As a first outcome from the previous test session, the specimen geometry was changed from dog-bone to stripe-shaped so that the cross-section and the load-bearing capability was tripled (see figure 3.30). A preliminary testing stage was

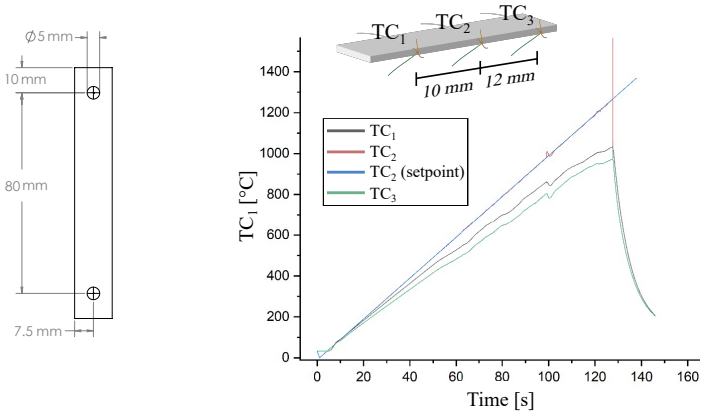

Figure 3.30: Stripe-shaped specimen new design with dimension in *mm* and temperature vs time measurements from thermo-couples in different locations along the specimen.

again performed to compare K-type thermocouples (Ni-Cr(+) vs. Ni-Al (-)) with a 0 - 1250°C temperature range, and R-type thermocouples (Pt - 13% Rh(+) vs Pt(-)) with a temperature range of 0 - 1450°. The goal was to find the peak temperature at which the thermocouples would still work without melting or fail in some way. The K-type thermocouples melted at 1265°C which is 15°C above their nominal temperature range. The R-type thermocouples broke at 1068°C despite the working range was supposed to be up to 1450°C. With these results for the thermocouples, the expectations of reaching temperatures such as 2000°C were scaled back and 1200°C was set as the maximum achievable temperature. The K-type thermocouples were considered as the best choice for this testing session.
One preliminary test was also performed with 3 thermocouples (schematic detail in figure 3.30) to see how the temperature was distributed throughout the graphite specimen when using stainless steel hot grips. These grips gave a well-distributed temperature field.
In order to assess the out-of-plane expansion of the sample, the best option was the so-called edge tracing techinque, which is a simplification of standard DIC:

this captures the displacements of the only specimen outer edges thanks to the contrast with the background. However, due to some issues related to the relative orientation between the DIC camera and machine testing chamber, the entire setup was modified again. Particularly, the standard jaws (the ones used at the very first attempt before Test 1) were considered as the only possible solution to obtain the correct visual access to the specimen. The grips were also changed to steel grips.
The chamber was set to low vacuum (10^3 Pa) and filled with Argon. As described before, three K-type thermocouples were wrapped around the specimen and a temperature profile was imposed up to 1200° at 10 and 1°C/s.

Test 5

The DIC camera was located on the back of the chamber and the light source was on the front side of the chamber with a white paper in front of the light as shown in figure 3.31a. This allowed the sides of the specimen to be dark and

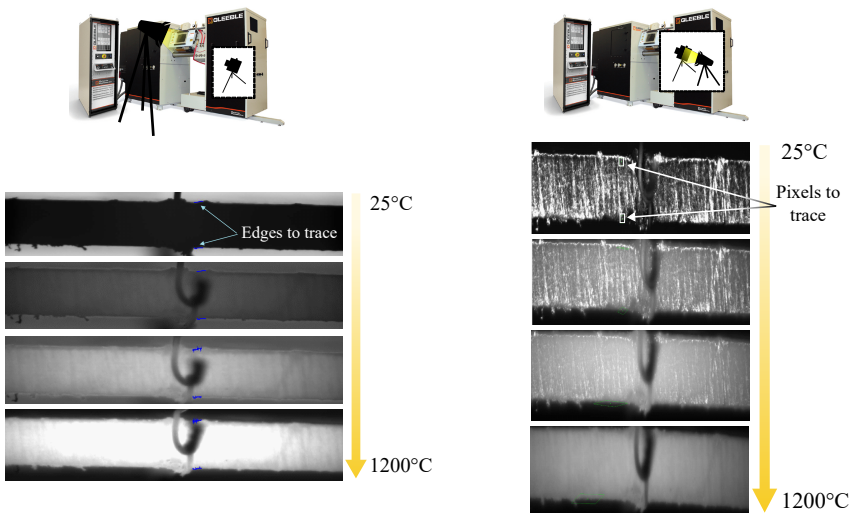

Figure 3.31: (a) Test 5: the contrast between the background and the specimen is not sufficient to obtain a reliable edge tracing. (b) Test 6: the pixel tracing suffered from the same issue at increasing temperature.

with the contrast with the white paper in the background. This test was run at a heating rate of 10 °C/sec. At the beginning of the test, the contrast between the background and the specimen was sufficiently high for imaging, but with the temperature increase, it started to decrease significantly due to the sample emissivity. At this stage, the edge-trace calculations were not reliable anymore. Then, above 1000°C, the specimen-background contrast was again good enough to obtain re-

liable results, but the edges got blurry and easy to confuse with the surrounding halo.

Test 6

Since edge tracing did not provide reliable results because of the blurred edges and the halo effects, the thermal expansion of the specimen was attempted to be obtained by following the distance between two pixels on the outer surfaces, as shown in figure 3.31b. The light source was placed on the chamber back side so that the thickness side surface of the specimen had a black background. In addition, since test 5 showed a strong gradient in the specimen luminosity during heating, the heating rate was set to 1°C/sec, in the way that the camera contrast could be changed by decreasing the exposure time of the camera during the heating.
Unfortunately, when the specimen started to glow, the pixels tracking started to fail again. The contrast with the background was still good, but the specimen's contours faded. At 1200°C most of details on the specimen front surface were almost gone.

Proposed solution

In order to solve the issues encountered, the possibility to use any types of filter to dim the emitted light from the specimen was explored. A possible solution, similar to what is discussed in [104], involves the use of ultraviolet lights and optics to minimize the light emitted by specimens in the concerned temperature range. Another cheaper option would be to use a thermo-resistant spray paint that reduce the emissivity of the specimen while also creating the speckle needed for the DIC analysis.

4. Modelling

4.1 Objectives

FG can be classified as a cellular solid that embodies a three-fold character originated by the hierarchical microstructure. Its response is due to (i) the layered crystalline structure of graphite, (ii) the meso-structure of a crumpled material and (iii) the macro-structure given by cohesive forces between particles, in analogy to compacted powders. The aim of this chapter is to describe and model especially the contributions (i) and (ii) and to support the idea that a full characterization of the response must account in parallel for all the three aspects. The characteristics that a suitable material model should have will be highlighted and the adaptation of a specific model already implemented in LS-Dyna will be shown with the practical purpose of modeling a static nanoindentation test.

4.2 FG similarities with crumpled materials

4.2.1 Microstructure and mechanical properties

Thanks to FIB-SEM imaging, it is clear that FG is a highly porous type of graphite with a complex pore space originated by irreversible crumpling of micro-sheets. Since no binder is added throughout the production process, the micro-sheets can be considered as purely crystalline and having properties more similar to those of graphite single crystals or multi-layered graphene. However, changing the thickness from one to two to a hundred layers of carbon results in mechanical and thermal properties extremely different and that need to be investigated per each case.
An example of such property is the modulus of rigidity associated to the bending stiffness of the carbon planes and to the inherent elastic properties. Considering that the elastic modulus perpendicular to the basal plane of a graphite single crystal (direction c) is $C_{33} = 36.5$ GPa [51], and that the out-of-plane elastic modulus of a less perfect material such as polycrystalline or pyrolytic graphite ranges from 10.88 GPa to 29.35 GPa [105, 106], a simplistic rule of mixture to estimate the out-of-plane modulus $E_{\perp}$ of FG would give a value in the order of magnitude of $1-10$ GPa i.e., a hundred times bigger than the actual tangent modulus: compare

with values found in this work and from Cermak et al. [46]: 30 - 50 MPa.
A good explanation to this big discrepancy can be given by regarding FG as having a crumpled meso-structure in which the bending rigidity of the constitutive micro-sheets plays the major role under compression loads. Indeed, the ratio between the bending and stretching in-plane rigidity of an elastic plate scales with $(h/L)^2$, that is the square of the ratio between its thickness h and width L.
The h/L ratio of a single FG micro-sheet with $h \sim 0.1$ µm and $L \sim 100$ µm can be estimated as in the order of 10^{-3}. This gives a modulus $E_\perp \sim 1$ MPa that is 10^{-6} times lower than the graphite single crystal in-plane modulus $C_{11} = 1060$ GPa [51]. This is a much better estimate for the compression modulus reported in [20] or [93] for expanded graphite at densities around 0.01 – 0.2 g/cm^3 (see also figure 2.3b) and explains the values for higher density sheets.
Crumpled materials have been partially investigated from a structural point of view, and some works can be found about crumpled paper, crumpled aluminum foils, crumpled graphene and crumpled pyrolytic graphite [107–111]. Crumpled materials are also related to another class of material called entangled materials, which are usually made of compacted metal wires, including aluminum, steel, and titanium [92, 112, 113]. In [114], some similarities between crumpled aluminum and entangled materials under uniaxial compressive loads were highlighted also with respect to crushable foams. These three groups of materials can all be viewed as cellular solids, but the peculiar aspect is in that both crumpled and entangled materials are kept together by contact forces generated by local geometrical configurations that constitute the material meso-structure.
In the case of FG however, the micro-sheets are the entities that undergo the crumpling process as represented schematically in figure 4.1: here a single cell of a expanded worm is crumpled hydrostatically and the micro-sheets are severely distorted. This is made possible by the very low shear forces needed to delaminate the micro-sheets and by the ability of the carbon planes to fold down without breaking. Indeed, Luo et al. [115] reported that a few layers graphene is capable to form curves with ≈ 10 nm in radius without breaking. The resulting meso-structure is

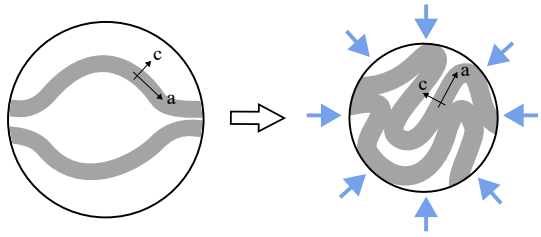

Figure 4.1: Schematic representation of single cell walls crumpling under hydrostatic pressure. a and c are the crystalline axes parallel and perpendicular to the basal planes, respectively.

made of heterogeneous configurations of the micro-sheets: the aligned regions are piled up, well-straighten along the bedding plane and tiny pores run among

them. The misaligned regions are randomly oriented and form zig-zag paths running around much bigger pores. The voids distribution is non uniform as well as the mass distribution is random, like what happens when a paper ball is crumpled under compression forces [116].
The crumpled nature may also explain the huge volumetric strain undergone by the pores during the production process. These, in the uncompacted worms, are roughly equiaxial with wall-to-wall size in the order of ~ 10 μm, while the average size of a Sigraflex® pore is in the order of magnitude of 0.1 μm. This leads to a large volumetric strain that is only explained by the continuous folding of the micro-sheets and implies the modification of the pore space with the creation of new pores in between the folds.
The crumpled nature also explains the impossibility of compacting a FG sheet to a density higher than 1.9 g/cm^3 [17]. The crumpling process is indeed governed by a quantity called fractal dimension D that is a material property. A spherical volume of a crumpled thin sheets with dimensions $L \times L$ obeys a scaling law of the type [117]

$$L^2 \sim R^D$$

at a given compression force, where R is the radius of the sphere and $2 < D < 3$. When $D = 3$, the sheet is completely transformed into a spherical volume and the physical upper bound can be reached thanks to an effective packing. For single layer graphene, it was found $D = 2.36$ [118] while experiments say that most of the materials like paper and aluminum sheets have $2.1 < D < 2.7$ [119]. If a similar value also applied to micro-sheets, this implies that the internal fractal microstructure of FG is retained regardless of the compaction force applied and the maximum density achieved is governed by the fractal dimension of the micro-sheets.

4.2.2 Analogies in the uniaxial compression curves

At the macro-scale then, despite the crumpling process may seem accidental, the randomly folded materials are statistically well-defined and well-reproducible in experiments [119]. The good repeatability of the uniaxial compression tests of Sigraflex® may represent a good example thereof.
In [120], a non-linear elastic region in closed-die compaction of aluminium foils was noticed at low strains (see figure 4.2 for comparison with FG uniaxial cyclic compression curves). This regime was described as *apparent*, resulting from two deformation contributions, one from the material and the other from dry sliding between sheets i.e., the meso-structure. Similarly, Tan et al. [113] argued that a *structural* strain component dominates the initial elastic domain in quasi-ordered entangled aluminium alloys and leads to similar nonlinear stress-strain curves. More examples of akin behaviors can be found in [112, 121].
In analogy therefore, this allows to think of FG initial toe as a combination of material and structural contributions: the first is localized near the creases and involves basal dislocations inside the micro-sheets, while the second can be asso-

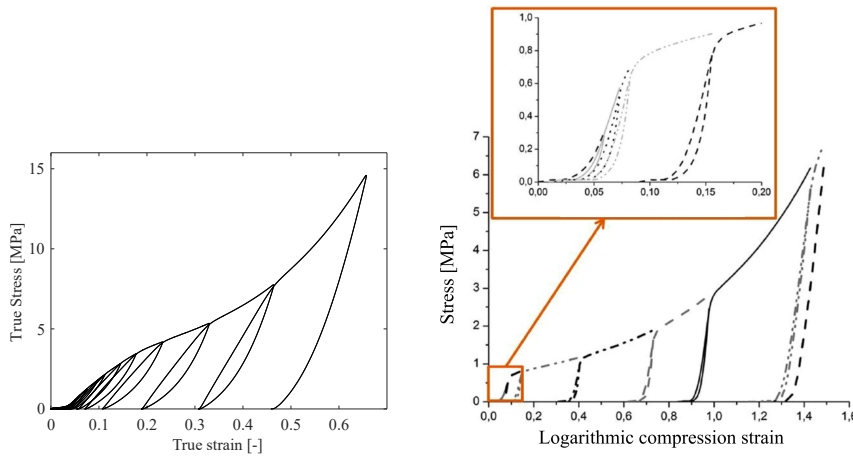

Figure 4.2: (a) True stress vs relative density curves. Both ρ^* and ρ_p^* are used as independent variables. (b) Closed-die compaction curve of a crumpled aluminum sheet [120]. A toe region similar to that observed for Sigraflex® is also evidenced.

ciated to local rigid motions of unstrained micro-sheets that result on large macroscopical deformation.
In [119] it was underlined that the stress relaxation in crumpled aluminum can be treated as a random consequence of individual events of energy dissipation. Therefore, since the toe in FG tests is always fully or partially recovered after unloading in uinaxial cyclic tests, this is attributed to a structural mechanism that is locked and retrieved only when the load is increased or decreased at a stress threshold value (in this case 0.3 – 0.4 MPa). When the compaction load increases, the number of folds and the consequential inelastic strain increase too, and can limit the toe strain recovery associated to the structural mechanism.
The FG transition domain seen in figure 3.17b can be interpreted as a hardening region, opposed to the typical flat plateau occurring in foams due to cell walls' buckling. Hardening and absence of flat plateau were also observed in [114] for crumpled aluminum and they were set among the similarities with entangled fibrous materials.
Cottrino et al. [120] motivated this response by noticing that the stress increases with the number of contact points in a power-law-like dependency. This is also observed in foams at the beginning of the densification regime [95] where the stress-strain curve concavity is turned upward for the whole regime. The FG transition domain is instead peculiar: the stress-strain concavity is downward for at least 20% strain and only later it is turned upward, as if a different mechanism than new wall contacts generation is predominant at this stage. This may originate from the aligned regions where the probability of new contacts is reduced and the de-

formation mechanism is closer to crystalline graphite. As it will be presented in the next section, the stress-relative density relation in the densification regime of FG follows an exponential law instead of a power-law more common in entangled materials or foams [95, 114, 122]. Luo et al. [115] tested crumpled graphene balls by nanoindentation and, given the ability of graphene to fold more severely than other materials, motivated the stiffness and strength increase by formation of more hard-to-bend ridges. This may explain the exponential hardening that is seen in the whole density range 0.1 - 1.7 /cm^3, where also the compression moduli (figure 3.17b) and the cyclic moduli (3.19b) observed in this work evolve accordingly.
Finally, a visible difference between FG and crumpled materials under compression can be related to the nature of the base material, that is, for example in crumpled aluminum the yield point is obvious and the hysteresis area is very limited, where FG has unclear yield stress and large hysteresis loops areas.

4.3 FG similarities with compacted powders

For the sake of completeness, it is emphasized that FG can show some aspects typical of compacted powders. Indeed, FG is nothing else than an exfoliated graphite powder compact with soft particles that aggregate thanks to their meso-structure ability to fold and interlock. Density-dependent properties such as the elastic modulus are common in compacted powders and many material models available in commercial FE software allow for controlling such dependency (see for example Modified Drucker-Prager/Cap plasticity [123]).
Nevertheless, the particles' boundaries and their interaction features are practically indistinguishable in the FIB-SEM images, unless pulled apart on purpose, and not much can be added about the particles behavior under mechanical load.
The role of cohesive forces is probably not observable under compression loads, while it may constitute the key contribution to model the mechanical response under tensile or simple shear loading.

4.4 1D analytical model

Intuitively, the aligned regions described in section 3.2.3 tend to behave like well-ordered graphite at increasing compression forces and the local deformation is expected to be stiffer (also suggested in [26]) and predominantly due to the dislocation mechanisms of the crystalline structure. In [26], these regions were linked to the reversible stored energy of the material.
Conversely, the misaligned regions mainly contribute to the deformation by means of their meso-structure in the sense that the micro-sheets create new folds, new contact points and interlocking constraints. Once sufficiently crumpled, these re-

gions turn into aligned regions and add on their volume fraction to the aligned region volume fraction. The result is an overall stiffening and a shift of the dominant deformation mechanism from the meso-structure to the microstructure.
A simple analytical model is proposed in this section in the attempt to decouple the deformation contributions upon compression coming from the FG graphitic component, associated to the aligned regions, and crumpled component, associated to the misaligned regions.
The aligned regions are here associated to a stress-strain response similar to polycrystalline graphite under compression. This was found to obey a power law of the type [44]:

$$\varepsilon = A\sigma + B\sigma^2, \tag{4.1}$$

where A [MPa^{-1}] and B [MPa^{-2}] are defined as elastic and plastic compliances. The model originated from the intuition of inhomogeneous plastic deformations that gradually participate to the overall deformation and can be visualized as a continuous involvement of additional spring in series. Despite the equation was found to give a good fit only up to a half of the graphite sample strength, this is easy to manipulate and resembles the commonly used Ramberg-Osgood equation when the stress exponent is set to 2. This can be expressed in terms of stiffnesses instead of compliances as:

$$\varepsilon = \varepsilon_e + \varepsilon_p = \frac{\sigma}{E_0} + \frac{\sigma^2}{K}. \tag{4.2}$$

Here E_0 is the elastic modulus of the aligned regions at zero strain and K is a material parameter that accounts for both the volume fraction and stiffness of the aligned regions involved in the plastic deformation. This relation can also be inverted, assuming positive strain $\varepsilon \geq 0$, as follows:

$$\sigma = -\frac{K}{2E_0} + \frac{K}{2E_0}\left(1 + \frac{4E_0^2}{K}\varepsilon\right)^{1/2} \tag{4.3}$$

On the other side, the misaligned regions are associated to a different function of the compressive stress and the *current* relative density ρ^*. This differs from ρ_p^* defined in equation 3.5 since it is related directly to ε by:

$$\rho^* = \frac{\rho_0}{\rho_s} e^{\varepsilon}. \tag{4.4}$$

To formulate the relationship, it is postulated that not only ρ_p^* is related to the compressive stress σ by an exponential law of the type 3.7, but also ρ^* satisfies a similar law.
Indeed, plotting the experimental σ - ρ^* curves in figure 4.3a in semi-logarithmic coordinates, a straight line can be fit in the whole densification regime. For comparison, σ - ρ_p^* curves extracted from the cyclic compression curves were also plotted in the same figure using the initial strain as found in the inset of figure 3.19a and by means of the conversion 3.5.

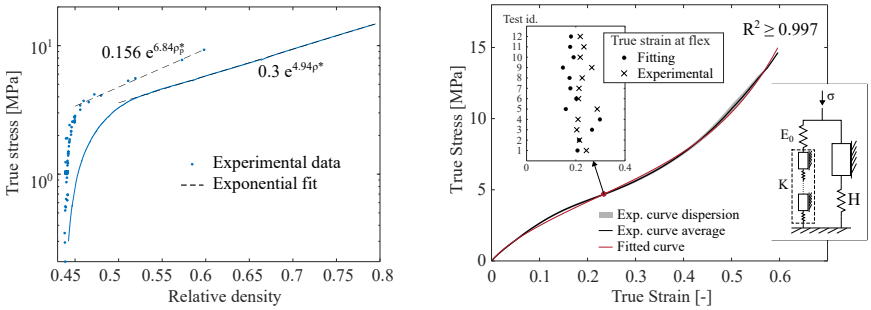

Figure 4.3: (a) True stress vs relative density curves. Both ρ^* and ρ_p^* are used as independent variables. (b) Example of experimental curve fitting by means of equation 4.7, including the scatter in the strains at flex and a schematic view of the proposed rheological model.

The exponential coefficient is in good agreement with that reported in equation 3.7 [46] i.e. 5.88. The difference is ascribed to the uncertainty about the real relative density of the tested specimens in this work.
Assuming that the misaligned regions are those who provide the major deformation contribution in the densification regime, their contribution to the overall compressive modulus can be related to ρ^* by an exponential law, in analogy to the exponential law 3.6 between σ and ρ^* during densification:

$$H = H_0 e^{n\rho^*}. \tag{4.5}$$

Here, H_0 is the initial modulus of the misaligned regions and n is a parameter related to the rate of densification. Relation 4.5 can be easily expressed in terms of ε by use of 4.4:

$$H = H_0 e^{n\frac{\rho_0}{\rho_s}e^{\varepsilon}}. \tag{4.6}$$

The contributions from 4.3 and 4.5 are assumed to work in parallel such as in the equivalent rheological model of figure 4.3b, and the total stress σ versus true strain ε relationship reads:

$$\sigma = -\frac{K}{2E_0} + \frac{K}{2E_0}\left(1 + \frac{4E_0^2}{K}\varepsilon\right)^{1/2} + H_0 e^{n\frac{\rho_0}{\rho_s}e^{\varepsilon}}\varepsilon, \tag{4.7}$$

Equation 4.7 was used to fit the average experimental monotonic curves as shown in figure 4.3b. The toe contribution to the total strain was not included in the averaging procedure.
The statistics of the fitting parameters is reported in table 4.1 together with the corresponding confidence interval. The parameter E_0 was obtained a priori from a high order polynomial fitting of the average curve, whose slope was evaluated

	Median	95% confidence interval
E_0 [MPa]	39.41	(fixed)
H_0 [MPa]	0.04262	(0.0392, 0.04604)
K [MPa^2]	135	(133.2, 136.7)
n [-]	7.091	(6.995, 7.187)

Table 4.1: Statistics of fitting parameters obtained by the mechanical model in 4.7.

at $\varepsilon = 0$, and it was kept fixed during the fitting. Whereas the exponential trend in the densification regime is matched perfectly, much room for improvement is visible in the transition region: this indeed depends on the exponent $1/2$ in equation 4.3 which is already known to partially match the graphite behavior.
The two friction blocks in the rheological model of figure 4.3b were inserted to represent the accumulated inelastic strain and to underline that both the graphitic and crumpled natures give separate contributions to the overall inelastic deformation. The friction block backing the spring series and associated to the fitting parameter K represents the non-recovered deformation coming from dislocations internal to the micro-sheets. The contact forces at micro-sheets interlocks are instead gathered in a separate block representative of such meso-structural contribution. Each spring of the spring series was associated by Jenkins [44] to the elastic stiffness of the plasticizing regions. Here however, these components were not decoupled and K is simply regarded as a fitting parameter that incorporates such stiffnesses as if they were already integrated over the deformed volume and uncoupled from any stress dependency.
At the early beginning of deformation, E_0 and H_0 act in parallel on behalf of the aligned and misaligned regions, but H_0 is negligible meaning that the former are predominant and E_0 and K determines the initial response. The resultant tangent slope decreases thanks to the contribution of the spring series until it rises quickly for the high rate of densification n. The flexes obtained numerically at the minimum of the stress-strain first derivative match satisfactorily the flexes given by the fitting curves as shown the inset of figure 4.3b.
Despite a 1D model is not comprehensive and direct applications for material modeling are limited, it confirms that the assumptions made about the decoupling of deformation contributions are realistic. The model derived in 4.7 will be used to define the input curves in the material model investigated in sectoin 4.6.6.

4.5 Characteristics of a suitable material model

4.5.1 Overview of the stress-strain curves

Although many differences have been underlined so far between FG and other types of graphite, the models available for the polycrystalline constitute a starting point also for FG modeling.

The uniaxial tensile and compression stress-strain curves of nuclear grade graphite were discussed by Jenkins [44] and other authors already in the 60's. In both the loading directions, these were observed to have a very small and even negligible elastic region, followed by a inelastic non-linear behavior with downward concavity. The same behavior was clearly observed for Sigraflex® and FG in the in-plane tensile tests (figures 3.10 and 3.13), but could be also recognized in the out-of-plane compression tests (figure 3.16) when the stress overcomes the toe region and remains lower than the point of flex. This point can be interpreted as the end of the predominant graphite-like behavior and the beginning of the predominant foam- or crumpled-like behavior, as observed hanks to the mechanical model of section 4.4.
However, many types of graphite are usually described as brittle or quasi-brittle materials in both tensile and compression loading directions, but the same does not applies to FG, where the in-plane tensile behavior is very brittle with low fracture strain ($\sim 0.7\%$), but the out-of-plane compression curve flows plastically up to very large strains (70 - 80 %) with no sign of failure.
Furthermore, synthetic or artificial graphite shows a degree of anisotropy given by the direction and shape of the grains. Isotropic graphite can be obtained by fine and randomly oriented grains while transversal isotropy originates by larger crystals obtained by pyrolysis, such as for pyrolytic graphite, or from compaction, such as for FG.
In addition, different behaviors in tension and compression along the same loading direction are another typical feature of graphitic materials [124, 125], in analogy with ceramics and glasses. Not only the failure strength, but also the initial modulus, the tangent modulus or any plastic internal variables can vary when going from positive to negative strains. Therefore, such a behavior can be expected also for FG and indeed, while in section 3.4, the initial modulus in the tensile in-plane direction was found to be 2288.94 MPa (other values from literature were 1335 MPa [45] and 2290 MPa [26]), the elastic modulus in the compression in-plane mode was found to be around 3500 MPa in [33] by means of ultrasound technique.
Assuming the full reliability of this data, a simple way to guess the stress-strain curve in the in-plane compression direction is to replicate the same non-linear trend as the tensile curve along the same direction and scale it uniformly along the stress axis until the derivative at the origin matches the value found in [33]. This is how the plot in figure 4.4a was obtained.
Of course, this is a trivial procedure and the scale factor must be considered as a new parameter of investigation.
The tensile out-of-plane compression curve has never been measured while the only known property is the out-of-plane fracture strength equal to 0.03 - 0.04 MPa [38]. Hence, the stress-strain curve in figure 4.4b was obtained by taking the same tangent at the origin of the compression curve and by extending the linear trend up to the fracture strength.
In summary, the montonic stress-strain curves of FG are expected as non-linear

in both the in-plane and out-of-plane directions, with possible asymmetry in the strain axis given by a pressure-dependent behavior.

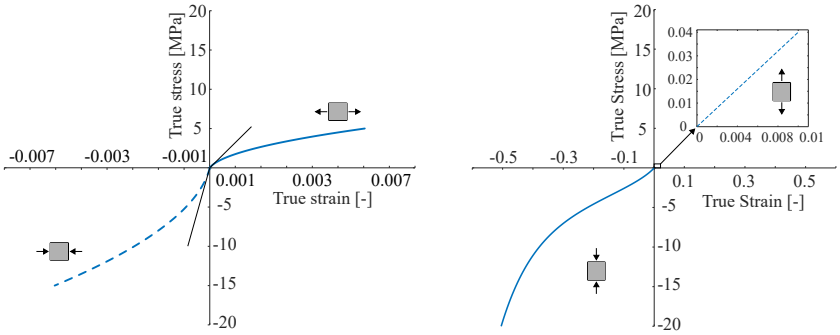

Figure 4.4: (a) In-plane stress-strain curves for FG. The tangent lines at the origin highlight the difference in modulus when the load is reversed. (b) Out-of-plane curves for FG.

4.5.2 Elastic properties

A very first approximation at small strains for Sigraflex® behavior, that is also suitable for exploratory FE simulations, could be the orthotropic elastic material model of the type $\sigma_{ij} = C_{ijkl}\varepsilon_{kl}$.
Here C_{ijkl} are the components of the elastic stiffness tensor C for FG, also called elastic moduli. The inverse of the stiffness tensor C is the compliance matrix $S = C^{-1}$ and can be expressed in Voigt notation as a function of the engineering elastic constants. This links the stress σ_{ij} to the strain ε_{kl} components expressed by the same notation. The relation reads:

$$\begin{bmatrix} \varepsilon_{11} \\ \varepsilon_{22} \\ \varepsilon_{33} \\ \varepsilon_{12} \\ \varepsilon_{23} \\ \varepsilon_{31} \end{bmatrix} = \begin{bmatrix} \frac{1}{E_{11}} & -\frac{\nu_{21}}{E_{22}} & -\frac{\nu_{31}}{E_{33}} & 0 & 0 & 0 \\ -\frac{\nu_{12}}{E_{11}} & \frac{1}{E_{22}} & -\frac{\nu_{32}}{E_{33}} & 0 & 0 & 0 \\ -\frac{\nu_{13}}{E_{11}} & -\frac{\nu_{23}}{E_{22}} & \frac{1}{E_{33}} & 0 & 0 & 0 \\ 0 & 0 & 0 & \frac{1}{G_{12}} & 0 & 0 \\ 0 & 0 & 0 & 0 & \frac{1}{G_{23}} & 0 \\ 0 & 0 & 0 & 0 & 0 & \frac{1}{G_{31}} \end{bmatrix} \begin{bmatrix} \sigma_{11} \\ \sigma_{22} \\ \sigma_{33} \\ \sigma_{12} \\ \sigma_{23} \\ \sigma_{31} \end{bmatrix} \tag{4.8}$$

For transversely isotropic material in the 1-2 plane, such as Sigraflex® or FG in general, one can set

$$E_{11} = E_{22} \qquad \nu_{31} = \nu_{32} \qquad G_{31} = G_{23}$$

so that the number of independent parameters for the elastic response is limited to five:

$$E_{11}, E_{33}, \nu_{12}, \nu_{31}, G_{23}. \tag{4.9}$$

Moreover, by the symmetry of C and from the in-plane isotropy, it follows

$$\nu_{21} = \nu_{12}\frac{E_{22}}{E_{11}} = \nu_{12},$$
$$\nu_{13} = \nu_{31}\frac{E_{11}}{E_{33}},$$
$$\nu_{23} = \nu_{32}\frac{E_{22}}{E_{33}} = \nu_{31}\frac{E_{22}}{E_{33}},$$

and

$$G_{12} = \frac{E_{11}}{2(1+\nu_{12})}. \tag{4.10}$$

Assuming that the FG response is fully elastic, only two out of five elastic parameters are known so far from the experimental tests i.e., $E_{11} = E_{22} = 2290$ MPa and $E_{33} = 30-40$ MPa[1]. The in-plane Poisson's ratio ν_{12}, the out-of-plane Poisson's ratio ν_{13} and the out-of-plane shear modulus G_{23} are missing and should be guessed reasonably:

- ν_{12} is the in-plane Poisson's ratio. In general, graphite single crystals have in-plane Poisson's ratio equals to 0.164 [51], but here the high porosity leads to think of a even lower transverse deformation. The latter is hardly visible from the images of both macro and micro-scale tensile tests because of poor image resolution, but it is supposed to be negligible with respect to the longitudinal deformation. For simplicity then, $\nu_{12} \simeq 0$, also constant with the applied deformation,
- ν_{31} it the Poisson's ratio that determines the in-plane deformation (direction 1) given by an out-of-plane compression (direction 3). To estimate that, one could use the measurements reported in section 3.6.6 assuming that most of the total deformation is plastic, so that $\nu_{31} = 0.083$, again constant through the whole strain domain ,
- G_{23} is probably the most challenging elastic property to measure experimentally. A practical approach for a realistic guess may be that shown in [126], that is:

  $$G_{23} = \frac{\sqrt{E_{22}E_{33}}}{2(1+\sqrt{\nu_{23}\nu_{32}})}.$$

  where $\nu_{31} = \nu_{32}$ due to transverse isotropy and $\nu_{23} = \nu_{32}E_{22}/E_{33}$ from the simmetry of C. Setting $E_{22} = E_{11} = 2290$ MPa and $E_{33} = 30-40$ MPa, it is finally obtained $G_{23} = 76-93$ MPa. Again for simplicity, this is assumed as constant with the applied deformation.

[1] From the linear fitting of the experimental curves in section 3.6.5, a mean value of 34.35 MPa was obtained, while from the derivative of polynomial fitting also used in section 4.4, this value was 39.02 MPa.

From these values, the in-plane shear modulus resulted from equation 4.10 as $G_{12} = 1145$ MPa. Therefore, a first set of suitable elastic parameters can be that reported in table 4.2. Here, all the nine orthotropic parameters are reported but only five are independent due to transversal isotropy.

$E_{11} = 2290$ MPa	$E_{22} = 2290$ MPa	$E_{33} = 30-40$ MPa
$\nu_{21} = 0$	$\nu_{31} = 0.083$	$\nu_{32} = 0.083$
$G_{12} = 1145$ MPa	$G_{23} = 76-92.95$ MPa	$G_{31} = 76-92.95$ MPa

Table 4.2: Set of elastic parameters for the orthotropic elastic material model.

To improve the guess about G_{23}, the results from static nanoindentation tests were further analyzed as follows. By means of the Sneddon formula 3.9 and the effective angle α' (equation 3.16), the unloading experimental curve can be matched under the assumption of pure elastic unloading. To do so, the compliance matrix S needs to be built with the parameters in table 4.2 and then inverted to obtain the components of the stiffness tensor C_{ijkl} to plug in the Delafargue and Ulm equation 3.14 for the calculation of the indentation modulus M. The load-displacement curve is finally obtained by using M in the Sneddon solution.
While building the compliance matrix S however, the elastic parameters must satisfy the following inequalities (see LS-DYNA Theory Manual[2]) to ensure that the material is thermodynamically stable:

$$\begin{aligned}
&E_{11}, E_{22}, E_{33}, G_{12}, G_{23}, G_{31} > 0 \\
&|\nu_{12}| < (E_{11}/E_{22})^{1/2} \\
&|\nu_{31}| < (E_{33}/E_{11})^{1/2} \\
&|\nu_{32}| < (E_{33}/E_{22})^{1/2} \\
&1 - \nu_{12}\nu_{21} - \nu_{23}\nu_{32} - \nu_{31}\nu_{13} - 2\nu_{21}\nu_{32}\nu_{13} > 0
\end{aligned} \tag{4.11}$$

As a consequence of the stiffness symmetry $\nu_{ij} = \nu_{ji}\frac{E_{ii}}{E_{jj}}$, the second, third and fourth inequalities could be expressed alternatively as:

$$\begin{aligned}
|\nu_{21}| &< (E_{22}/E_{11})^{1/2} \\
|\nu_{13}| &< (E_{11}/E_{33})^{1/2} \\
|\nu_{23}| &< (E_{22}/E_{33})^{1/2}
\end{aligned}$$

If the value $E_{33} = 30$ MPa is used for the calculation, the parameters reported in table 4.2 leads to satisfy all the conditions except 4.11. The reason was ascribed to the large difference between the elastic moduli in the in-plane and out-of-plane directions; indeed, simply setting $E_{33} = 40$ MPa could fulfill all the conditions. This also means that extreme care must be taken every time these parameters are

[2] `https://www.dynasupport.com/manuals`

tweaked for numerical simulations that have in input orthotropic elastic parameters. For this reason, the values $E_{33} = 40$ and $G_{23} = 92.95$ MPa were preferred over $E_{33} = 30$ and $G_{23} = 76$ MPa.
The final indentation modulus M with this set of values was 149.94 MPa and the Sneddon solution could be plotted as in figure 4.5a. The unloading curve is still far

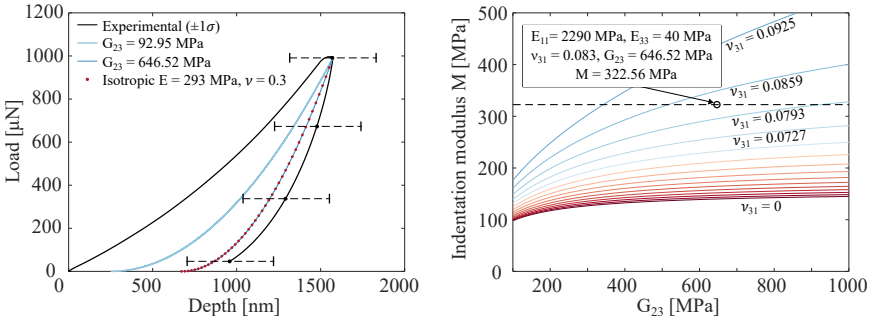

Figure 4.5: (a) P-h comparison between this work experimental and analytical solution by Sneddon. All the analytical curves were shifted so that the maximum displacements match. The dispersion of experimental data in the unloading path indicates one standard deviation far from the median value. (b) Indentation modulus M dependency on G_{23} and Poisson's ratios ν_{31}.

from the experimental unloading curve as well as from the experimental indentation modulus $M = 322.56$ MPa. Hence, a simple one-parameter optimization was performed to improve the matching. All the parameters except G_{23} were fixed until the experimental value of the indentation modulus was retrieved. The optimal value obtained was $G_{23} = 646.52$ MPa.
This is of course very simplistic and variations of other parameters could also affect the final value of M, including the equivalent included angle α' that was not observed experimentally and ν_{31}.
In particular, ν_{31} was varied from 0 to the upper limit imposed by the thermodynamic i.e., $|\nu_{31}| = (\frac{E_{33}}{E_{11}})^{1/2} = 0.132$. As can be seen in figure 4.5b, many optimal solutions are available at the same value of M if both ν_{31} and G_{23} are changed accordingly. Large variations of G_{23} request small variation of ν_{31}, allowing to think of a bigger influence of G_{23} to the elastic response. Moreover, the material becomes unstable when ν_{31} is increased above 0.0925 or G_{23} is decreased below 341.4 MPa, and hence the only stable solution domain is $\nu_{31} \leq 0.0925$ and $G_{23} \geq 341.4$ MPa.
An equivalent isotropic material would match the unloading curve at $E = 293$ MPa and $\nu = 0.3$ thus giving elastic parameters substantially inconsistent with experimental observations.
To minimize the number of dependent parameters, ν_{31} was left unchanged to its original assumption while the shear moduli value was increased to $G_{23} = G_{31} =$

646.52 MPa.
The set of elastic parameters is finally adjusted as in table 4.3.

$E_{11} = 2290$ MPa	$E_{22} = 2290$ MPa	$E_{33} = 40$ MPa
$\nu_{21} = 0$	$\nu_{31} = 0.083$	$\nu_{32} = 0.083$
$G_{12} = 1145$ MPa	$G_{23} = 646.52$ MPa	$G_{31} = 646.52$ MPa

Table 4.3: First suitable set of elastic parameters for orthotropic elastic material model

Due to the uncertainties on the size of the elastic domain, the term *elastic* is used here to refer to the material properties at the early beginning of the loading path. For example, the elastic moduli E_{11} and E_{33} are used for the initial tangent slope of the corresponding stress-strain curves. Nevertheless, a material model that is fully linear elastic is clearly not the best option even at small strains due to the non-linearity of the stress-strain curves and the intrinsic presence of plastic deformation since the early beginning of deformation.

4.5.3 Coupling of the uniaxial non-linear behaviors: Jones and Nelson model

The model originally proposed by Jones and Nelson [124] for artificial graphite appears as the simplest option to extend and couple the non-linear stress-strain behaviors observed separately in different uniaxial directions. This model was developed in the 70's while it is still on used in recent works such as [127] where a cutting simulation of carbon/carbon composites was modeled.
The model assumes that each mechanical property Y_i, such as the elastic moduli (derivative at the origin), the secant moduli σ/ε and the Poisson's ratios, is a function of the strain energy U:

$$Y_i = A_i \left[1 - B_i \left(\frac{U}{U_0} \right)^{C_i} \right] \tag{4.12}$$

where

$$U = \frac{1}{2} (\sigma_{11}\varepsilon_{11} + \sigma_{22}\varepsilon_{22} + \sigma_{33}\varepsilon_{33} + \sigma_{23}\varepsilon_{23} + \sigma_{31}\varepsilon_{31} + \sigma_{12}\varepsilon_{12}) \tag{4.13}$$

and A_i is the initial value for the property Y_i with the dimensions of the property itself. B_i and C_i are dimensionless fitting parameters that stand for the initial curvature and the curvature change of the stess-strain curves. Lastly, U_0 is an arbitrary value usually selected as equal to 1 so to make the factor inside the square brackets dimensionless.
The strain energy U is independent on the coordinate system and characterizes the elasto-plastic response under multiaxial stress-strain states. This requests previous knowledge of at least the uniaxial stress-strain responses in the principal

directions including the shear directions. For FG, the tensile in-plane and compression out-of-plane uniaxial responses are known (figure 4.6) while the shear directions responses are not. As an example, the stress-strain curves obtained in sections 3.4 and 3.6 are reported in figure 4.6a and 4.6c together with the corresponding secant modulus-U function $Y_i = Y_i(U)$ in figures 4.6b and 4.6d.
The parameters A_i, B_i and C_i were simply fitted by non-linear least square regression. The compression curve in figure 2.3b shows a change in concavity that is

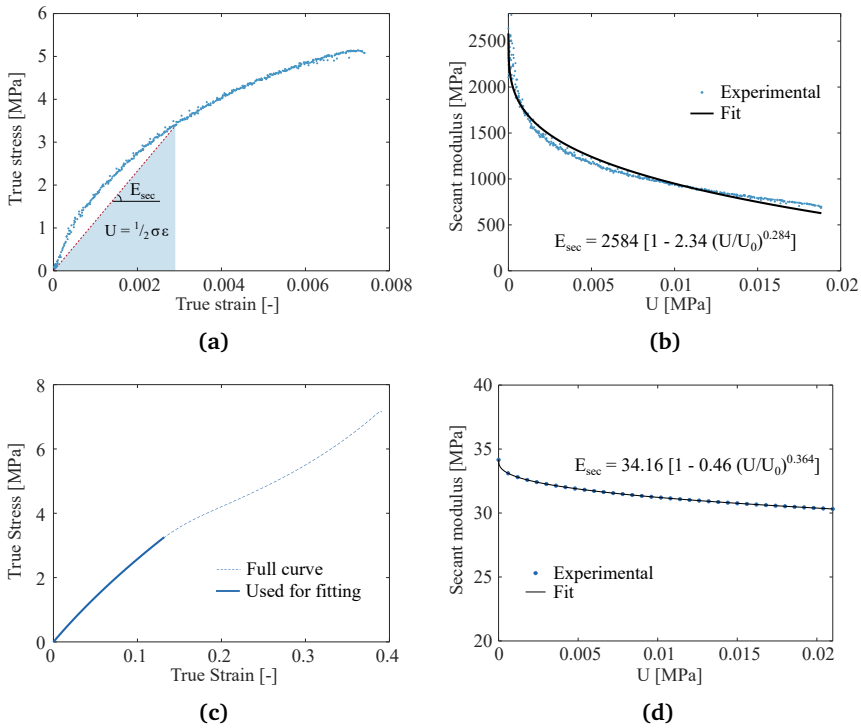

Figure 4.6: (a) Experimental tensile in-plane curve. The definitions of secant modulus and strain energy U are also shown. Their relationship is fitted with equation 4.12 and shown in (b) together with the average fitting coefficients. The same was done for the out-of-plane compression curves in (c) and (d).

not a feature common in graphite and whose secant modulus does not conform to equation 4.12. Hence, the fitting and the applicability of Jones and Nelson model is limited to $\varepsilon \leq 0.13$, in correspondence to the flex where the concavity changes.
Assuming that the Poisson's ratios ν_{12} and ν_{23} characterize the stress-strain behavior for the whole non-linear regime, these could be taken as constant with respect to U by setting $B_i = 0$ in equation 4.12 for both cases.
The same can be done for the unknown out-of-plane shear stress-strain curve corresponding to G_{23}, and its slope can be fixed to a constant value $G_{23} = 646.52$

MPa. Finally, the in-plane shear stress-strain curve can be found by the assumption of transversal isotropy, and its slope taken as equal to $G_{12} = \frac{E_{11}}{2(1-\nu_{12})}$.
Under these hypotheses, the iterative procedure to solve for combined load states looks like the one represented in figure 4.7. For a stress driven problem, equation 4.8 is first solved with the initial values of the material properties Y_i in the compliance matrix S. U_i is calculated with the strain obtained and the stress imposed so that the a new cycle is fully initialized. Then, new values for Y_i are obtained by plugging U_i into equation 4.12 and a new stress state is obtained together with a new value of U_i. If the ratio $\Delta U/U$ does not fall below an arbitrary low threshold, new values for Y_i are found from U_i and a new iteration begins. When the convergence is reached the strain is stored and a new imposed stress is applied.
The procedure just described was implemented in a simple MATLAB code to as-

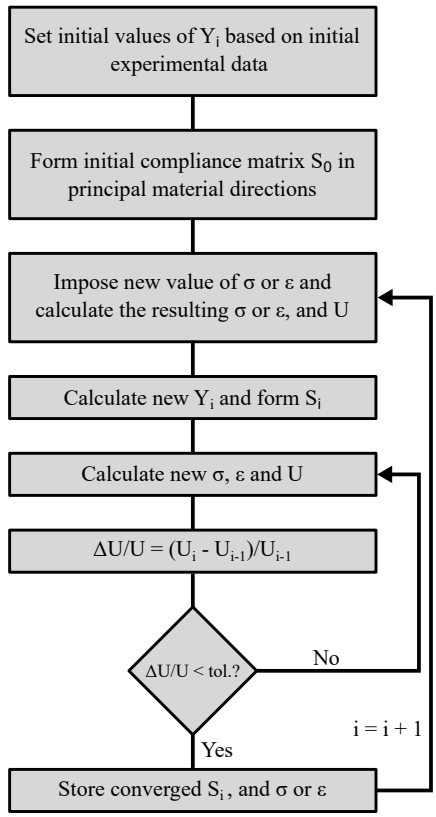

Figure 4.7: Jones and Nelson iterative procedure

sess more in detail the behavior of the material model. In figure 4.8a both uniaxial and biaxial stress responses in directions 1 and 1-2 are displayed. Here it is noticed that due to the non-increasing ν_{12}, the biaxial response shows softening with respect to the uniaxial in-plane response. This feature was reported by Jones and

Nelson [124] for artificial graphite and recognized as a marked difference with behaviors of other materials such as aluminum.
Applying compression along the direction 3 (the softest one) together with biaxial tension in the plane 1-2, leads to higher strains at the same maximum stress with respect to the case were only uniaxial compression along 3 is applied (see figure 4.8b).
Applying compression along direction 3 with biaxial compression in the 1-2 plane leads to the opposite behavior, and hence to a stiffening along the direction 3. This behavior can be realistic also for FG but should be supported by multi-axial experiments.
A limitation of this model is that U combines the contributions of maximum stresses from all the directions and may reach values that were not actually achieved in the uniaxial experimental curve but are only the result of bad extrapolation of the fitting function. For example, the fitting reported in figure 4.6b goes to zero when $U = U_0 B^{-1/C} = 0.05$ and hence the secant moduli turns into a negative value. This should be fixed by constraining the fitting parameters so to obtain a larger suitable domain for the strain energy.
An advantage of this model is that it is easy to implement, also on a FE software

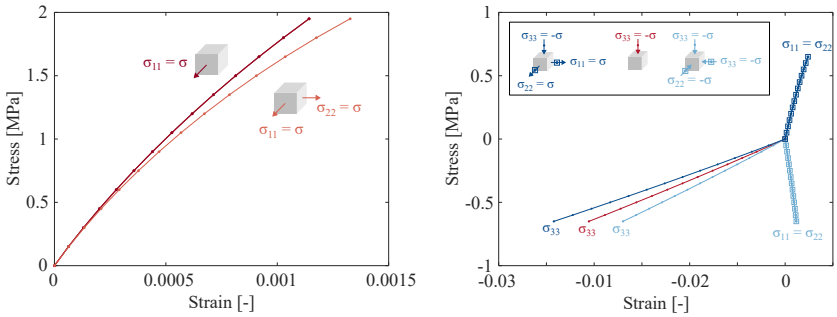

Figure 4.8: Behavior of Jones and Nelson model under multi-axial loading. (a) In-plane uniaxial and biaxial load, and (b) uniaxial compression along 3 together with in-plane biaxial tension and compression.

by means of a user defined subroutine, but the efficiency in the calculation should be checked since the strain energy convergence should be solved per each element at each step inside the material subroutine. In addition, the model is capable to account for different behaviors in tension and compression if a *weighted compliance matrix* is used. This is based on the attribution of a positive U to tensile stress states and negative U to compression stress states. Then, a tensile compliance S^t and a compression compliance S^c can be defined whose components are chosen according to the following four cases (see [127]):

1. $\sigma_{ij} > 0$ and $\sigma_{ji} > 0$:

$S_{ii} = S^t_{ii}, S_{ij} = S^t_{ij} = S_{ji}, S_{jj} = S^t_{jj}$

2. $\sigma_{ij} < 0$ and $\sigma_{ji} < 0$:
   $S_{ii} = S^c_{ii}, S_{ij} = S^c_{ij} = S_{ji}, S_{jj} = S^c_{jj}$
3. $\sigma_{ij} > 0$ and $\sigma_{ji} < 0$:
   $S_{ii} = S^t_{ii}, S_{ij} = k_{ij}S^t_{ij} + k_{ji}S^c_{ij}, S_{ji} = k_{ji}S^c_{ji} + k_{ij}S^t_{ji}, S_{jj} = S^c_{jj}$
4. $\sigma_{ij} < 0$ and $\sigma_{ji} > 0$:
   $S_{ii} = S^c_{ii}, S_{ij} = k_{ij}S^c_{ij} + k_{ji}S^t_{ij}, S_{ji} = k_{ji}S^t_{ji} + k_{ij}S^c_{ji}, S_{jj} = S^t_{jj}$

where $k_{ij} = \frac{|\sigma_{ij}|}{|\sigma_{ij}|+|\sigma_{ji}|}$ and $k_{ji} = \frac{|\sigma_{ji}|}{|\sigma_{ij}|+|\sigma_{ji}|}$ are defined as flexibility coefficients. The correct case is chosen per each element based on the imposed stress at the current step. This part has not been tested here but it is suggested for future works that may focus on the FE implementation of a similar material model for FG.

4.5.4 Load reversal and compressibility under plastic flow

The Jones and Nelson model can be a first approach to couple the non-linear responses when the material undergoes multi-axial stress states. However, given the total strain formulation, it cannot predict some accumulated properties such as the total plastic strain or the hysteresis, and hence cannot model the unloading response as observed in the experiments of Sigraflex® .
This model is indeed a sort of extension of the more famous Ramberg-Osgood constitutive law to a three dimensional case, but it is capable to replicate both the anisotropic plastic behavior and the volumetric deformation in the plastic regime. The latter is a critical property that is missing for example in the implementation of deformation plasticity model (based on Ramberg-Osgood law) in Abaqus[3].
Another desired feature of this kind of plasticity as well as Jones and Nelson plasticity is that there is no yield function involved as in the classical plasticity, and hence there is no need for a yield strength to be defined. If the same zero-yield feature needs to be modeled within a classical plasticity framework, some complexities may arise. A first solution may be that of employing a two-surface plasticity model. One example could be that proposed by Dafalias and Popov [128] that presented also a modification thereof for ATJ graphite that was showing a *vanishing* elastic domain. The advantage of this model is that a bounding surface is defined, in addition to the usual yield surface, having the normal vector equal to that of the enclosed yield surface so to prevent it from being undefined when the yield strength is set to zero.
An alternative model that made use of more than one yield surface to overcome the same issue is the one developed by Greenstreet and Phillips [129]; here at each load reversal a new yield surface is originated and expands generating plasticity also during unloading.
Although two-surface plasticity models are widely used for metals and are capable

[3]Online Simulia User Assistance 2022 - Dassault Systemès - Deformation plasticity

of describing many cyclic characteristics including the Bauschinger effect, the cyclic hardening or softening, ratcheting, and the stress relaxation, these become of complex implementation especially for anisotropic and pressure-dependent materials such as FG.
Other material models that can embody compressibility and anisotropy under plastic deformation are crushable foams and soils or compressed powders. These make use of elliptical or spherical yield surface with associative or non-associative flow rule to model the compressible plastic behaviors given by pore closures. In this case, a yield strength is requested, but a sufficiently low values may be given as input so to have a negligible elastic domain. Since a wide variety of crushable foam models is already implemented in LS-Dyna, these were the first and the only ones investigated in this work.

4.6 FE nanoindentation model

4.6.1 Objective

A nanoindentation test on FG has been simulated by means of Ansys LS-Dyna. The main goal was to assess the material models already available in the software that could be suitable for the simulation of Sigraflex® under static loading and unloading. As described in the Introduction section, the proton beam impact in figure 1.4 generates a multi-axial stress state that may involve a large volume underneath the surface. The standard deviation of the spatial beam distribution is $250\mu m^2$ in width, which means that an area slightly bigger than that shown in figure 3.21 is being heated up instantaneously. Since the largest pores of the size distribution were found to be in the order of magnitude of $1\mu m$, these are much smaller than the heated volume and hence we can consider the response of the material at the macro-scale as the one relevant for the mechanical part of the beam impact problem. For the thermal part instead, the phenomena occurring at the meso-structure scale, such as the interaction between trapped gaseous species and unfolding of micro-sheets, are probably more relevant and would request a micromechanical model for a complete understanding.
The nanoindentation is seen as the simplest way to induce a multi-axial stress state into the material, especially due to the technical problems that arise when dealing with the fragility of the material during most types of testing setup. It has been already clarified in section 3.7.4 by applying the Delafargue and Ulm formula that the nanoindentation curves of Sigraflex® can be potentially interpreted as the macro-scale response of the material and this section can be considered as a confirmation a posteriori of this observation.

4.6.2 Overview of suitable material models in LS-Dyna

Based on the experimental observations pictured so far, a list of suitable material models for FG modeling is collected in table 4.4. The most straightforward ma-

Names	Comments
MAT_02_ORTHOELASTIC	Orthotropic elastic. The implementation depends on the type of elements used.
MAT_26_HONEYCOMB	Orthotropic: it needs six input curves σ_y - $\varepsilon_{v,pl}$. A nonlinear elastoplastic behavior can be defined separately for all normal and shear stresses, which are fully uncoupled. Elastic unloading based on tangent slope of last loading point.
MAT_57_LOW DENSITY_FOAM	Isotropic hyperelastic with hysteresis upon unloading governed by one parameter. The behavior under uniaxial loading does not significantly couple in the transverse directions.
MAT_63_CRUSHABLE_FOAM (MODEL = 1)	the behavior is the same as default implementation of Abaqus crushable foam. Elliptical yield surface in pressure-deviatoric stress space and independent definitions of elastic and plastic Poisson's ratio. Isotropic. Elastic unloading.
MAT_75_BILKHU/DUBUOIS_FOAM	Yield function and plastic flow equivalent to MAT_154 if Plastic poisson = 0. Triaxial tests are needed because the pressure for plastic yielding as a function of volumetric strain is given in input. Isotropic.
MAT_83_FU-CHANG	Isotropic hyperelastic with hysteretic unloading governed by one parameter
MAT_126_MODIFIED_HONEYCOMB	Advanced version of MAT_26.
MAT_142_TRANSVERSELY_ISOTROPIC_FOAM	Modification of MAT_26. The stress-strain curves are input separately and the stress response is fully uncoupled. It solves the issue of MAT_26 related to the overestimation of off-axis response.
MAT_154_DESHPANDE_FLECK	Elliptical yield surface such as MAT_63, but with concavity of hardening only directed upward.
MAT_05_SOIL_AND_FOAM	For soil, concrete and crushable foams. Isotropic. It needs pressure-volumetric strain input curve. Similar to Drucker-Prager/Cap model in Abaqus.
MAT_25_GEOLOGICAL_CAP_MODEL	Several material parameters that need to be calibrated by experiments. Mainly for concrete and soil.

Table 4.4: List of suitable material models in LS-Dyna.

terial model suitable for FG modeling in LS-Dyna is MAT_02 which is orthotropic elastic. This may serve as a test material model to check the validity of the input elastic parameters for other more complex orthotropic models and will be better commented in section 4.6.4.
MAT_26, MAT_126 and MAT_142 seem to have similar implementations. All of them have the characteristic of uncoupled uniaxial response which is desired to model the low plastic Poisson's ratio typical of crushable foams. MAT_57, MAT_63, MAT_75 and MAT_83 are all potentially suitable to reproduce the nonlinear behavior shown by FG under uniaxial compression, but either they are isotropic or hyperelastic and hence not capable to represent the correct unloading behavior.
MAT_154 has a particular hardening law that would not allow the change in curvature shown by the FG experimental curve.
MAT_05 and MAT_25 were included in this list as the simplest models to represent concrete-like behavior. In particular, the advantage of cap models over other

models such as the standard Drucker-Prager and Mohr-Coulomb is the ability to model plastic compaction, but the calibration involve several parameters that must be found by means of multi-axial tests, difficult to perform on FG sheets.

4.6.3 Geometry and boundary conditions

A 3D FE model was built Ansys APDL so to parametrize the geometry dimensions and the mesh parameters. The geometry of the volume is one-sixth of a cylinder with radius $r = 200$ µm and height $h_s = r$. Since the maximum indentation depth h_{max} imposed to the indenter tip is 2 µm, the conditions for a *converged* geometry are fulfilled [130]:

$$\frac{r}{h_s} \geq 1 \qquad\qquad \frac{h_s}{h_{max}} \geq 100.$$

The indenter was modeled as the Berkovich tip shown previously in figure 3.22a. Two tip radii were chosen to be compared, since this quantity is well-known to affect the loading response of elastic-plastic materials [131]. The values were 0 µm, to simulate the ideal case of sharp tip, and 1 µm (figure 4.9b), since it is the closest measurement available for the real tip used in the experiments [97]. The simulations were run by using both implicit and explicit solvers. In the second case, the kinetic-to-internal energy ratio were kept smaller than 5% so as to perform quasi-static analyses, as well as the hourglass-to-internal energy ratio when reduced elements were used.
The indented volume was meshed by hexahedral elements with progressively smaller sizes. The smallest elements were placed near the tip and were varied from 30 to 150 nm (figure 4.9c). The largest element sizes far from the indenter tip were approximately 100 times larger than the smallest elements. The indenter with tip radius equal to 0 µm was also meshed with hexahedrons, while the indenter with finite tip radius was meshed with tetrahedrons to better capture the curvature.
The displacement of the indenter was imposed as a rigid body motion (figure 4.9b) with a constant displacement rate up to a maximum value, followed by a holding time and unloading. The boundary conditions were applied to the volume as in figure 4.9d. To constrain the nodes on the lateral surface rotated by 60° around the direction 3, an additional reference was defined so to bound the nodes to move only on the plane $1^* - 2^*$. The contact force along the displacement direction 3 was taken as output and was multiplied by six so to obtain the final value to compare with the experimental curves.
The contact formulation used was the surface-to-surface mortar type for both the implicit and explicit solver. Although not common for the second solver, it was found to be the best option to minimize the penetration. Element formulations ELFORM = -1, -2 were mainly used in order to avoid hourglass problems and improve the accuracy of the results. The maximum relative penetrations were

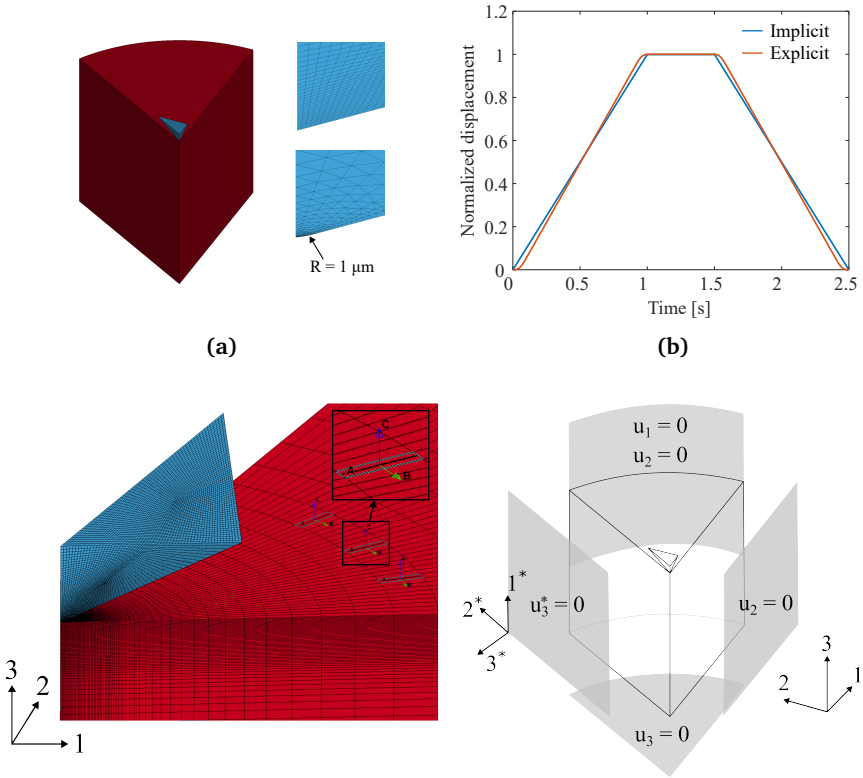

Figure 4.9: (a) 3D FE nanoindentation model geometry together with the indenter tips with radii equal to 0 µm and 1 µm. (b) The normalized displacement imposed during the simulation to the rigid indenter. (c) Detail of mesh refinement near to the tip. (d) Boundary conditions applied to the indented volume.

checked to be always below 10 nm so to give a negligible contribution to the final response.
Finally, when orthotropic material models were used, the initial material axis were oriented so that the c material axis (corresponding to E_{33}) is coincident with the indenter displacement direction as in figure 4.9d.
For comparison purposes, mostly related to the testing of different implementation of the elastic material models in LS-Dyna, an equivalent axisymmetric 2D model was also employed (figure 4.10). This geometry should be in principle closer to the Sneddon solution. The indenter was a single rigid shell with 70.3° included angle in order to have the same contact area of a pyramidal Berkovich. The element adopted were axisymmetric quadrilateral shells (ELFORM = 15) with the y axis being the symmetry axis. When orthotropic material properties were used, the material c axis was taken as normal to the shell elements plane and the b axis was chosen as the weakest material direction (figure 4.10b).

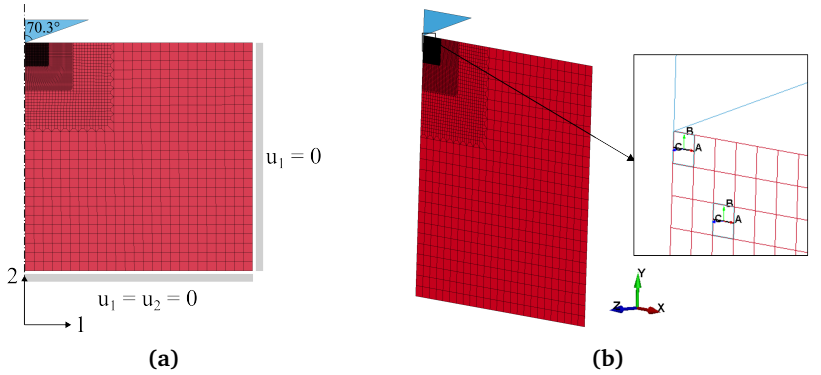

Figure 4.10: (a) 2D FE nanoindentation model together with the applied boundary conditions and (b) material directions applied to the elements, different from the 3D case.

4.6.4 Elastic simulations

At first, the simulations were run with MAT_01_ELASTIC, i.e. linear isotropic elastic properties, for the indented volume. The aim was to validate the model, the accuracy of the contact and the relative penetrations.
The material properties chosen were arbitrary i.e., $E = 500$ MPa and $\nu = 0.3$, while the indenter was given rigid body properties with realistic elastic parameters for contact treatment i.e., $E = 210$ GPa and $\nu = 0.3$.
The results are plotted in figure 4.11a together with the analytical solution from Sneddon obtained with the isotropic indentation modulus $\frac{E}{1-\nu^2}$. As expected, the 3D simulation with MAT_01 overestimates the Sneddon analytical solution mainly due to the difference in shape between the conical geometry and the Berkovich pyramidal shape, and the radial displacement, both not included in the Sneddon

solution but captured by the FE simulations. Many authors in literature have proposed simple coefficients to correct this discrepancy (see e.g. Hay et al. [132]), practically used to divide either the FE load-displacement curve or the unloading stiffness in case of elasto-plastic materials in order to obtain the correct indentation modulus and the underlying elastic properties.
The correction factor $\beta = 1.034$ already introduced in section 3.7.4 is among the most used coefficients for the correction of the difference in shape, while for the radial displacement Hay et al. proposed the coefficient γ as function of the equivalent indenter angle (70.3° for Berkovich indenter) and Poisson's ratio of the material. For example, when $\nu = 0.3$, then it outputs $\gamma = 1.067$. However, the corrective coefficients will not be used here since the main goal is to match real experimental curve by using a FE model that reproduces the real indenter shape and boundary conditions.
The real elastic properties of Sigraflex® are however transversely isotropic and therefore MAT_02_ORTHOTROPIC_ELASTIC model is better suited to get closer to the real behavior. This material model was first given isotropic elastic properties and compared to the Sneddon solution again in figure 4.11a. Since MAT_02 is implemented differently on LS-Dyna depending on both the type of solver (linear or non-linear) and the type of element (shells and solids)[4], it was also decided to assess the differences with an equivalent 2D axisymmetric model that employ shell elements (axisymmetric formulation).
Using MAT_01 in the 2D model with the same elastic parameters as for the 3D model gave results basically equal to the Sneddon solution, net of the neglected radial displacements. And, as expected, the same result is obtained if MAT_02 is used with the same isotropic elastic parameters as for MAT_01. The corresponding Von Mises stress fields for MAT_01 simulations for 2D and 3D simulations appear very similar and radially distributed beneath the indenter tip as shown in figure 4.11b.
However, if MAT_02 is used in the 3D model with the same isotropic elastic parameter of MAT_01, the load-displacement curve obtained is very different from that of MAT_01 for both the 2D and 3D model. This difference is visible for both the explicit and implicit non-linear solvers, whereas switching to the implicit linear solver gives the expected result. In the case of shell elements indeed, the linear behavior is retained even when large deformation are accounted for, while for solid elements the linear solver is needed to make the material behaving linearly at large deformation. This otherwise corresponds to the hyperelastic St. Venant-Kirchoff model.
This can be observed even more clearly also when plugging the orthotropic elastic properties of table 4.3 into MAT_02 as shown in figure 4.11c. In this case the force-displacement FE curves are compared with the Sneddon solution obtained with the Delafargue and Ulm orthotropic indentation modulus and again switching to the linear solver gives the wanted result. It should be also noticed that there is a big difference between the explicit and implicit solvers, probably due to the latter

[4] see LS-Dyna Theory Manual 06/08/22 (r:14765) - section 22.2

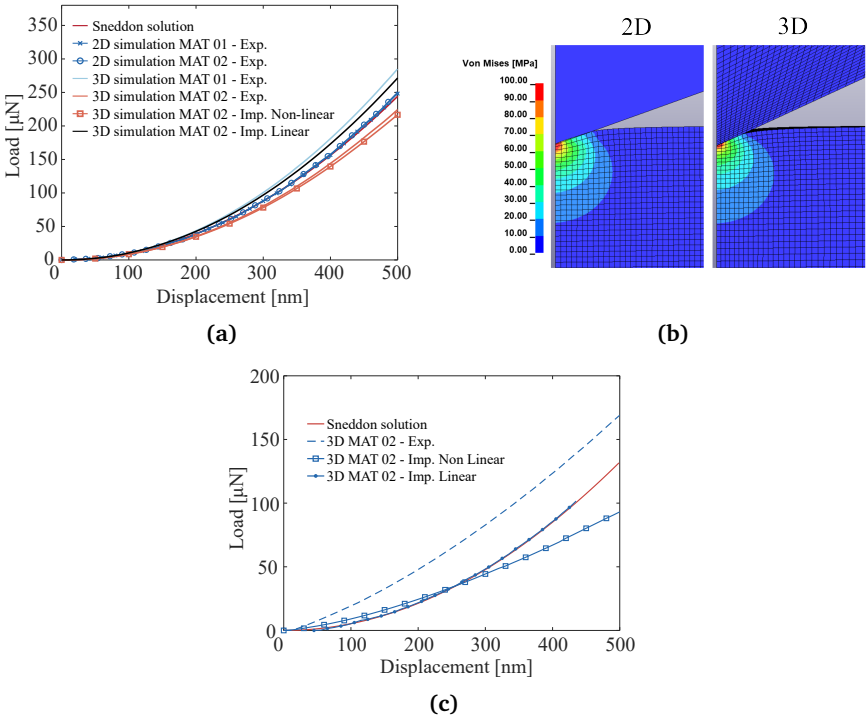

Figure 4.11: (a) Simulations with isotropic elastic material properties. MAT_01 and MAT_02 are compared with the same elastic properties in input. (b) 2D nanoindentation FE model with axisymmetric shells and comparison of Von Mises stress fields (MPa) for both 2D and 3D isotropic elastic simulations (MAT_01). (c) 3D nanoindentation FE model: validation with MAT_02 and different FE solvers

being more stable when the material embodies such a large ratio between E_{11} and E_{33}.
It is therefore concluded that the 2D approach should be preferred if the model needs to be validated by comparison with the Sneddon solution. Alternatively, the 3D model should be run by switching to the linear implicit solver which is however not the best option when non-linearities not derived from the material are present in the model.

4.6.5 Mesh sensitivity and tip radius effect

In the case considered here, large deformations and hence high mesh distortions are expected beneath the tip and thus a sensitivity analysis was performed by changing the element sizes from 50 to 150 nm.
The material model chosen was MAT_24 (piecewise linear plasticitiy model) that has isotropic elastic-isotropic plastic behavior. The material properties chosen in

this case were: $E = 500$ MPa, $\nu = 0.3$, $\sigma_y = 0.1$ MPa and $E_{tan} = 0.001$ MPa. The tangent modulus E_{tan} was given a value close to zero so to have an elastic-perfectly plastic material. At the same time, the effects of having a large tip radius equal to 1 µm instead of a sharp vertex were assessed.

The resulting force-displacement curves are shown in figure 4.12a. In the low

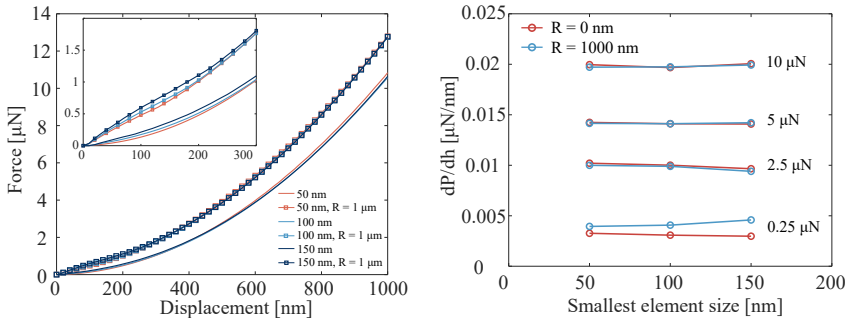

Figure 4.12: (a) Force-displacement curve from elastic-plastic simulations for different mesh size near the tip and different tip radius. (b) Slope of the force-displacement curves evaluated at four different force levels.

displacements part, the finest mesh reproduced better the power-law-like shape of a perfect shallow indenter while at higher displacements the difference in the curve slope was negligible. The same occurred for the finite radius model, which however shows a much higher force for the same displacement. This is expected because of the different contact area function which is larger since the beginning and requests a larger external force to produce the same displacement.

The slope of the force-displacement curves was evaluated at four different force values and plotted in figure 4.12b. It is observed that above certain values of the load (in this case higher than 5 µN) the slopes never differ more than 5% one from each other regardless of the mesh size and the effect of the tip radius vanishes.

It is therefore important to have a mesh size that is very fine if the goal is to reproduce reliably the shape of the low displacement region, while coarser mesh are also acceptable if the goal is to investigate large displacements. The blunt radius affects the loading curve shape only when the maximum force is sufficiently low, but shifts the whole curve towards left also at higher force values.

4.6.6 MAT 142: Transversely isotropic crushable foam

Definition of the input quantities

Based on the observations reported in the previous sections, a 3D FE nanoindentation model was simulated by means of the implicit non-linear solver with mesh size at the tip equal to 150 nm.

The material model chosen among the ones listed in section 4.6.2, is MAT_142 transversely isotropic crushable foam, currently only implemented for solid elements[5].
This material was developed by Hirth, Du Buois and Weimar [133] to model transversely anisotropic crushable foams. During their analysis, they observed that, until then, the only orthotropic models for low density foams with zero Poisson effect were MAT_26_HONEYCOMB and MAT_126_MODIFIED_HONEYCOMB.
However, the first showed an issue on the overestimation of the off-axis strength due to the full uncoupling of each stress component with its own yield strength, while MAT_142 represents an adjusted version thereof. MAT_126 may represent a good alternative to MAT_142, but it is left for future works to test and compare with the results of MAT_142 reported here.
MAT_142 is transversely anisotropic both in the elastic and plastic behavior and it is characterized by a yield surface that is an adaptation of the Tsai-Wu failure criterion. The surface hardens or softens as function of the volumetric strain $\varepsilon_v = 1 - \frac{V}{V_0}$, here considered as equal to the axial strain $\varepsilon_v = \varepsilon$ due to the low transversal deformation observed in the in-plane and out-of-plane directions. The requested inputs for this model are reported in table 4.5. Although the problem under investigation concerns the microscale, here the inputs used are borrowed from experimental data taken at the macroscale. This constitutes a strong assumption whose validity can only be assessed a posteriori.
For the load curve I_{11} shown in figure 4.13a, the mechanical model 4.7 proposed in section 4.4 was used for the negative volumetric strain part in order to have a smooth input curve and a realistic extrapolation at high volumetric strains. However, since the material model requested the engineering volumetric strain, the fitting already shown in section 4.4 was adapted to the engineering stress-strain curves. The new parameters were:

$$E = 41.91 \text{ MPa} \quad H = 0.0009359 \text{ MPa} \quad K = 166.2 \text{ MPa}^2 \quad n = 14.19 \qquad (4.14)$$

Since it was also of interest to vary the elastic contribution in the out-of-plane direction, other two curves were given in input. These were simply obtained by keeping the known fitting parameters in 4.14 except for the elastic modulus, which was instead doubled and tripled i.e., $E_{33} = 80$ MPa and $E_{33} = 120$ MPa. The curves obtained are shown in figure 4.13a. For the positive volumetric strain part, a very low constant stress value was given so to have a sort of elastic-perfectly plastic material under tensile load. The value of asymptotic stress was set to 0.3 MPa. Concerning I_{22} (figure 4.13b), the fitting 3.1 with the values $A = 1/2290$ MPa^{-1} and $B = 130.78 \cdot 10^{-6}$ MPa^{-2}, already reported in section 3.9, was used to construct the curve for both the positive and negative domains of the volumetric strain. To test also the potential differences between the tension and compression behavior discussed in section 4.5.3, the compression part was also scaled in order

[5]The author tested different element formulations, including shell elements, and observed that only hexahedral solid elements gave meaningful results.

E_{11}	Elastic modulus in the out-of-plane direction	40 MPa
E_{22}	Elastic modulus in the in-plane direction	2290 MPa
E_{12}	Shear modulus in the longitudinal plane 1 - 2	646.56 MPa
E_{23}	Shear modulus in the transversal plane 2 - 3	1145 MPa
G	Shear modulus for contact	1145 MPa
K	Bulk modulus for contact	190 MPa*
I_{11}	Load curve for nominal axial stress as a function of volumetric strain	Figure 4.13b
I_{22}	Load curve for nominal transverse stresses as a function of volumetric strain ($I_{22} = I_{33}$)	Figure 4.13a
I_{12}	Load curve for shear stress component 12 and 31 as a function of volumetric strain ($I_{12} = I_{31}$)	Figure 4.13d
I_{23}	Load curve for shear stress component 23 as a function of volumetric strain	Figure 4.13d
I_{AA}	Load curve for nominal off-axis stress as a function of volumetric strain	Not assigned
σ_y	Yield strength (in all the directions)	0.001 MPa
μ	Damping coefficient for tensor viscosity	0.05

*This was estimated according to Summerscales et al. [126].

Table 4.5: Inputs for MAT_142. It must be noticed that the material axes for MAT_142 are different from the material axes used for MAT_02. In MAT_142, the out-of-plane axis corresponding to the weak direction was along direction 1 instead of 3 (compare with figure 4.9c).

to have the value of the initial slope in the negative strain domain equal to a typical elastic modulus value of polycrystalline graphite (see e.g. [52]).
Due to the assumption of transverse isotropy, the in-plane shear modulus is dependent on the in-plane tensile modulus, but the entire shear stress-shear strain curve is not known from the experiments. This was assumed as having a linear behavior with slope correspondent to the elastic in-plane shear modulus $G_{12} = 1145$ MPa. Consequently, since the in-plane compression curve was scaled for testing purposes, also the corresponding shear in-plane curve had to be changed, and a mean value between the tension and compression in-plane moduli was assigned per each case 4.13c.
The out-of-plane shear curve curve in figure 4.13d was also not known from the experiments and was likewise assumed as linear with slope equal to the initial shear modulus $G_{23} = 646.52$ MPa. Two additional values of the slope were tested, the first corresponding to the slope of in-plane shear curve and the second corresponding to the in-plane tensile modulus.
Finally, all the curves were let to start from $\sigma_y = 0.001$ MPa in order to simulate the vanishing elastic domain.
Not clear indications were given in the user manual about the unloading behavior but this was directly observed by simulations of single solid elements and was found to be linear elastic with the unloading moduli corresponding to the initial elastic moduli.
The simulations were run by changing only one quantity at a time while keeping

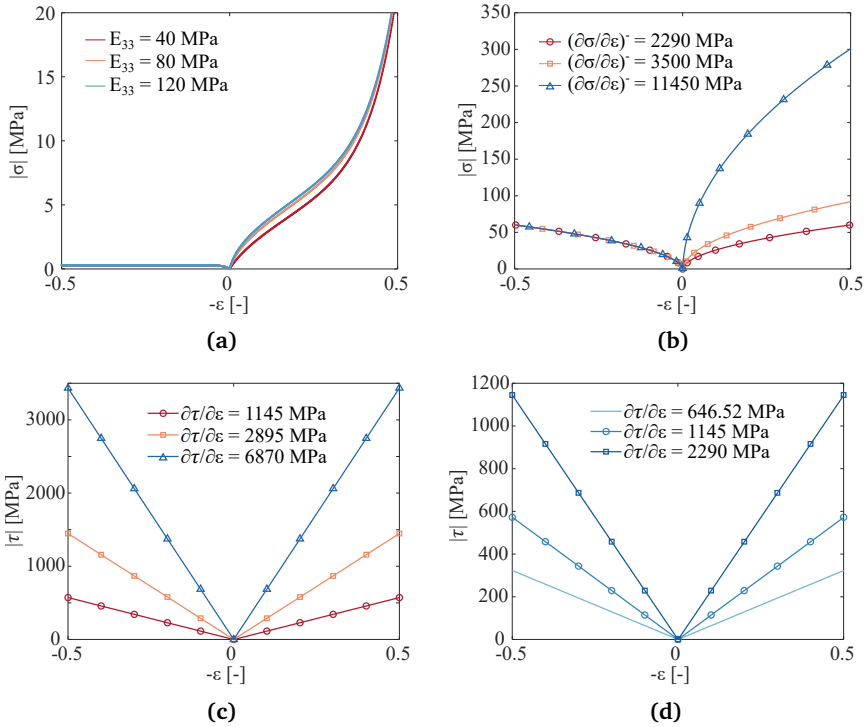

Figure 4.13: MAT_142 input curves: (a) I_{11}, (b) I_{22}, (c) I_{23} and (d) I_{12}. See also table 4.5.

the others equal to the basic case: this corresponds to case where the lowest value of the elastic moduli is considered in each direction as well as $R = 0$ µm. The tip radius was increased up to 5 µin this session to exaggerate the effects observed in section 4.6.5.

Results

The resulting load-displacement curves are displayed in figure 4.14a to 4.14d. With respect to the basic case, it can be observed that:

- increasing the slope G_{12} of the out-of-plane shear curve I_{12} has a very low effect on the maximum load and on the displacement recovered after unloading (figure 4.14a),
- increasing the in-plane compression initial modulus $\left(\frac{\partial \sigma}{\partial \varepsilon}\right)^{-}$ does not lead to any sensitive effects on the maximum load (figure 4.14b) except for the highest modulus case. This deviated slightly and showed a much larger non-recovered displacement. This case is however extreme and not realistic because of the unloading being fully elastic while the underlying elastic prop-

erties not representing to a stable material (violation of the stability conditions discussed in section 4.5.2). The loading part instead develops entirely in the elasto-plastic domain of the material where the stability conditions are not required anymore,

- increasing the tip radius from 0 up to 5 μm leads to a noticeable increase in the maximum load (figure 4.14c). The slope of the unloading curve together with the recovered deformation are instead untouched. This is in line with what is usually observed in nanoindentation tests where the unloading is assumed fully elastic and the elastic properties extracted are not dependent on the tip radius [131],
- increasing E_{33} elastic modulus has the major effect on the loading curve (figure 4.14d). Also the slope after the load reversal is strongly increased while the permanent deformation is basically the same for the three cases.

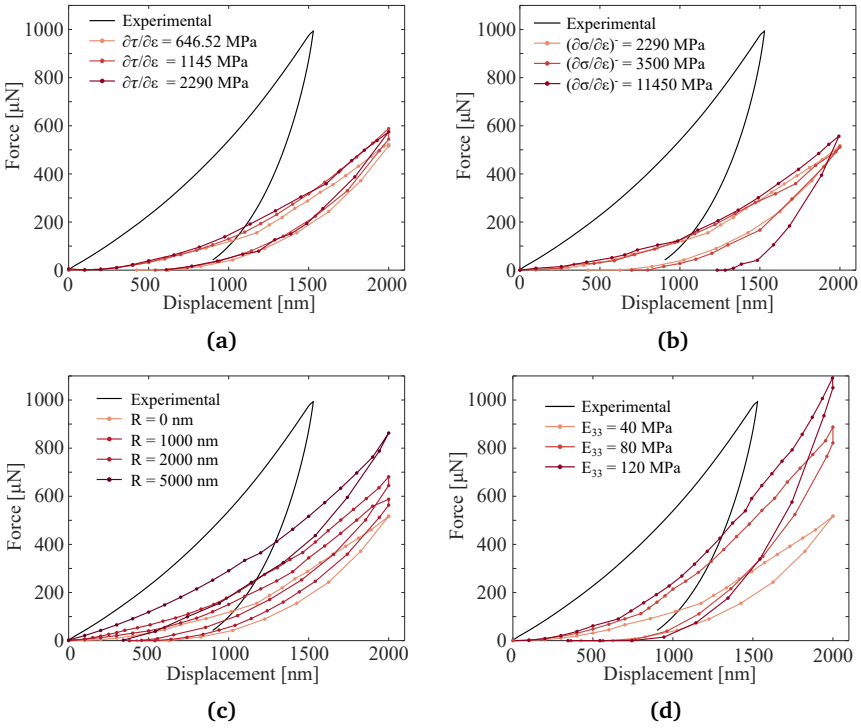

Figure 4.14: Numerical force-displacement curves from MAT_142 simulations: (a) variation of the out-of-plane shear curve I_{12}, (b) variation of the in-plane curve I_{11}, (c) variation of the tip radius, (d) variation of the out-of-plane curve I_{33}.

Discussion

The first challenge encountered while running these simulations was the strong difference between the in-plane and out-of-plane stiffness of the elements being compressed under the tip. The optimal mesh near the tip was found after several iterations and was constituted of elements with aspect ratio between the out-of-plane and in-plane sizes higher than one, so that they could deform largely in the out-of-plane direction while avoiding volumetric locking and negative volumes.
Observing 4.15, it can be seen that the equivalent stress field extends mainly along the in-plane direction with respect to an equivalent isotropic case (compare with figure 4.11b) and the perturbation follows the stiffest material axes while remaining narrow along the weak direction axis. After the unloading, the plastic imprint is well visible and follows a convex surface profile probably resulted from the predominant recovery of the radial deformations.
Although the nanoindentation problem originates a 3D stress state that involves

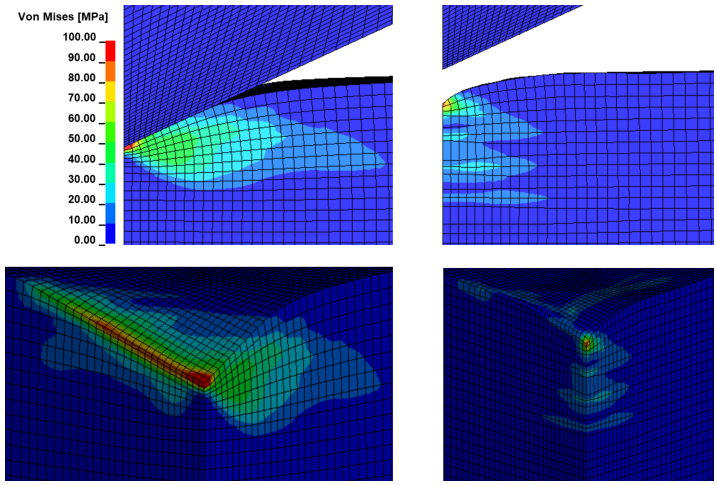

Figure 4.15: Von mises stress distribution beneath the indenter tip. On the left side, front and trimetric view of the simulation when tip is pushed down to 1 µm. On the right side, front and trimetric view of the simulation after complete unloading.

also the contributions from the in-plane directions, the most influencing material quantity was the out-of-plane elastic modulus E_{33}. To assess more in depth this contribution, the slope of the loading curve at different loads was measured by evaluating the derivative of a polynomial fitting to both the simulation curves and to the experimental curve (figure 4.16a). The experimental curve slope lays in between the slopes corresponding to $E_{33} = 80$ MPa and $E_{33} = 120$ MPa. This means that either the real material is denser and stiffer near the surface, as already discussed in section 3.2, or that it undergoes densification due to pore closures while being indented. According to figure 3.19a, the modulus should increase ex-

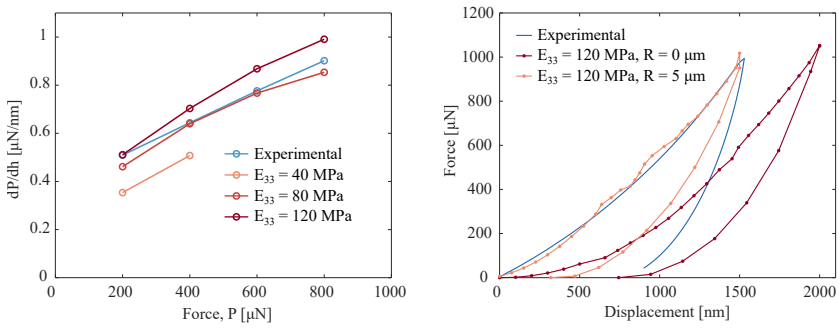

Figure 4.16: (a) Slope of the force-displacement curves reported in figure 4.14d at four different force levels. (b) Effect of 5 μm tip radius and $E_{33} = 120$ MPa.

ponentially as function of the relative density. For example, an increase from 30 to 60 MPa would correspond to a relative density increase from 0.44 to 0.6. It is therefore reasonable that, if the volume under the indenter densifies up to 0.7 or 0.8, the modulus could increase up to 120 MPa.
However, the gap that is missing to match the experimental behavior is still large. Although the slopes of the simulation and experimental curves are similar, a big shift backward in the displacement axis would be needed to improve the matching (see figure 4.16b). This could be attributed to an effect of the tip radius, as shown in section 4.6.5, which would act exactly as a shift along this axis. Indeed, keeping $E_{33} = 120$ MPa, and increasing the radius up to the unrealistic value of 5 μm, would actually lead a very good match to the loading path. Measurements of the real tip radius are unfortunately not available but this is unlikely to deviate so much from R = 1 μm inferred in [97]. Therefore, other material parameters related to the local porous microstructure may have played a similar role and may have originated a larger contact area since the early beginning of the indentation. The unloading path remains untouched with respect to the case for R = 0 μm. This deviates from the shape of the experimental curve but shows a similar ratio between the residual and maximum deformations. The underestimation of the unloading slope also defined contact stiffness can be ascribed to even further stiffening of the real material at peak load or to a different equivalent angle of the plastic imprint with respect to the one obtained in the simulation.
In summary, MAT_142 equipped with stress-strain curves borrowed from macroscale tests can be considered as a good initial guess for FG modeling and mechanical properties investigation. Further experiments such as macro-indentations at different length scale and with different shapes of the indenter tip could be a useful resource to proceed with this investigation and get further refinement of the material model parameters without stepping too far from the observations gathered in this work. Other material models such as MAT_126 may also be tested and compared with MAT_142.

4.7 Challenges and potentialities of a micromechanical model

The goal of a micromechanical model would be to obtain homogenized properties that are better estimates than those found in this work by macro-scale approaches or that could be used for example for FE multi-scale simulations.
A fundamental parameter for the design of a micromechanical model is the size of the representative volume element (RVE) for the microstructure. This should be large enough to reproduce the global mechanical response but as small as possible to reduce the simulation time. Since the nanoindentation simulations could somehow reflect the behavior of Sigraflex® at macro-scale, it is likely that the volume of material as large as the one compressed under the indenter tip is representative of FG mechanical response.
Observing the FE simulations, this may be roughly represented by a volume with height from 10 to 15 μm in the out-of-plane direction and widths from 20 to 30 μm in the in-plane directions. The image analysis in section 3.2 was performed on pictures of the cross-section area having dimensions in the same order of magnitude (40×50 μm^2), and gave as estimated porosity a value around 0.15, much smaller than the global porosity that is around 0.5. On one side, this does not support the previous argument about the RVE size, while on the other side it could be simply due to the difference between the 2D and 3D pores distributions that is not captured by image analysis. Therefore, different techniques capable to both detect pore sizes as low as ∼10 nm and capture three dimensional features would be needed, such as *slice-and-view* FIB-SEM scanning [134] or computed tomography with higher resolution.
In this work, a simple 2D micromechanical model based on the FIB-SEM image analysis was attempted to assess the benefits and challenges of a potential 3D micromechanical model to be developed in future works. A possible geometry for a representative area element was rendered by post-processing the FIB-SEM images of section 3.2; the model shown in figure 4.17a was constructed by means of conversion from pixels to coordinate performed in MATLAB® and by exploiting the boolean geometry capabilities of Ansys APDL®. The material was assumed as isotropic elastic-perfectly plastic (MAT_24) with elastic properties in the order of magnitude of those of polycrystalline graphite: $E = 10$ GPa and $\nu = 0.3$. The yield strength was arbitrarily set to 1 MPa. The boundary conditions included plain strain in the shell elements plane and static uniaxial compression applied in the out-of-plane direction. A FE model of this type could easily run in a short solution time but carried so many uncertainties that the solution at this stage could not be considered as reliable. Due to time constraints related to the project at the time of the model development, it was decided to prioritize the macro-scale approach while leaving the refinement of the micromechanical model for future work. A short discussion is reported anyway for completeness.
A first observation is that a large number of small pores could not be well reproduced in the geometry due to the insufficient accuracy of the pixel-coordinate

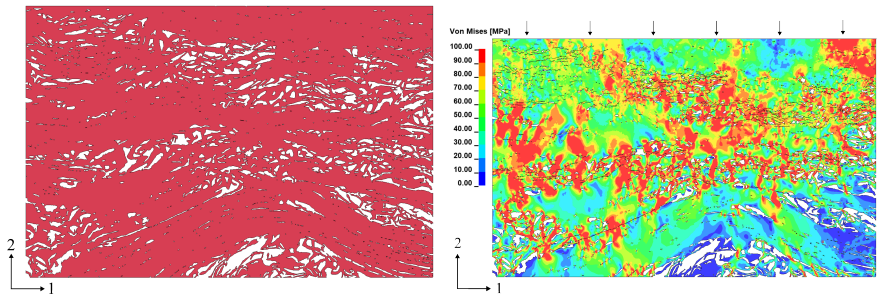

(a) **(b)**

Figure 4.17: (a) Geometry of 2D micromechanical model based on image analysis of FIB-SEM investigation. (b) Von Mises stress field after compression along the out-of-plane direction.

conversion. Most of them corresponded to less than three pixels and their contours were uncertain. The limitations of this type of image analysis are thus related to the possibility of capturing with the same amount of pixels the large and the tiny pores randomly mixed together inside the material. Many more pictures should be taken at different magnifications and analyzed separately so that, after re-scaling and composition, the representative element geometry could be reproduced more accurately.

The geometry as it appears in figure 4.17a corresponds to a material that is porous and continuously connected such as a disordered foam. FG is instead the result of a crumpling process that put the micro-sheets in contact without creating new linking forces[6]. Many regions that appear as continuously connected contain instead non visible contact surfaces where none or weak links exist. The modeling of all these contacts with any FE software would probably lead to an enormous increase in the simulation time but would include the fundamental structural difference with a continuous foam microstructure.

Finally, it should be considered that the micro-sheets are anisotropic and that this property is probably not negligible for the correct simulation of the homogenized mechanical properties. This should be implemented in any FE mesher by orienting the initial material directions of each element along the actual crystalline axes following the micro-sheets mid-surface curvature (in a similar way as shown in figure 4.1). In this way, the material properties of graphite single crystals could also be used and this basically constitutes the main advantage of such a micromechanical model whose role would be to only replicate the contribution of the structural deformation.

A solution for the correct reproduction of the structure would be to first generate the geometry in the uncompressed configuration e.g., a single expanded worm or a single honeycomb cell with carbon walls, and then compress it by leaving the

[6]Actually, in folding of graphene sheets, new Van der Waals forces may be recreated at the contacts and act as stabilizers for the folded configuration [118]

folds and the creases to generate freely according the random crumpling dynamics. This is somehow similar to what has been done in many crumpling materials investigation where techniques such as molecular dynamics or discrete elements were employed to simulate the crumpling mechanism of single elastic and elastoplastic thin sheets [117, 135]. This procedure would serve to the only microstructure generation, which could now be tested under the desired load conditions.
With the recent advances in terms of computing capabilities, it is not excluded that also FE would succeed in solving similar problems in reasonable simulation times. In this case, to know the size of a representative element would be crucial in speeding up the solution. Many random configurations of two interacting micro-sheets could be simulated under compression loading so to obtain several crumpled volumes with geometrical properties that can be correlated to the mechanical properties, perhaps in a statistical way, and compared with experimental data. Experiments such as in-situ compression tests on the same line as the the ones shown in section 3.5 would serve as model validation.

5. Conclusions

5.1 Concluding remarks

An extensive characterization of Sigraflex® ($\rho = 1$ g/cm^3) and FG have been presented in this thesis.
A comprehensive review of the known FG properties was first presented. In particular, the experimental observation and data from microstructural investigations were collected and presented. The latter was described as strongly inhomegeneous and anisotropic, with pores having sizes ranging from a few nanometers up to a few micrometers, and shapes mainly flatten along the in-plane directions. The micro-sheets constituted the basic structural elements and their crumpled configurations were considered as responsible of the aggregation forces developed during the compaction process.
The mechanical properties were collected and compared at different densities. The density was observed to be the main design parameters for FG sheets as affecting both the sheet stiffness and the ultimate strength. The thermal properties such as the heat capacity and the thermal expansion were found to be quite similar to those of crystalline graphite given the high content of carbon (> 98 %), while the conductivity was comparable to that of pyrolytic and polycrystalline graphite.
The review outlined a consistent lack of quantitative data obtained by direct investigation of the microstructure, such as image analysis, especially at the density of 1 g/cm^3. This aspect motivated the second goal of this work established in the Introduction i.e., to find an experimental technique that could allow for the quantitative evaluation of the microstructure. The FIB-SEM investigation performed during the experimental campaign was applied to FG for the first time, and was recognized as a successful technique in this sense, finally allowing for the measurement of the micro-sheet thickness, the 2D pores' sizes and shapes. The micro-sheets were clearly visible and they were estimated to be made of 120 - 360 carbon basal planes.
Moreover, some portions of the milled section (100 × 150 µm) that were the least affected by curtaining were chosen for image post-processing in 2D. The microstructure was found to be made of aligned and misaligned regions: the first ones were composed of bundles of well-oriented micro-sheets surrounded by thin and elongated pores. The second ones had bigger pores ($R_{eq} = 0.13$ µm) and mainly

contributed to 85% of the overall porosity. In general, all the pores were found to have an average 2D aspect ratio equal to 0.384, as it is expected after a compacting production process.
Subsequently, tensile tests were performed on Sigraflex® in the in-plane direction both in-situ and at the macro-scale. The initial tangent modulus was found to be 2290 MPa. Post-mortem fractographies performed by SEM on tensile-fractured specimens highlighted that the interlocked particles inside the material were mainly torn apart near the boundaries. However, it was difficult to define whether the micro-sheets or the interlocking arrangement were the weakest link.
The stress-strain curve observed in the out-of-plane compression was observed to be extremely different from the in-plane tensile curve. This showed three stages of deformation: the initial toe, the transition and the densification. The deformation mechanism behind the initial toe was attributed to a structural component of the strain, in analogy to uniaxial compression tests of crumpled and entangled material. The transition region was markedly different from a typical flat plateau usually observed in foam compression and was attributed to a predominance of graphite-like dislocation mechanism.
During cyclic loading, FG showed discrete memory behavior similar to rock and soils, nearly zero yield strength typical of graphitic material and relatively large areas of the hysteresis loops. The initial tangent slope of each cycle was observed to increase from 30 to 60 MPa while the relative density was increased from 0.45 to 0.6.
Finally, the ratio of the residual deformations was estimated to have constant value (0.083) along the strain domain tested. This could be also considered as a rough approximation for the plastic Poisson's ratio.
In summary, FG behavior could be described at three different scales of length: at the micro-scale, hundreds of carbon basal planes constituted the microstructure of a single micro-sheet and the deformation mechanism was ascribed to the crystalline dislocations. At the meso-scale, the micro-sheets arrangement resulted from severe crumpling after the compaction thank to ease of sliding of the basal planes, and deform locally in a way similar to crumpled materials. At the macro-scale, contact forces due to folds and wrinkles act likewise cohesive forces in compacted powders and keep the micro-sheets as well as the particles aggregated.
In the modeling section, a simple 1D phenomenological model was proposed to fit the experimental compression curves and to support the assumptions about the decoupling of underlying deformation mechanisms under compression i.e., one from the graphitic nature and the other from the crumpled nature. The model was also used subsequently in the implementation of the out-of-plane compression curve for the FE nanoindentation model.
From the 1D dimension, the focus was then shifted to the 3D dimensions: the five elastic parameters E_{11}, E_{33}, G_{23}, ν_{12}, ν_{23} needed to build the elasticity stiffness were found and inferred by simple assumptions based on experimental observations.

However, FG showed a non-linear behavior in both the in-plane and out-of-plane direction and the extension from 1D to 3D was found to be not straightforward. The most practical solution was to adapt a material model already implemented in the LS-Dyna materials library and in principle targeted for transversely isotropic crushable foams.
To test the accuracy of this model, a 3D FE nanoindentation model was built with the aim to reproduce the typical experimental force-displacement curve extracted from the nanoindentation tests. The six stress-strain curves requested in input were partially taken from macro-scale tests and partially assumed along the same line as the elastic parameters. The elastic modulus E_{33} was found to be most affecting quantity, and the simulations were able to predict the slope of the loading curve only when E_{33} was increased from the initial value of $E_{33} = 40$ MPa up to 120 MPa. This was attributed the a local densification of the material caused by the indentation itself. Increasing the tip radius from 0 μm to 1 μm and even up to 5 μm improved the matching, but not enough to attribute a major contribution to this parameter. The unloading path could not be reproduced, and this was probably due to a different effective angle of the plastic imprint.
Finally, the challenges related to a potential micromechanical model were discussed based on observations about an exploratory 2D micromechanical model. The computational cost of such a modeling was considered as demanding, but since, to the knowledge of the author, no constitutive material model is dedicated to the modeling of crumpled materials, the potential of a micro-mechanical model capable to give an homogenized solution would be extremely high and of interest also in different applications of crumpled materials.

5.2 Suggestions for future works

The next experimental steps may help to enlarge the knowledge about FG properties and perhaps reveal the properties that were only guessed in this work. These may include:

- In-plane compression testing of FG. The goal would be not only to extract the compression modulus (that could be done by ultra-sound techniques) but the whole stress-strain curve. An idea for the setup can be found in ASTM D695 [87]. Here, a support jig for thin specimens is recommended and, given the smoothness of FG external surfaces and the low lateral expansion expected, the approach is worth to try. It is not excluded that also flexural tests maybe of help for indirect observation of different moduli in tension and compression.
- In-plane shear tests to measure G_{12} and the shear stress-strain curve. Some possible tests configurations could be two/three rails or Iosipescu-type tests (e.g. [136]).
- Out-of-plane shear tests to measure G_{23}. This correponds to the delamina-

tion mode of deformation and can be more challenging to measure due to the fragility of the material. Some possible test options could be the double-notched specimen test described in ASTM D5379 [137] or the torsional test on a rectangular-based specimen as described in [138–140]. Other suitable tests may include dynamic tests based on sonic resonance of lamina-type specimens, for which dedicated standards on graphitic materials there exist (see e.g. ASTM C747 [141] and related).

- measurement of ν_{12}. This can be found by measuring the lateral deformation in a uniaxial tension test in the in-plane direction by Digital Image Correlation. If possible, with a similar setup proposed also for in-plane compression, ν_{12} should be measured also under in-plane compression.
- measurement of ν_{31}. This can be found by measuring the lateral deformation in a uniaxial compression test along the out-of-plane direction and measuring at the same time the lateral deformation along the in-plane direction by Digital Image Correlation. This could be done by stacking squared specimens until a cubic volume is obtained so to have a large imaged area. The main unknown is about the large deformation expected and hence the reliability of the spray pattern to capture it without being damaged.
- a substitute test to replace the nanoindentation in the modeling validation task. This can be a macro-indentation tests with the indenter tip much larger than a Berkovich tip (such as a typical hardness test). This is to make sure that no size effect is involved in the testing. Indentation tests are often employed for foam FE model validation such as in [133, 142] and may use both spherical, pyramidal or flat tip. Here a limitation would be that the sheet thickness is limited to 2 or 2.5 mm, and hence, for very deep indentations the force-displacement may be affected by the rigid floor below the specimen. But again, this could be solved by stacking two or more sheets.
- nanoindentation tests that can be a useful tool to extract FG orthotropic properties. To decouple the contributions of the elastic moduli from each direction, it is suggested to indent FG along the in-plane direction. (The same could be done for the macro-indentation test mentioned above). The limitation here can be given by the surface roughness observed after the specimen cutting with water jet machining. It is noticed however that as-provided Sigraflex® sheets shows a fine lateral surface, probably sufficient to obtain reliable force-displacement curves.
- FIB-SEM slice-and-view technique or μ-CT to reconstruct a volume of material at least as big as $50 \times 50 \times 50\ \mu m^3$,
- the thermal properties of Sigraflex® . A thermo-mechanical tests can be extremely valid to quantify the effect of a fast application of thermal load. This should be supported by adequate equipment such as a high-temperature camera, capable to measure the temperature field and the temperature gradient. The issue of specimen emissivity observed in this work may be solved by spray painting the specimen with an adequate absorbing paint that may also act as base paint for the Digital Image Correlation speckle.

Some ideas for future modeling steps are instead listed here:

- Compare MAT_126 (modified honeycomb) and MAT_142, preferably using macro-scale tests for validation, such as the last proposed in the previous list. Refine the material parameters in input with the experimental results from the previous list.
- Implement the Jones and Nelson model in a user defined subroutine and compare with the abovementioned material models upon loading conditions. To model the unloading implies that a criterion to account for plastic internal variable should be also implemented but this is non trivial and further theoretical knowledge must be developed previously. Perhaps, a modification of the Ramberg-Osgood implementation in Abaqus targeted to edit the incompressibility of the material under plastic flow may be a good starting point,
- Use the volume reconstructuted by FIB-SEM slice-and-view or μ-CT to build a micromechanical model capable to replicate the crumpled meso-structure. This can be not trivial given the large amount of contacts that may not be captured after the reconstruction.
- Improve the knowledge about crumpled materials and ensure whether the theory and the means used in the investigation of crumpled materials could be used to ease the FG modeling. For example, the excessive thermal expansion observed in the HiRadMat experiments may also be seen as a structural deformation mode, that can be explained by the crumpled meso-structure. Moreover, since crumpled materials have mechanical properties that are well-reproducible despite the chaotic microstructure, it is expected that a few basic mechanisms govern the crumpling dynamic and hence a few statistical parameters may suffice to represent a crumpled geometry. If it could be demonstrated that a FG micro-sheets behave as a crumpled sheet, a micromechanical model could be even avoided.

Bibliography

[1] L. Evans and P. Bryant, 'LHC machine,' *Journal of instrumentation*, vol. 3, no. 08, S08001, 2008.

[2] A. L. Lund, *Upgrades of the target dump externals for the large hadron collider - cern document server*, (Accesss: 2023-21-04). [Online]. Available: https://cds.cern.ch/record/2851843?ln=en.

[3] *The CERN accelerator complex, layout on 2022*, (Accessed: 10.12.2022). [Online]. Available: https://cds.cern.ch/images/CERN-GRAPHICS-2022-001-1.

[4] R. Schmidt, R. Assmann, E. Carlier, B. Dehning, R. Denz, B. Goddard, E. Holzer, V. Kain, B. Puccio, B. Todd *et al.*, 'Protection of the CERN large hadron collider,' *New Journal of Physics*, vol. 8, no. 11, p. 290, 2006.

[5] J. Wenninger, 'Machine protection and operation for LHC,' *arXiv preprint arXiv:1608.03113*, 2016.

[6] SGL Carbon, *Smart solutions in graphites & fiber composite*, (Accessed: 8.11.2022). [Online]. Available: https://www.sglcarbon.com/en.

[7] F.-X. Nuiry, M. Calviani, M. Bergeret, S. Pianese, M. Butcher, L.-M. Grec, A. Lechner, M. I. Frankl, F. L. Maciariello and T. Pichon, '3d carbon/carbon composites for beam intercepting devices at cern,' *Material Design & Processing Communications*, vol. 1, no. 1, e33, 2019.

[8] J. Heredia, A. Perillo-Marcone, F. Berto, A. Alvaro, K. Kershaw, D. Grenier, V. Rizzoglio, E. Solfiti, R. Franqueira Ximenes, F.-X. Nuiry *et al.*, 'Sigraflex® for LHC CERN Beam Dump: Summary and Perspective,' *JACoW IPAC*, vol. 2021, pp. 3571–3574, 2021.

[9] J. H. Shane, R. J. Russell and R. A. Bochman, *Flexible graphite material of expanded particles compressed together*, US Patent 3,404,061, 1968.

[10] M. P. Nemeth, 'An in-depth tutorial on constitutive equations for elastic anisotropic materials,' Tech. Rep., 2011.

[11] *Release 11.0: ANSYS CFX-Solver theory guide*, 2010.

[12] B. Gladman *et al.*, 'LS-Dyna Keyword Users' Manual,' *Livermore Software Corporation California*, 2007.

[13] A. Bertarelli, E. Berthome, V. Boccone, F. Carra, F. Cerutti, N. Charitonidis, C. Charrondiere, A. Dallocchio, P. F. Carmona, P. Francon *et al.*, 'An experiment to test advanced materials impacted by intense proton pulses at CERN HiRadMat facility,' *Nuclear Instruments and Methods in Physics Research Section B: Beam Interactions with Materials and Atoms*, vol. 308, pp. 88–99, 2013.

[14] G. Battistoni, F. Cerutti, A. Fasso, A. Ferrari, S. Muraro, J. Ranft, S. Roesler and P. Sala, 'The fluka code: Description and benchmarking,' in *AIP Conference proceedings*, American Institute of Physics, vol. 896, 2007, pp. 31–49.

[15] Mersen, *Technical guide - Papyex® flexible graphite*, (Accessed: 13.12.2022). [Online]. Available: https://www.mersen.com/sites/default/files/publications-media/6-gs-papyex-flexible-graphite-mersen.pdf.

[16] NeoGraf, *GraFoil® flexible graphite*, (Accessed: 13.12.2022). [Online]. Available: https://neograf.com/products/gaskets-sealants/grafoil-flexible-graphite.

[17] M. Cermak, 'Natural graphite sheet heat sinks for power electronics,' Ph.D. dissertation, Applied Sciences: School of Mechatronic Systems Engineering, 2020.

[18] H. Toda, K. Tsubone, K. Shimizu, K. Uesugi, A. Takeuchi, Y. Suzuki, M. Nakazawa, Y. Aoki and M. Kobayashi, 'Compression and recovery micromechanisms in flexible graphite,' *Carbon*, vol. 59, pp. 184–191, 2013. DOI: 10.1016/j.carbon.2013.03.008.

[19] M. Kobayashi, H. Toda, A. Takeuchi, K. Uesugi and Y. Suzuki, 'Three-dimensional evaluation of the compression and recovery behavior in a flexible graphite sheet by synchrotron radiation microtomography,' *Materials Characterization*, vol. 69, pp. 52–62, 2012. DOI: 10.1016/j.matchar.2012.04.008.

[20] A. Celzard, J. Mareche and G. Furdin, 'Modelling of exfoliated graphite,' *Progress in materials science*, vol. 50, no. 1, pp. 93–179, 2005.

[21] SIMULIA User Assistance 2022, *Mechanical constitutive theories*, (Accessed: 14.12.2022). [Online]. Available: https://www.3ds.com/support.

[22] E. Solfiti and F. Berto, 'Mechanical properties of flexible graphite,' *Procedia Structural Integrity*, vol. 25, pp. 420–429, 2020.

[23] E. Solfiti and F. Berto, 'A review on thermophysical properties of flexible graphite,' *Procedia Structural Integrity*, vol. 26, pp. 187–198, 2020.

[24] E. Solfiti, M. Calviani, A. Perillo-Marcone, J. Heredia, C. Torregrosa, A. Alvaro and F. Berto, 'Flexible graphite as beam dumping material in the TDE blocks of the large hadron collider,' *Procedia Structural Integrity*, vol. 28, pp. 2228–2234, 2020.

[25] E. Solfiti, D. Wan, A. Celotto, N. Solieri, P. A. Munoz, R. F. Ximenes, J. M. Heredia, C. L. T. Martin, A. P. M. F.-X. Nuiry, A. Alvaro *et al.*, 'FIB-SEM investigation and uniaxial compression of flexible graphite,' *arXiv preprint arXiv:2304.04021*, 2023.

[26] M. Dowell and R. Howard, 'Tensile and compressive properties of flexible graphite foils,' *Carbon*, vol. 24, no. 3, pp. 311–323, 1986.

[27] A. V. Ivanov, N. V. Maksimova, M. S. Manylov, A. N. Kirichenko, I. L. Kalachev, A. P. Malakho and V. V. Avdeev, 'Gas permeability of graphite foil prepared from exfoliated graphite with different microstructures,' *Journal of Materials Science*, vol. 56, no. 6, pp. 4197–4211, 2021.

[28] M. Inagaki and T. Suwa, 'Pore structure analysis of exfoliated graphite using image processing of scanning electron micrographs,' *Carbon*, vol. 39, no. 6, pp. 915–920, 2001.

[29] P.-H. Chen and D. Chung, 'Elastomeric behavior of exfoliated graphite, as shown by instrumented indentation testing,' *Carbon*, vol. 81, pp. 505–513, 2015.

[30] Y. Leng, J. Gu, W. Cao and T.-Y. Zhang, 'Influences of density and flake size on the mechanical properties of flexible graphite,' *Carbon*, vol. 36, no. 7-8, pp. 875–881, 1998.

[31] A. Yoshida, Y. Hishiyama and M. Inagaki, 'Exfoliated graphite from various intercalation compounds,' *Carbon*, vol. 29, no. 8, pp. 1227–1231, 1991.

[32] P. H. Chen and D. D. Chung, 'Viscoelastic behavior of the cell wall of exfoliated graphite,' *Carbon*, vol. 61, pp. 305–312, 2013. DOI: 10.1016/j.carbon.2013.05.009.

[33] M. Krzesińska, A. Celzard, J. F. Marêché and S. Puricelli, 'Elastic properties of anisotropic monolithic samples of compressed expanded graphite studied with ultrasounds,' *Journal of Materials Research*, vol. 16, no. 2, pp. 606–614, 2001. DOI: 10.1557/JMR.2001.0087.

[34] L. Xiao and D. Chung, 'Mechanical energy dissipation modeling of exfoliated graphite based on interfacial friction theory,' *Carbon*, vol. 108, pp. 291–302, 2016.

[35] E. A. Efimova, D. A. Syrtsova and V. V. Teplyakov, 'Gas permeability through graphite foil : The influence of physical density, membrane orientation and temperature,' *Separation and Purification Technology*, vol. 179, pp. 467–474, 2017. DOI: 10.1016/j.seppur.2017.02.023.

[36] H. Pierson, 'Handbook of Carbon, Graphite, Diamond and Fullerenes,' *Noyes Publications*, 1994.

[37] N. Sykam and G. M. Rao, 'Lightweight flexible graphite sheet for high-performance electromagnetic interference shielding,' *Materials Letters*, vol. 233, pp. 59–62, 2018.

[38] J. Gu, Y. Leng, Y. Gao, H. Liu, F. Kang and W. Shen, 'Fracture mechanism of flexible graphite sheets,' *Carbon*, vol. 40, no. 12, pp. 2169–2176, 2002. DOI: 10.1016/S0008-6223(02)00075-1.

[39] X. H. Wei, L. Liu, J. X. Zhang, J. L. Shi and Q. G. Guo, 'Mechanical, electrical, thermal performances and structure characteristics of flexible graphite sheets,' *Journal of Materials Science*, vol. 45, no. 9, pp. 2449–2455, 2010. DOI: 10.1007/s10853-010-4216-y.

[40] R. Reynolds and R. Greinke, 'Influence of expansion volume of intercalated graphite on tensile properties of flexible graphite,' *Carbon (New York, NY)*, vol. 39, no. 3, pp. 479–481, 2001.

[41] S. G. Ionov, V. V. Avdeev, S. V. Kuvshinnikov and E. P. Pavlova, 'Physical and chemical properties of flexible graphite foils,' *Molecular Crystals and Liquid Crystals Science and Technology. Section A. Molecular Crystals and Liquid Crystals*, vol. 340, no. 1, pp. 349–354, 2000.

[42] D. Savchenko, S. Ionov and A. Sizov, 'Properties of carbon-carbon composites based on exfoliated graphite,' *Inorganic Materials*, vol. 46, no. 2, pp. 132–138, 2010.

[43] Y.-L. Mo, Y.-X. Tian, Y.-H. Liu, F. Chen and Q. Fu, 'Preparation and properties of ultrathin flexible expanded graphite film via adding natural rubber,' *Chinese Journal of Polymer Science*, vol. 37, no. 8, pp. 806–814, 2019.

[44] G. M. Jenkins, 'Analysis of the stress-strain relationships in reactor grade graphite,' *British Journal of Applied Physics*, vol. 13, no. 1, pp. 30–32, 1962. DOI: 10.1088/0508-3443/13/1/307.

[45] X. Xi and D. Chung, 'Electret, piezoelectret and piezoresistivity discovered in steels, with application to structural self-sensing and structural self-powering,' *Smart Materials and Structures*, vol. 28, no. 7, p. 075 028, 2019.

[46] M. Cermak and M. Bahrami, 'Compression behavior of natural graphite sheet,' *SN Applied Sciences*, vol. 2, no. 3, pp. 1–7, 2020.

[47] P. Jaszak, 'Adaptation of a highly compressible elastomeric material model to simulate compressed expanded graphite and its application in the optimization of a graphite-metallic structure,' *Journal of the Brazilian Society of Mechanical Sciences and Engineering*, vol. 42, no. 5, pp. 1–22, 2020.

[48] M. Smalc, J. Norley, R. A. Reynolds III, R. Pachuta and D. W. Krassowski, 'Advanced thermal interface materials using natural graphite,' in *International Electronic Packaging Technical Conference and Exhibition*, vol. 36908, 2003, pp. 253–261.

[49] P.-H. Chen and D. Chung, 'Elastomeric behavior of exfoliated graphite, as shown by instrumented indentation testing,' *Carbon*, vol. 81, pp. 505–513, 2015.

[50] M. Khelifa, V. Fierro, J. Macutkevic and A. Celzard, 'Nanoindentation of flexible graphite: Experimental versus simulation studies,' *Review in Advanced Material Science*, vol. 3, no. 2, 2018.

[51] O. Blakslee, D. Proctor, E. Seldin, G. Spence and T. Weng, 'Elastic constants of compression-annealed pyrolytic graphite,' *Journal of applied physics*, vol. 41, no. 8, pp. 3373–3382, 1970.

[52] E. Seldin, 'Stress-strain properties of polycrystalline graphites in tension and compression at room temperature,' *Carbon*, vol. 4, no. 2, pp. 177–191, 1966.

[53] X. Luo and D. Chung, 'Vibration damping using flexible graphite,' *Carbon*, vol. 38, pp. 1499–1524, 2000.

[54] P.-H. Chen and D. Chung, 'Dynamic mechanical behavior of flexible graphite made from exfoliated graphite,' *Carbon*, vol. 50, no. 1, pp. 283–289, 2012.

[55] D. Chung, 'Interface-derived extraordinary viscous behavior of exfoliated graphite,' *Carbon*, vol. 68, pp. 646–652, 2014.

[56] L. Xiao and D. Chung, 'Mechanical energy dissipation modeling of exfoliated graphite based on interfacial friction theory,' *Carbon*, vol. 108, pp. 291–302, 2016.

[57] M. Cermak, N. Perez, M. Collins and M. Bahrami, 'Material properties and structure of natural graphite sheet,' *Scientific reports*, vol. 10, no. 1, pp. 1–12, 2020.

[58] X. Py, R. Olives and S. Mauran, 'Paraffin/porous-graphite-matrix composite as a high and constant power thermal storage material,' *International Journal of heat and mass transfer*, vol. 44, no. 14, pp. 2727–2737, 2001.

[59] R. Liu, J. Chen, M. Tan, S. Song, Y. Chen and D. Fu, 'Anisotropic high thermal conductivity of flexible graphite sheets used for advanced thermal management materials,' IEEE, vol. 1, 2013, pp. 107–111.

[60] M. Bonnissel, L. Luo and D. Tondeur, 'Compacted exfoliated natural graphite as heat conduction medium,' *Carbon*, vol. 39, no. 14, pp. 2151–2161, 2001. DOI: 10.1016/S0008-6223(01)00032-X.

[61] R. Olives and S. Mauran, 'A highly conductive porous medium for solid–gas reactions: Effect of the dispersed phase on the thermal tortuosity,' *Transport in porous media*, vol. 43, no. 2, pp. 377–394, 2001.

[62] P.-H. Chen and D. Chung, 'Thermal and electrical conduction in the compaction direction of exfoliated graphite and their relation to the structure,' *Carbon*, vol. 77, pp. 538–550, 2014.

[63] C. Y. Ho, R. W. Powell and P. E. Liley, 'Thermal conductivity of the elements,' *Journal of Physical and Chemical Reference Data*, vol. 1, no. 2, pp. 279–421, 1972.

[64] S. Chen, Q. Wu, C. Mishra, J. Kang, H. Zhang, K. Cho, W. Cai, A. A. Balandin and R. S. Ruoff, 'Thermal conductivity of isotopically modified graphene,' *Nature materials*, vol. 11, no. 3, pp. 203–207, 2012.

[65] S. Picard, D. Burns and P. Roger, 'Measurement of the specific heat capacity of graphite,' 2006.

[66] A. Butland and R. Maddison, 'The specific heat of graphite: An evaluation of measurements,' *Journal of Nuclear Materials*, vol. 49, no. 1, pp. 45–56, 1973.

[67] A. Lutcov, V. Volga and B. Dymov, 'Thermal conductivity, electric resistivity and specific heat of dense graphites,' *Carbon*, vol. 8, no. 6, pp. 753–760, 1970.

[68] C. Brooks and R. Bingham, 'The specific heat of aluminum from 330 to 890 k and contributions from the formation of vacancies and anharmonic effects,' *Journal of Physics and Chemistry of Solids*, vol. 29, no. 9, pp. 1553–1560, 1968.

[69] J. R. Davis *et al.*, *Copper and copper alloys*. ASM international, 2001.

[70] D. Riley, 'The thermal expansion of graphite: Part ii. theoretical,' *Proceedings of the Physical Society*, vol. 57, no. 6, p. 486, 1945.

[71] W. Morgan, 'Thermal expansion coefficients of graphite crystals,' *Carbon*, vol. 10, no. 1, pp. 73–79, 1972.

[72] D. Tsang, B. Marsden, S. Fok and G. Hall, 'Graphite thermal expansion relationship for different temperature ranges,' *Carbon*, vol. 43, no. 14, pp. 2902–2906, 2005.

[73] J. E. Zorzi and C. A. Perottoni, 'Thermal expansion of graphite revisited,' *Computational Materials Science*, vol. 199, p. 110 719, 2021.

[74] A. Bailey and B. Yates, 'Anisotropic thermal expansion of pyrolytic graphite at low temperatures,' *Journal of Applied Physics*, vol. 41, no. 13, pp. 5088–5091, 1970.

[75] F. Entwisle, 'Thermal expansion of pyrolytic graphite,' *Phys. Letters*, vol. 2, 1962.

[76] E. Kellett and B. Richards, 'The thermal expansion of graphite within the layer planes,' *Journal of Nuclear Materials*, vol. 12, no. 2, pp. 184–192, 1964.

[77] J. H. W. Simmons, *Radiation damage in graphite: international series of monographs in nuclear energy*. Elsevier, 2013, vol. 102.

[78] B. T. Kelly, 'Physics of graphite,' 1981.

[79] I. Mason and R. Knibbs, 'The thermal conductivity of artificial graphites and its relationship to electrical resistivity,' Tech. Rep., 1962.

[80] R. Powell, 'The thermal and electrical conductivities of a sample of acheson graphite from 0°C to 800°C,' *Proceedings of the Physical Society*, vol. 49, no. 4, p. 419, 1937.

[81] Y. M. Hoi and D. Chung, 'Flexible graphite as a compliant thermoelectric material,' *Carbon*, vol. 40, no. 7, pp. 1134–1136, 2002.

[82] J. Gandhi and A. Pathak, 'Performance evaluation of thermal interface material for space applications,' in *Applied Mechanics and Materials*, Trans Tech Publ, vol. 110, 2012, pp. 135–141.

[83] E. E. Marotta, S. J. Mazzuca and J. Norley, 'Thermal joint conductance for flexible graphite materials: Analytical and experimental study,' *IEEE Transactions on Components and Packaging Technologies*, vol. 28, no. 1, pp. 102–110, 2005.

[84] N. Nan, J. Wang and A. A. Eckstein, 'FIB-SEM Three-Dimensional Tomography for Characterization of Carbon-Based Materials,' *Advances in Materials Science and Engineering*, vol. 2019, 2019. DOI: 10.1155/2019/8680715.

[85] T. Prill, K. Schladitz and C. Wieser, 'Simulation of FIB-SEM images for segmentation of porous microstructures,' *1st International Conference on 3D Materials Science 2012, 3DMS 2012*, vol. 35, pp. 159–164, 2012. DOI: 10.1007/978-3-319-48762-5_24.

[86] E. P. Randviir, D. A. Brownson and C. E. Banks, 'A decade of graphene research: Production, applications and outlook,' *Materials Today*, vol. 17, no. 9, pp. 426–432, 2014.

[87] 'ASTM D695-15 Standard Test Method for Compressive Properties of Rigid Plastics,' pp. 1–8, 2015. DOI: 10.1520/D0695-15.2.

[88] ISO 13003:2003, 'Fibre-reinforced plastics - Determination of fatigue properties under cyclic loading conditions,' *International Standard Organization*, vol. 3, 2013.

[89] M. W. Barsoum, A. Murugaiah, S. R. Kalidindi, T. Zhen and Y. Gogotsi, 'Kink bands, nonlinear elasticity and nanoindentations in graphite,' *Carbon*, vol. 42, no. 8-9, pp. 1435–1445, 2004. DOI: 10.1016/j.carbon.2003.12.090.

[90] R. A. Guyer and P. A. Johnson, 'Nonlinear mesoscopic elasticity: Evidence for a new class of materials,' *Physics Today*, vol. 52, no. 4, pp. 30–36, 1999. DOI: 10.1063/1.882648.

[91] Y. Sun, B. Amirrasouli, S. B. Razavi, Q. Li, T. Lowe and P. Withers, 'The variation in elastic modulus throughout the compression of foam materials,' *Acta Materialia*, vol. 110, pp. 161–174, 2016.

[92] J. P. Masse, L. Salvo, D. Rodney, Y. Bréchet and O. Bouaziz, 'Influence of relative density on the architecture and mechanical behaviour of a steel metallic wool,' *Scripta Materialia*, vol. 54, no. 7, pp. 1379–1383, 2006. DOI: 10.1016/j.scriptamat.2005.11.075.

[93] I. M. Afanasov, D. V. Savchenko, S. G. Ionov, D. A. Rusakov, A. N. Seleznev and V. V. Avdeev, 'Thermal conductivity and mechanical properties of expanded graphite,' *Inorganic Materials*, vol. 45, no. 5, pp. 486–490, 2009. DOI: 10.1134/S0020168509050057.

[94] Neograf Solutions, *GRAFOIL - Flexible graphite*, 2002.

[95] I. Gibson and M. F. Ashby, 'The mechanics of three-dimensional cellular materials,' *Proceedings of the royal society of London. A. Mathematical and physical sciences*, vol. 382, no. 1782, pp. 43–59, 1982.

[96] A. C. Fischer-Cripps and D. Nicholson, 'Nanoindentation. mechanical engineering series,' *Appl. Mech. Rev.*, vol. 57, no. 2, B12–B12, 2004.

[97] D. Wang, X. Lu, Y. Deng, X. Guo and A. Barnoush, 'Effect of hydrogen on nanomechanical properties in Fe-22Mn-0.6 C TWIP steel revealed by in-situ electrochemical nanoindentation,' *Acta Materialia*, vol. 166, pp. 618–629, 2019.

[98] W. C. Oliver and G. M. Pharr, 'An improved technique for determining hardness and elastic modulus using load and displacement sensing indentation experiments,' *Journal of materials research*, vol. 7, no. 6, pp. 1564–1583, 1992.

[99] I. N. Sneddon, 'Boussinesq's problem for a rigid cone,' in *Mathematical Proceedings of the Cambridge Philosophical Society*, Cambridge University Press, vol. 44, 1948, pp. 492–507.

[100] A. Delafargue and F.-J. Ulm, 'Explicit approximations of the indentation modulus of elastically orthotropic solids for conical indenters,' *International journal of solids and structures*, vol. 41, no. 26, pp. 7351–7360, 2004.

[101] D. Tabor, 'A simple theory of static and dynamic hardness,' *Proceedings of the Royal Society of London. Series A. Mathematical and Physical Sciences*, vol. 192, no. 1029, pp. 247–274, 1948.

[102] I. Efthymiopoulos, D. Grenier, M. Meddahi, P. Trilhe, S. Evrard, H. Vincke, C. Theis, N. Charitonidis, C. Hessler, A. Pardons *et al.*, 'HiRadMat: A new irradiation facility for material testing at CERN,' Tech. Rep., 2011.

[103] *ASTM E228 - Standard Test Method for Linear Thermal Expansion of Solid Materials with a Push-rod Dilatometer*. ASTM International, 2017.

[104] R. B. Berke and J. Lambros, 'Ultraviolet digital image correlation (uv-dic) for high temperature applications,' *Review of Scientific Instruments*, vol. 85, no. 4, p. 045 121, 2014.

[105] W. H. Smith and D. H. Leeds, 'Pyrolytic graphite,' *Modern materials*, vol. 7, pp. 139–221, 1970.

[106] F. Balima, S. Le Floch, A. San-Miguel, P. Lindner, A. Brûlet, L. Duclaux and V. Pischedda, 'Shear effects on expanded graphite under uniaxial pressure: An in situ small angle neutron scattering study,' *Carbon*, vol. 74, pp. 54–62, 2014. DOI: 10.1016/j.carbon.2014.03.002.

[107] F. Martoïa, L. Orgéas, P. J. Dumont, J. F. Bloch, F. Flin and J. Viguié, 'Crumpled paper sheets: Low-cost biobased cellular materials for structural applications,' *Materials and Design*, vol. 136, pp. 150–164, 2017. DOI: 10.1016/j.matdes.2017.09.031.

[108] J. A. Baimova, E. A. Korznikova, S. V. Dmitriev, B. Liu and K. Zhou, 'Review on crumpled graphene: Unique mechanical properties,' *Reviews on Advanced Materials Science*, vol. 39, no. 1, pp. 69–83, 2014.

[109] C. Hui, Y. Zhang, L. Zhang, R. Sun and F. Liu, 'Crumpling of a pyrolytic graphite sheet,' *Journal of Applied Physics*, vol. 114, no. 16, pp. 14–18, 2013. DOI: 10.1063/1.4827842.

[110] Y. Liao, Z. Li, W. Xia *et al.*, 'Size-dependent structural behaviors of crumpled graphene sheets,' *Carbon*, vol. 174, pp. 148–157, 2021.

[111] A. S. Balankin, M. A. Cruz, L. A. Caracheo, O. S. Huerta, C. D. Rivas, C. L. Martínez, D. S. Ochoa, L. M. Ruiz, S. M. Gutiérrez, J. P. Ortiz and M. P. Ortiz, 'Mechanical properties and relaxation behavior of crumpled aluminum foils,' *Journal of Materials Science*, vol. 50, no. 13, pp. 4749–4761, 2015. DOI: 10.1007/s10853-015-9030-0.

[112] P. Liu, Q. Tan, L. Wu and G. He, 'Compressive and pseudo-elastic hysteresis behavior of entangled titanium wire materials,' *Materials Science and Engineering A*, vol. 527, no. 15, pp. 3301–3309, 2010. DOI: 10.1016/j.msea.2010.02.071.

[113] Q. Tan, P. Liu, C. Du, L. Wu and G. He, 'Mechanical behaviors of quasi-ordered entangled aluminum alloy wire material,' *Materials Science and Engineering: A*, vol. 527, no. 1-2, pp. 38–44, 2009.

[114] O. Bouaziz, J. P. Masse, S. Allain, L. Orgéas and P. Latil, 'Compression of crumpled aluminum thin foils and comparison with other cellular materials,' *Materials Science and Engineering A*, vol. 570, pp. 1–7, 2013. DOI: 10.1016/j.msea.2013.01.031.

[115] J. Luo, H. D. Jang, T. Sun, L. Xiao, Z. He, A. P. Katsoulidis, M. G. Kanatzidis, J. M. Gibson and J. Huang, 'Compression and aggregation-resistant particles of crumpled soft sheets,' *ACS nano*, vol. 5, no. 11, pp. 8943–8949, 2011.

[116] A. D. Cambou and N. Menon, 'Three-dimensional structure of a sheet crumpled into a ball,' *Proceedings of the National Academy of Sciences of the United States of America*, vol. 108, no. 36, pp. 14 741–14 745, 2011. DOI: 10.1073/pnas.1019192108.

[117] T. Tallinen, J. Åström and J. Timonen, 'The effect of plasticity in crumpling of thin sheets,' *Nature materials*, vol. 8, no. 1, pp. 25–29, 2009.

[118] S. W. Cranford and M. J. Buehler, 'Packing efficiency and accessible surface area of crumpled graphene,' *Physical Review B*, vol. 84, no. 20, p. 205 451, 2011.

[119] A. S. Balankin, A. Horta Rangel, G. García Pérez, F. Gayosso Martinez, H. Sanchez Chavez and C. L. Martínez-González, 'Fractal features of a crumpling network in randomly folded thin matter and mechanics of sheet crushing,' *Physical Review E - Statistical, Nonlinear, and Soft Matter Physics*, vol. 87, no. 5, pp. 1–11, 2013. DOI: 10.1103/PhysRevE.87.052806.

[120] S. Cottrino, P. Viviès, D. Fabrègue and E. Maire, 'Mechanical properties of crumpled aluminum foils,' *Acta Materialia*, vol. 81, pp. 98–110, 2014. DOI: 10.1016/j.actamat.2014.07.069.

[121] D. Hughes, E. H. Amalu, T. Pak and R. Kennedy, 'Effect of relative density on compressive load response of crumpled aluminium foil mesh,' *Materials*, vol. 12, no. 23, 2019. DOI: 10.3390/ma12234018.

[122] S. Toll, 'Packing mechanics of fiber reinforcements,' *Polymer Engineering & Science*, vol. 38, no. 8, pp. 1337–1350, 1998.

[123] *Abaqus Analysis User's Manual*, Version 6. Simulia Dassault Systèmes, 2022.

[124] R. M. Jones and D. A. Nelson Jr, 'Material models for nonlinear deformation of graphite,' *AIAA Journal*, vol. 14, no. 6, pp. 709–717, 1976.

[125] S. Duffy, 'Modeling stress strain relationships and predicting failure probabilities for graphite core components,' Cleveland State Univ., Cleveland, OH (United States), Tech. Rep., 2013.

[126] J. Summerscales, 'The bulk modulus of carbon fibers,' *Journal of Materials science letters*, vol. 19, no. 1, pp. 15–16, 2000.

[127] S. Zhang, Y. Li, M. Luo and C. Shan, 'Modelling of nonlinear and dual-modulus characteristics and macro-orthogonal cutting simulation of unidirectional carbon/carbon composites,' *Composite Structures*, vol. 280, 2022.

[128] Y. Dafalias and E. Popov, 'A model of nonlinearly hardening materials for complex loading,' *Acta mechanica*, vol. 21, no. 3, pp. 173–192, 1975.

[129] W. Greenstreet and A. Phillips, 'A theory of an elastic-plastic continuum with special emphasis to artificial graphite,' *Acta Mechanica*, vol. 16, no. 1-2, pp. 143–156, 1973.

[130] B. Poon, D. Rittel and G. Ravichandran, 'An analysis of nanoindentation in linearly elastic solids,' *International Journal of Solids and Structures*, vol. 45, no. 24, pp. 6018–6033, 2008.

[131] B. Poon, D. Rittel and G. Ravichandran, 'An analysis of nanoindentation in elasto-plastic solids,' *International Journal of Solids and Structures*, vol. 45, no. 25-26, pp. 6399–6415, 2008.

[132] J. C. Hay, A. Bolshakov and G. Pharr, 'A critical examination of the fundamental relations used in the analysis of nanoindentation data,' *Journal of materials Research*, vol. 14, no. 6, pp. 2296–2305, 1999.

[133] A. Hirth, P. Du Bois and K. Weimar, 'A material model for transversely anisotropic crushable foams in ls-dyna,' in *7th International LS-DYNA Users Conference*, 2002, pp. 16–23.

[134] Y. Zhang, C. Kong, R. S. Davidsen, G. Scardera, L. Duan, K. T. Khoo, D. N. Payne, B. Hoex and M. Abbott, '3D characterisation using plasma FIB-SEM: A large-area tomography technique for complex surfaces like black silicon,' *Ultramicroscopy*, vol. 218, 2020.

[135] T. Tallinen, J. A. Åström and J. Timonen, 'Discrete element simulations of crumpling of thin sheets,' *Computer Physics Communications*, vol. 180, no. 4, pp. 512–516, 2009.

[136] T. Bru, R. Olsson, R. Gutkin and G. M. Vyas, 'Use of the iosipescu test for the identification of shear damage evolution laws of an orthotropic composite,' *Composite structures*, vol. 174, pp. 319–328, 2017.

[137] ASTM Internationa, 'ASTM D5379 - Standard Test Method for Shear Properties of Composite Materials by the V-Notched Beam Method,' 2019.

[138] J. F. Davalos, P. Qiao, J. Wang, H. A. Salim and J. Schlussel, 'Shear moduli of structural composites from torsion tests,' *Journal of composite materials*, vol. 36, no. 10, pp. 1151–1173, 2002.

[139] H. T. Sumsion and Y. D. Rajapakse, 'Simple torsion test for shear moduli determination of orthotropic composites,' in *Intern. Conf. on Composite Mater.*, 1978.

[140] C. Tsai and I. Daniel, 'Determination of in-plane and out-of-plane shear moduli of composite materials,' *Experimental mechanics*, vol. 30, pp. 295–299, 1990.

[141] ASTM C747-93, 'Standard Test Method for Moduli of Elasticity and Fundamental Frequencies of Carbon and Graphite Materials by Sonic Resonance,' *ASTM Book of Standards*, vol. 93, no. Reapproved 2010, pp. 1–8, 2010. DOI: 10.1520/C0747-16.1.4.

[142] A. Reyes, O. S. Hopperstad, T. Berstad, A. G. Hanssen and M. Langseth, 'Constitutive modeling of aluminum foam including fracture and statistical variation of density,' *European Journal of Mechanics-A/Solids*, vol. 22, no. 6, pp. 815–835, 2003.

ISBN 978-82-326-7138-0 (printed ver.)
ISBN 978-82-326-7137-3 (electronic ver.)
ISSN 1503-8181 (printed ver.)
ISSN 2703-8084 (online ver.)

NTNU

Norwegian University of
Science and Technology